

Electronic Theses and Dissertations, 2004-2019

2014

Advanced Liquid Crystal Materials For Display And Photonic Applications

Yuan Chen
University of Central Florida

 Part of the [Electromagnetics and Photonics Commons](#), and the [Optics Commons](#)
Find similar works at: <https://stars.library.ucf.edu/etd>
University of Central Florida Libraries <http://library.ucf.edu>

This Doctoral Dissertation (Open Access) is brought to you for free and open access by STARS. It has been accepted for inclusion in Electronic Theses and Dissertations, 2004-2019 by an authorized administrator of STARS. For more information, please contact STARS@ucf.edu.

STARS Citation

Chen, Yuan, "Advanced Liquid Crystal Materials For Display And Photonic Applications" (2014). *Electronic Theses and Dissertations, 2004-2019*. 4561.
<https://stars.library.ucf.edu/etd/4561>

ADVANCED LIQUID CRYSTAL MATERIALS FOR DISPLAY AND PHOTONIC APPLICATIONS

by

YUAN CHEN

B.S., Optical Engineering, Zhejiang University, China, 2007

M.S., Optics, University of Central Florida, 2012

A dissertation submitted for partial fulfillment of the requirements
for the degree of Doctor of Philosophy
in the College of Optics and Photonics
at the University of Central Florida
Orlando, Florida

Summer Term
2014

Major Professor: Shin-Tson Wu

© 2014 Yuan Chen

ABSTRACT

Thin-film-transistor (TFT) liquid crystal display (LCD) has been widely used in smartphones, pads, laptops, computer monitors, and large screen televisions, just to name a few. A great deal of effort has been delved into wide viewing angle, high resolution, low power consumption, and vivid color. However, relatively slow response time and low transmittance remain as technical challenges. To improve response time, several approaches have been developed, such as low viscosity liquid crystals, overdrive and undershoot voltage schemes, thin cell gap with a high birefringence liquid crystal, and elevated temperature operation. The state-of-the-art gray-to-gray response time of a nematic LC device is about 5 ms, which is still not fast enough to suppress the motion picture image blur. On the other hand, the LCD panel's transmittance is determined by the backlight, polarizers, TFT aperture ratio, LC transmittance, and color filters. Recently, a fringe-field-switching mode using a negative dielectric anisotropy ($\Delta\epsilon$) LC (n-FFS) has been demonstrated, showing high transmittance (98%), single gamma curve, and cell gap insensitivity. It has potential to replace the commonly used p-FFS (FFS using positive $\Delta\epsilon$ LC) for mobile displays.

With the urgent need of submillisecond response time for enabling color sequential displays, polymer-stabilized blue phase liquid crystal (PS-BPLC) has become an increasingly important technology trend for information display and photonic applications. BPLCs exhibit several attractive features, such as reasonably wide temperature range, submillisecond gray-to-gray response time, no need for alignment layer, optically isotropic voltage-off state, and large cell gap tolerance. However, some bottlenecks such as high operation voltage, hysteresis, residual

birefringence, and slow charging issue due to the large capacitance, remain to be overcome before their widespread applications can be realized. The material system of PS-BPLC, including nematic LC host, chiral dopant, and polymer network, are discussed in detail. Each component plays an essential role affecting the electro-optic properties and the stability of PS-BPLC.

In a PS-BPLC system, in order to lower the operation voltage the host LC usually has a very large dielectric anisotropy ($\Delta\epsilon > 100$), which is one order of magnitude larger than that of a nematic LC. Such a large $\Delta\epsilon$ not only leads to high viscosity but also results in a large capacitance. High viscosity slows down the device fabrication process and increases device response time. On the other hand, large capacitance causes slow charging time to each pixel and limits the frame rate. To reduce viscosity, we discovered that by adding a small amount (~6%) of diluters, the response time of the PS-BPLC is reduced by 2X-3X while keeping the Kerr constant more or less unchanged. Besides, several advanced PS-BPLC materials and devices have been demonstrated. By using a large $\Delta\epsilon$ BPLC, we have successfully reduced the voltage to <10V while maintaining submillisecond response time. Finally we demonstrated an electric field-induced monodomain PS-BPLC, which enables video-rate reflective display with vivid colors. The highly selective reflection in polarization makes it promising for photonics application.

Besides displays in the visible spectral region, LC materials are also very useful electro-optic media for near infrared and mid-wavelength infrared (MWIR) devices. However, large absorption has impeded the widespread application in the MWIR region. With delicate molecular design strategy, we balanced the absorption and liquid crystal phase stability, and proposed a fluoro-terphenyl compound with low absorption in both MWIR and near IR regions. This

compound serves as an important first example for future development of low-loss MWIR liquid crystals, which would further expand the application of LCs for amplitude and/or phase modulation in MWIR region.

ACKNOWLEDGMENTS

I would like to first thank my Ph. D. advisor and mentor: Dr. Shin-Tson Wu. His insightful lecture “Liquid crystal materials and devices” inspired me and led me into the liquid crystal research in his group. Dr. Wu has been extremely helpful and supportive during my Ph. D study and research. Whenever I had obstacles in research or life and needed help, he has always been willing to discuss with me and encourage me. He has also provided me precious opportunities to interact with eminent scholars in at international conferences and broaden my horizon, which tremendously benefits my research and professional career. He also enthusiastically uplifted me by nominating me to win several prestigious society awards, which greatly enhance my self-esteem. Without him, it wouldn’t be possible for me to advance my graduate studies and professional career so smoothly.

I also appreciate all the contribution of time, ideas, insightful discussion and support from Dr. Martin Schadt. It’s great honor to know him. His wisdom and enthusiasm motivated me to be more productive in my research.

I’m very grateful to be in our research group, which is more like a big warm family. I appreciate everyone’s guidance, discussion and friendship. Especially I would like to thank Dr. Jie Sun and Dr. Jin Yan. Jie taught me how to prepare and characterize nematic liquid crystals and polymer network liquid crystals when I just joined this group. Jin walked me through the fabrication of PS-BPLC and shared her abundant knowledge with me. Besides, their dedication to research and hardworking spirit also set a good example for me. I would like to say thank you to our collaborators who helped us with liquid crystal material synthesis, test cells and financial

support. I also want to acknowledge my committee members, Dr. Winston Schoenfeld, Dr. Boris Zeldovich and Dr. Jiyu Fang for their delightful conversations and guidance.

Lastly I would like to thank my family for all their unconditional love and encouragement. My parents have raised me up and educated me well and supported me in all my pursuits. And most of all I want to thank my loving, supportive and encouraging husband Ming Wei, who is willing to sacrifice his time and effort to faithfully support me. Thank you!

TABLE OF CONTENTS

LIST OF FIGURES	x
LIST OF TABLES.....	xiv
CHAPTER ONE: INTRODUCTION.....	1
CHAPTER TWO: HIGH PERFORMANCE NEMATIC LIQUID CRYSTALS	5
2.1 High Birefringence Positive Dielectric Anisotropy Nematic Liquid Crystals.....	5
2.1.1 Response Time	5
2.1.2 Thin Cell Approach.....	6
2.1.3 Temperature Effect.....	11
2.1.4 Driving Scheme.....	14
2.2 Advanced Negative Dielectric Anisotropy Nematic Liquid Crystals	15
2.2.1 Overview and Recent Progress	15
2.2.2 Negative $\Delta\epsilon$ LCs for FFS Mode.....	17
2.2.3 Negative $\Delta\epsilon$ LCs for VA Mode.....	32
CHAPTER THREE: POLYMER-STABILIZED BLUE PHASE LIQUID CRYSTALS	41
3.1 Background and Current Progress.....	41
3.2 PS-BPLC Material System.....	43
3.2.1 Nematic Liquid Crystal Host.....	44

3.2.2	Chiral Dopants.....	47
3.2.3	Polymer Network	49
3.3	Properties of PS-BPLC.....	51
3.3.1	Blue Phase Appearance.....	51
3.3.2	Electric Field Effect	52
3.3.3	Diluter Effects on PS-BPLC	54
3.4	Advanced PS-BPLC Materials and Devices	65
3.4.1	A Microsecond Response Time PS-BPLC.....	65
3.4.2	Large Kerr Constant and Low Voltage Blue Phase Liquid Crystal	73
3.4.3	Electric Field-Induced Monodomain Blue Phase.....	82
CHAPTER FOUR: LOW ABSORPTION LIQUID CRYSTALS FOR MID-WAVE INFRARED APPLICATIONS		94
4.1	Molecular Design Strategy.....	96
4.2	Absorption and Physical Properties	98
CHAPTER FIVE: SUMMARY.....		103
CHAPTER SIX: MAJOR ACCOMPLISHMENTS.....		105
APPENDIX: LIST OF PUBLICATIONS		107
LIST OF REFERENCES		114

LIST OF FIGURES

Figure 1. Refractive indices of M4 at different wavelengths: dots are measured data and lines are fittings with Equation (6).....	9
Figure 2. Birefringence of M4: dots stand for measured data and solid line for fitting curve. $\lambda=633$ nm.....	10
Figure 3. Temperature dependent visco-elastic constant of M4: dots are experimental data and solid line is fitting.	12
Figure 4. FoM of M4 vs. T . $\lambda=633$ nm. Dots are experimental data and solid line is fitting by Equation (13).	13
Figure 5. Temperature dependent Δn of UCF-N1, HAV, ZOC and UCF-N2 at $\lambda=633$ nm.....	19
Figure 6. Birefringence dispersion of the four LC mixtures studied.	20
Figure 7. Temperature dependent (a) γ_1/k_{33} and (b) FoM of the four LCs studied.	21
Figure 8. Device configuration of FFS structure, equal-potential lines, and LC director deformation in voltage-on state of (a) n-FFS and (b) p-FFS.	23
Figure 9. T_p and V_{on} at different $d\Delta n/\lambda$ for n-FFS and p-FFS.	24
Figure 10. VT curves for FFS cell using (a) UCF-N0 (b) UCF-N1 (c) UCF-HB and (d) UCF-P1 for RGB colors. Inset plots show the normalized VT curves.	26
Figure 11. Simulated twist angle distribution of (a) FFS-N1 and (c) FFS-P1; Tilt angle distribution of (b) FFS-N1 and (d) FFS-P1.....	27

Figure 12. $\Delta\varepsilon$ effect on the Von of n-FFS under two types of passivation layers.	30
Figure 13. Simulated isocontrast plots for: (a) FFS-P1 and (b) FFS-N1.	31
Figure 14. (a) Temperature dependent Δn of UCF-N3 at $\lambda=633\text{nm}$. (b) Wavelength dependent Δn of UCF-N3 at $T=50^\circ\text{C}$	35
Figure 15. Temperature dependent (a) γ_1/k_{33} and (b) FoM of UCF-N3.....	35
Figure 16. Simulated VR curves for RGB of a VA LCOS using UCF-N3 at 50°C . $d=0.93\ \mu\text{m}$. 36	
Figure 17. VT curves for VA cell with UCF-N2 ($d=3.07\ \mu\text{m}$) and MLC 6882 ($d=3.37\ \mu\text{m}$), respectively.	40
Figure 18. Chemical structures of some exemplary nematic LC hosts, chiral dopants, and monomers used in polymer-stabilized BPLC systems. ²¹	44
Figure 19. Illustration of the mechanism for polymer stabilization effect on blue phase	50
Figure 20. (a),(c),(e) Typical multi-domain blue phase platelet texture (b),(d),(e) monodomain blue phase texture with different pitch length. Reflective images.....	52
Figure 21. Temperature dependent (a) Δn at $\lambda=633\ \text{nm}$, (b) $\Delta\varepsilon$ at $1\ \text{kHz}$, (c) γ_1/k_{11} and (d) γ_1 of LC1 and LC2. Dots represent the measured data and lines are fitting results by Equation (8), (10), (12) and (23), respectively.	56
Figure 22. Illustration of relaxation frequency shifting by doping a low viscosity diluter to a LC host.....	58
Figure 23. Measured VT cures for PSBP-1, 2, 8 and 10. $\lambda=633\ \text{nm}$	60
Figure 24. Temperature dependent decay time of PSBP-1 and PSBP-2. Dots are measured data and lines are fitting with Equation (25).	64

Figure 25. (a) Microscopic image of the PS-BPLC under crossed polarizers, and (b) Experimental setup for electro-optic measurement of the VFS cell.	68
Figure 26. VT curve for cell with TMPTA (blue line) and for cell with C12A (red line).....	69
Figure 27. Hysteresis loop for Sample A and Sample B.	70
Figure 28. Blue line: Temperature dependent Δn of the LC host; Red line: Temperature dependent decay time for the VFS PSBP cell (Sample B). Dots: experimental data.	72
Figure 29. POM images of the homogeneous cells filled with (a) JC-BP06N and (b) LC1 (with alignment direction parallel to the optic axis of the polarizer).	74
Figure 30. Frequency-dependent $\varepsilon_{//}$ ' and ε_{\perp} ' of JC-BP06N and LC1.....	75
Figure 31. VT curves of the VFS cell at the specified wavelengths. Dots are measured data and lines are fitted curves with extended Kerr model. Cell gap $d=3.2 \mu\text{m}$	78
Figure 32. Cell gap effect on V_{on} and optimized cell gap for hysteresis-free and $V_{on}<10\text{V}$	80
Figure 33. The VT curves (data and fitting) at the specified wavelengths of an IPS-5/5 cell.....	81
Figure 34. Measured reflection spectra of the green PSBP cell.	85
Figure 35 Reflection spectra at different voltages for (a) red, (b) green, and (c) blue cells. The inset photos are the corresponding images at 0V (ITO area in the center: 12mm X 12mm).	87
Figure 36 Angular intensity distribution of the reflected beam from the red and green PBLC cell (Incident light: He-Ne laser beam for red cell and Argon laser beam for the green cell). Inset plots show the beam patterns.	89
Figure 37. Outdoor viewing angle performance of the R, G, and B cells.	90

Figure 38. Measured VR curves for LP and RCP incident lights, and reflectance for LCP at 0V.	91
Figure 39. Polarization state of the reflected light for RCP (open circle) and LP (solid circle) incident beams.	92
Figure 40. Measured transmission spectra of 5CB (Red), 1CB (Blue), FB (Green) and F7CB (Violet).....	97
Figure 41. Measured transmission spectra of 5CB (red line) and FT (blue line) in MWIR region	99
Figure 42. Measured transmission spectra of 5CB (red line) and FT (blue line) in near IR region.	100
Figure 43. Molecular structure with potentially wider nematic range for forming eutectic mixtures (X=F or OCF ₃).	102

LIST OF TABLES

Table 1. Chemical structures and properties of the compounds studied. C stands for crystalline phase, S for smectic phase and I for isotropic phase.	7
Table 2. Physical properties of the liquid crystals studied (measured at $\lambda=633$ nm, $T\sim 22$ °C and $f=1$ kHz).	18
Table 3. Calculated GTG response time (unit: ms) of the UCF-N3 VA LCOS at 50°C. $d=0.93$ μm	37
Table 4. Fitting parameters for LC1 and LC2	57
Table 5. Physical properties of PSBP samples containing 6% of different diluters. Here, Kerr constant and decay time were measured at $\lambda=633$ nm, and 25°C. (*The FOM_{BP} is normalized to that of PSBP-1).	60
Table 6. Influence of diluter concentration on the PS-BPLC properties.	65
Table 7. Comparison between Sample A and Sample B.	71
Table 8. Chemical structures and properties of the compounds studied. Cr stands for crystalline, N for nematic, and I for isotropic phase.	95

CHAPTER ONE: INTRODUCTION

Liquid crystals (LCs) have been widely used in display and photonic devices. Enormous efforts have been delved into high resolution, wide viewing angle, low power consumption, and vivid color. Improved fabrication capability enables high resolution and compensation films are used to widen the viewing angle. Recently LED (light emitting diode) backlight and red/green quantum dots (QDs) with narrow emission bandwidth are employed to boost the color gamut.¹ However, relatively slow response time and low transmittance remain technical challenges.

In addition to displays, liquid crystals are also useful for photonic devices,² such as phase modulators, filters, adaptive lenses, beam steering devices, and tunable microresonators, etc. Fast response time is also a highly desired feature for these tunable photonic devices. For a nematic LC, its response time is proportional to the square of cell gap (d). Thus, thin cell gap helps reduce response time effectively. However, to maintain sufficient phase retardation with a thin cell gap, high birefringence LC material is required regardless its dielectric anisotropy ($\Delta\epsilon$) is positive or negative. Chapter Two is devoted to high birefringence LC materials. Different approaches for improving response time will also be discussed. On the other hand, the LCD panel transmittance is determined by the backlight, polarizers, TFT (thin film transistor) aperture ratio, LC transmittance, and color filters. Recently, a fringe-field-switching mode using a negative dielectric anisotropy ($\Delta\epsilon$) LC (n-FFS) has been demonstrated, showing high transmittance, single gamma curve, and cell gap insensitivity. It has potential to replace the commonly used p-FFS (FFS using positive $\Delta\epsilon$ LC) for mobile displays. Besides fringe-field switching (FFS) cell,³⁻⁵ and in-plane switching (IPS) cell,^{6,7} where the electric field is mainly in

the lateral direction, a negative $\Delta\epsilon$ LC can also be used in a VA cell^{8,9} or multi-domain VA (MVA) cell,^{10,11} where the field is basically in the longitudinal direction.

The state-of-the-art gray-to-gray response time of most LCDs is about 5 ms, which is still not fast enough for eliminating the motion picture image blur. On the other hand, conventional TFT LCDs use red (R), green (G) and blue (B) spatial color filters to display color pictures. In such an additive color production scheme, the R sub-pixels only transmit red color while blocking the remaining spectrum from the backlight. Thus, the color filters transmit less than 1/3 of the backlight (white). On the other hand, a color sequential display¹²⁻¹⁴ reproduces each color component in different time sequence using synchronously pulsed colored backlights, such as RGB LEDs, and pixelated LC amplitude modulators.¹⁵ By eliminating the spatial color filters would not only simplify the device fabrication process and reduce cost, but also triples the optical efficiency and device resolution density. This feature is particularly important for reducing the power consumption of a high resolution retina display. However, to avoid color breakup the LC response time (gray to gray) should be kept below 1 ms. As a promising candidate for next-generation high speed display and photonics devices, PS-BPLC¹⁶⁻²¹ exhibits three distinctive features: 1) self-assembly process so that no surfactant (e.g., rubbed polyimide layer) is needed to generate uniform molecular alignment, 2) nanoscale (~100 nm) double-twist cylinder diameter and short coherence length which leads to microsecond response time,^{22,23} and 3) three-dimensional lattice structure resulting in optically isotropic voltage-off state. Alignment-layer-free process greatly simplifies the device fabrication process. Fast response time not only produces crisp video but also enables color sequential displays without noticeable color breakup.

Moreover, short coherence length significantly improves the diffraction efficiency of BPLC gratings.²⁴ Finally, optically isotropic state makes adaptive BPLC lenses polarization independent.^{25,26} Therefore, BPLC holds promises for display^{19,20} and photonic applications.²⁷ However, some bottlenecks such as high operation voltage, strong frequency-dependent $\Delta\epsilon$, hysteresis, residual birefringence, image sticking, charging issue due to the large capacitance, and relatively low transmittance for the IPS mode, remain to be overcome before widespread application of BPLC can be realized. To reduce operation voltage, both new BPLC materials and new device structures have been investigated. In this dissertation, we demonstrated a large Kerr constant PS-BPLC with on-state-voltage (V_{on}) <10V, fast response time BPLC material development and monodomain blue phase for reflective display and photonics application. The PS-BPLC material system, including LC host, chiral dopant, and polymer network, and physical properties will also be discussed in detail in Chapter Three.

Besides applications in the visible spectral region, linearly conjugated liquid crystals exhibit a relatively high birefringence in the infrared (IR) region^{28,29} and thus have been used in the 8-12 μm range as dynamic scene projectors for infrared seekers³⁰, and at $\lambda=10.6 \mu\text{m}$ and $1.55 \mu\text{m}$ for laser beam steering³¹ and infrared light shutter,³² and photonic crystal fiber.³³ A major concern for IR applications using LCs is the inherent absorption loss due to the existence of molecular vibration bands. Even in the off-resonance region, the baseline absorption coefficient may reach as high as $\alpha\sim 10 \text{ cm}^{-1}$,³⁴ but if the LC layer is thin ($\sim 5 \mu\text{m}$), then the absorption loss may be negligible. However, to achieve a sufficient phase change a minimum cell gap is required. As the cell gap increases, the absorption loss increases exponentially. In the vicinity of resonance

wavelengths where α is about 10^4 cm^{-1} , the 5- μm LC layer is now essentially opaque. Low absorption liquid crystal is essential for MWIR. In Chapter Four, we will discuss the molecular design strategy to achieve low absorption while maintaining liquid crystal phase. A new LC compound with low absorption in MWIR will be described. Finally, a brief summary on the major accomplishments will be given in Chapter Five.

CHAPTER TWO: HIGH PERFORMANCE NEMATIC LIQUID CRYSTALS

2.1 High Birefringence Positive Dielectric Anisotropy Nematic Liquid Crystals

2.1.1 *Response Time*

Fast response time plays a key role for reducing the image blur and improving optical efficiency in conventional LCDs and for realizing color sequential displays without color breakup. The dynamic response of LC director can be described by Leslie-Ericksen equation. Under the conditions of single elastic constant and small angle approximations and strong surface anchoring energy, Leslie-Ericksen equation can be simplified as:³⁵

$$k_{ii} \frac{\partial^2 \phi}{\partial Z^2} + \Delta \varepsilon E^2 \sin \phi \cos \phi = \gamma_1 \frac{\partial \phi}{\partial t}, \quad (1)$$

where $\phi(Z,t)$ is the deformation angle of the LC directors, E is the applied electric field, γ_1 is the rotational viscosity of the LC, and k_{ii} is the elastic constant corresponding to the LC alignment. For a LC in In-Plane Switching (IPS) or Fringe-Field Switching (FFS) cell, the electric field mainly induces twist deformation^{5,6}. Thus, k_{ii} can be approximated by k_{22} (twist elastic constant).³⁶ On the other hand, in a vertical alignment (VA) cell k_{ii} is generally a weighted average of k_{11} (splay elastic constant) and k_{33} (bend elastic constant).⁹ But under small angle and single elastic constant approximation, k_{33} dominates and the contribution of k_{11} can be ignored. For a positive $\Delta \varepsilon$ LC in homogeneous (HG) cell, k_{11} dominates. By substituting $E=0$ into Equation (1), we can obtain the equation for the free relaxation process:

$$k_{ii} \frac{\partial^2 \phi}{\partial Z^2} = \gamma_1 \frac{\partial \phi}{\partial t}. \quad (2)$$

By solving Equation (2), we obtain the free relaxation time of the LC directors:

$$\tau_{decay} = \gamma_1 d^2 / k_{ii} \pi^2, \quad (3)$$

where d is the cell gap. The rise time can be described as:

$$\tau_{rise} = (\gamma_1 d^2 / k_{ii} \pi^2) / [(V / V_{th})^2 - 1], \quad (4)$$

where V is the applied voltage, V_{th} is the threshold voltage. For gray-to-gray transitions with a bias voltage V_b , the decay time is modified as follows.³⁷

$$\tau_{rise} = (\gamma_1 d^2 / k_{ii} \pi^2) / |(V_b / V_{th})^2 - 1|, \quad (5)$$

From Equation (5), the gray-level transitions in the vicinities of threshold voltage is much slower than those at high levels. To overcome this bottleneck, we could apply an overdrive³⁸ or undershoot³⁹ voltage method to speed up the LC reorientation⁴⁰.

2.1.2 Thin Cell Approach

Based on Equations (3) and (5), the response time of a nematic LC cell is proportional to the square of cell gap d . A thin cell gap helps to reduce the response time effectively. However, to achieve sufficient phase retardation with a thin cell gap, a high birefringence LC material is required. The LC birefringence is governed primarily by the molecular conjugation. The most effective approach for increasing birefringence is to elongate the π -electron conjugation of the LC compounds.⁴¹⁻⁴³ Conjugation length can be extended by either unsaturated bonds (such as carbon-carbon triple bond) or phenyl rings in the rigid core structure. Due to the photostability concern of carbon-carbon double bonds and triple bonds, conjugated phenyl rings have been commonly used for obtaining high birefringence because of their excellent stability. However, using too many phenyl rings will cause two undesirable drawbacks: 1) its melting point and

heating enthalpy could be too high which lead to a poor solubility, and 2) its viscosity will increase resulting in an increased response time. Therefore, terphenyl could be an optimal structure. For active matrix LCDs, high resistivity and sufficiently large dielectric anisotropy are two additional requirements. Fluoro group provides an excellent resistivity, modest dipole moment, and low viscosity. Therefore, fluorinated terphenyls seem to meet all the desirable properties abovementioned.

Table 1. Chemical structures and properties of the compounds studied. C stands for crystalline phase, S for smectic phase and I for isotropic phase.

Compound	Chemical Structure	PTT (°C)
1. PP(3F)P-3FFF		C63.85 I
2. PP(3F)P-5FFF		C57.3I
3. PPP-3FFF		C118.72 I
4. PPP-5FFF		C95.01 S98.52 I
5. CPP-3F		C106.53N156.17
6. CPP-5F		C102.27N154.42I
7. CPP(3,5F)-3NCS		C54.97N199.48I

Several fluoro-terphenyl compounds (Compounds 1-4) were prepared,⁴⁴ as shown in Table 1.

Three or four fluoro groups are attached to the terphenyl core to increase the dielectric

anisotropy. Compounds 3 and 4 have a fairly high melting point and do not have nematic phase. Their mixtures also do not show any nematic phase. With an extra fluoro substitution in the middle ring, compounds 1 and 2 exhibit a much lower melting point, but still no LC phase. A binary eutectic mixture (designated as Mix1) consisting of 50.34 wt% PP(3F)P-3FFF and 49.66 wt% PP(3F)P-5FFF was formulated.⁴⁵

Unexpectedly, Mix1 shows an enantiotropic nematic phase from 27.82 °C to 31.06 °C. To formulate a wide nematic range mixture using these terphenyl compounds, 21.2 wt% of CPP(3,5F)-3NCS, 7.6 wt% of CPP-3F, and 8.6 wt% of CPP-5F were mixed with 62.6 wt% of Mix1. This new mixture is denoted as M4. As Table 1 shows, compound 7 has a very wide nematic range from 55 °C to 199 °C. Usually, isothiocyanate group has lower resistivity than fluoro group, which would result in a lower voltage holding ratio in TFT-addressed liquid crystal displays. However, fluorinated NCS compounds can still maintain a high resistivity.^{46,47} Besides, with two phenyl rings and –NCS group, the conjugation length is elongated and the birefringence should also be high. M4 has a wide nematic range from 0°C to 83.9°C. The super-cooling effect brings the melting point lower than -60°C. Moreover, together with a large polarizability of fluorinated NCS compounds⁴⁷ and relative high clearing temperature, M4 has a fairly large dielectric anisotropy of 16.8 at room temperature (23 °C).

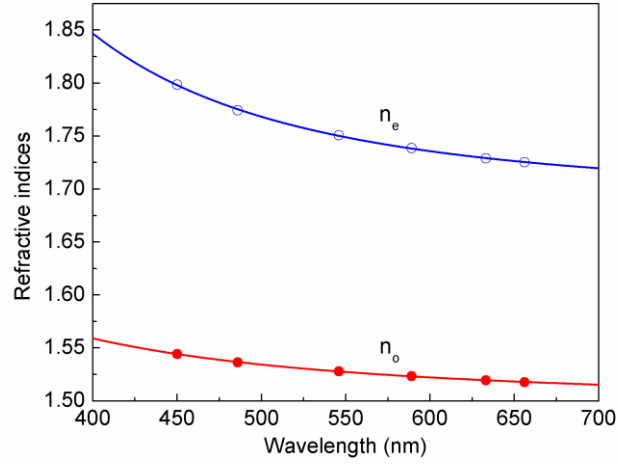


Figure 1. Refractive indices of M4 at different wavelengths: dots are measured data and lines are fittings with Equation (6).

The extraordinary and ordinary refractive indices of M4 at different wavelength were measured at room temperature (23°C). The results are shown in Figure 1. The blue open circles denote the extraordinary refractive indices (n_e), while the red solid circles represent the ordinary refractive indices (n_o). These data are well fitted by the following Extended Cauchy Equation.⁴⁸

$$n_{e,o} = A_{e,o} + \frac{B_{e,o}}{\lambda^2} + \frac{C_{e,o}}{\lambda^4}. \quad (6)$$

The birefringence Δn of the mixture at different temperature was measured through phase retardation of a homogeneous (HG) LC cell sandwiched between two crossed polarizers. The LC mixtures before and after doping were filled into these cells at ~50°C. The cell was mounted in a Linkam LTS 350 Large Area Heating/Freezing Stage controlled by a Linkam TMS94 Temperature Programmer. A 1 kHz square-wave AC signal was applied to the LC cell. A linearly polarized He-Ne laser ($\lambda = 632.8$ nm) was used as probing light source. The light transmittance was measured by a photodiode detector (New Focus Model 2031) and recorded

digitally by a LabVIEW data acquisition system (DAQ, PCI 6110). The VT curves and then the phase retardation (δ) of the VA cells were then measured by the LabVIEW system. The LC birefringence at wavelength λ and temperature was obtained from the phase retardation using the following equation:⁴⁹

$$\delta = 2\pi d\Delta n / \lambda. \quad (7)$$

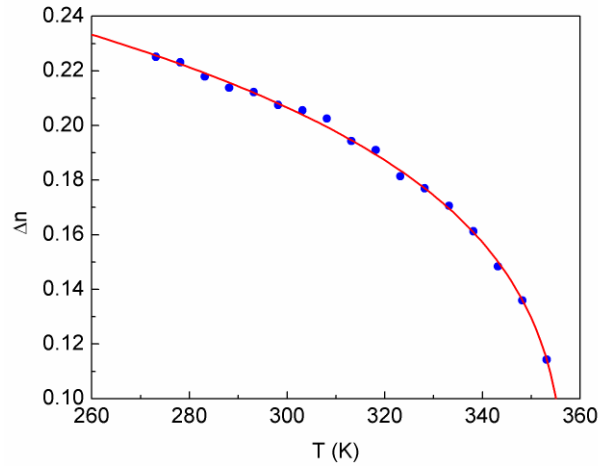


Figure 2. Birefringence of M4: dots stand for measured data and solid line for fitting curve. $\lambda=633$ nm.

The temperature dependent Δn at $\lambda=633$ nm was fitted by Haller's semi-empirical equation⁵⁰

$$\Delta n = \Delta n_o S = \Delta n_o (1 - T / T_c)^\beta, \quad (8)$$

where S is the order parameter, Δn_o is the birefringence when $S=1$, i.e., the completely ordered state, β is a material constant, T is the operating temperature in Kelvin, and T_c is the clearing point of the mixture. This approximation for the order parameter S is valid only when the temperature is not too close to the clearing point. The experimental data and fitting results are shown in Figure 2. Through fitting, we obtained $\Delta n_o = 0.315$ and $\beta = 0.23$. With these two parameters, the birefringence at any temperature can be extrapolated. At room temperature of

23°C, $\Delta n=0.21$ at 633 nm. The birefringence decreases as the wavelength increases and then saturates according to the birefringence dispersion model.²⁹ The measured Δn is 0.223 at $\lambda=550\text{nm}$ and the viscoelastic constant is $21\text{ms}/\mu\text{m}^2$ at 23°C.

With high transmittance and weak color dispersion, TN mode is a good candidate for field sequential color display. For a 90° TN cell, to satisfy Gooch-Tarry first minimum condition^{51,52} the required $d\Delta n \sim 0.48 \mu\text{m}$ at $\lambda=550 \text{ nm}$. Thus, a 2.2- μm cell gap is sufficient when using this high birefringence LC material. However, to achieve a <2ms response time with high Δn LC material, the birefringence should be over 0.3 to achieve light efficiency over 95%.⁵³ Currently, typical TFT-grade LC materials has Δn around 0.1, and some commercially available TFT-grade LC materials have high Δn around 0.2. New LC materials with high Δn , low viscosity, high resistance and good stability are still in urgent need for color sequential display.

2.1.3 Temperature Effect

The switching time of the nematic LC director is proportional to the rotational viscosity. Low viscosity is favorable to achieve fast response time. By measuring the free relaxation (decay) time for a controlled phase change, visco-elastic coefficient (γ_l/k_{ii}) was obtained according to following equation and Equation (3):⁵⁴

$$\delta(t) = \delta_0 \exp(-2t / \tau_0), \quad (9)$$

where δ_0 is the total phase change, γ_l is rotational viscosity, and k_{ii} is the elastic constant (k_{11} : splay elastic constant for HG cell; k_{33} : bend elastic constant for VA cell). As the temperature increases, γ_l decreases exponentially:^{55,56}

$$\gamma_l = c \cdot S \exp(E_a / K_B T), \quad (10)$$

where b is a proportional constant, E_a is the activation energy and K_B is the Boltzmann constant. Meanwhile, the elastic constant k is proportional to S^2 according to Maier-Saupe theory:^{57,58}

$$k_{11} = g \cdot S^2. \quad (11)$$

Thus, the temperature dependent visco-elastic coefficient can be expressed as follows:

$$\frac{\gamma_1}{k_{11}} = \frac{A \cdot \exp(E_a / K_B T)}{(1 - T / T_c)^\beta}, \quad (12)$$

where A is a proportional constant. γ_1/k_{11} decreases quickly with increased temperature. Therefore elevated temperature seems to be an obvious approach to fast response. We measured γ_1/K_{11} at different temperatures and fitted the experimental results by Equation (12), as shown in Figure 3. Here the activation energy is 346.9 meV.

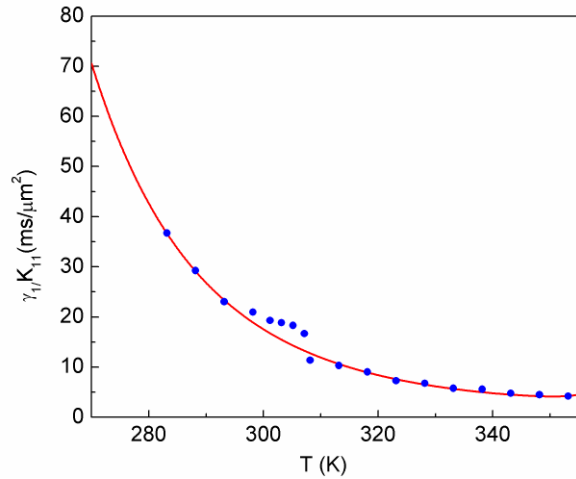


Figure 3. Temperature dependent visco-elastic constant of M4: dots are experimental data and solid line is fitting.

However, when the temperature increases, the birefringence gradually decreases as Equation (8) shows, and vanishes at the clearing point. The reduced Δn would in turn require a thicker cell

gap to achieve enough phase retardation. Therefore a figure of merit (FoM) has been defined to evaluate the overall performance of a LC material:^{59,60}

$$FoM = \frac{(\Delta n)^2}{\gamma_1 / k_{11}} = \omega(\Delta n_o)^2 \left(1 - \frac{T}{T_c}\right)^{3\beta} \exp\left(\frac{-E_a}{K_B T}\right). \quad (13)$$

From Equation (13), FoM is independent of the cell gap employed. Thus, it is commonly used for comparing the performance of a LC compound or mixture. Larger FoM helps reduce the response time. The FoM is expected to exhibit a maximum at the optimal operation temperature, T_{op} . T_{op} can be simply obtained by setting $d(FoM)/dT=0$, and this gives:⁵⁹

$$T_{op} = \frac{E}{6\beta K_B} (\sqrt{1 + 12\beta K_B T_c / E} - 1). \quad (14)$$

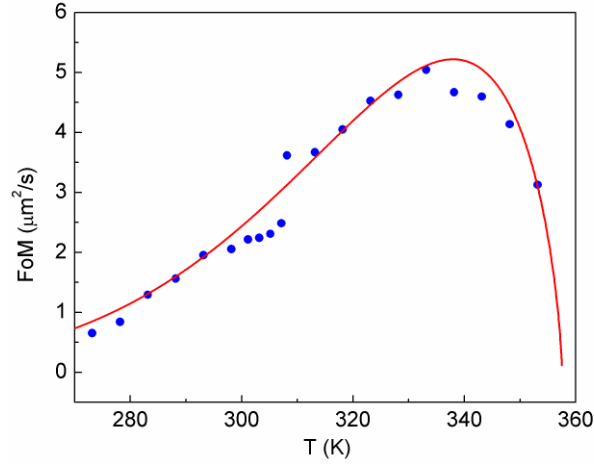


Figure 4. FoM of M4 vs. T . $\lambda=633$ nm. Dots are experimental data and solid line is fitting by Equation (13).

Figure 4 shows the temperature dependent FoM of M4 mixture. The blue dots stand for the measured data and the red curve for the fitting results. M4 has best performance at an elevated temperature of ~ 65 °C. The FoM increases by $\sim 3X$ at 65 °C, compared to that at room temperature, i.e., the response time is improved by $\sim 3X$. It is worth mentioning that at room

temperature, FoM of this mixture is $\sim 2 \mu\text{m}^2/\text{s}$, which is 9X larger than that of MLC-6815. This indicates that we can improve the response time of the LC cell by using a high Δn and low viscosity LC material.

2.1.4 Driving Scheme

Based on Equations (3) and (5), the rise time depends on the applied voltage (V), especially near the threshold region. For some intermediate gray levels, the applied voltage is only slightly above V_{th} . Under such circumstances, the rise time would be very slow. To overcome this, we could apply a high voltage for a short period and then hold the transmittance at the desired gray level. This is the so-called *overdrive* voltage method.³⁸ Meanwhile, during the decay period, when the holding voltage V_b is very close to V_{th} , the decay time will be very slow. To speed up this relaxation process, the voltage is turned off for a short period and then a small holding voltage is applied to keep the LC at the desired gray level. This is the *undershoot* effect.³⁹ With the help of overdrive and undershoot, the LC response time can be reduced by two to three times.

In summary, we have demonstrated a fluoro-terphenyl mixture (M1) with high birefringence, which enables thin-cell-gap approach for achieving fast response while keeping sufficient phase retardation. Due to the narrow nematic range, M1 cannot be used alone. By doping M1 into a low birefringence mixture, the performance can be improved by 2X-3X. More importantly, by using M1 mixture instead of individual homologues, the final mixture's properties, especially clearing point, become predictable. Based on this fluoro-terphenyl mixture, we also formulated a eutectic mixture (M4) with wide nematic range from 0 °C to 83.9°C, high birefringence, large

dielectric anisotropy, and high resistivity, which could be an attractive candidate for active matrix LCDs.

2.2 Advanced Negative Dielectric Anisotropy Nematic Liquid Crystals

2.2.1 *Overview and Recent Progress*

Negative dielectric anisotropy ($\Delta\varepsilon = \varepsilon_{//} - \varepsilon_{\perp} < 0$) liquid crystals (LCs)^{61,62}, in which the parallel permittivity $\varepsilon_{//}$ is smaller than the perpendicular permittivity ε_{\perp} , have been widely used for direct-view and projection displays. The common feature of a negative $\Delta\varepsilon$ LC is that lateral polar substituents induce a dipole moment perpendicular to the principal molecular axis^{63,64}. As described in Hird, et al.⁶⁵, there are several approaches to induce polarity perpendicular to the molecular axis, such as (i) using certain polar linking groups (e.g., ester), (ii) adding a polar unit at an axial position of a cyclohexane ring, (iii) positioning polar unit(s) in lateral positions of an aromatic ring, and (iv) using heterocyclic rings with the heteroatom off-axis. However the off-axis polar group would decrease the aspect ratio of the cylindrical molecular shape and hence tend to disturb the liquid crystal phase stability. Furthermore, the magnitude of the $\Delta\varepsilon$ value will generally be much less than for positive $\Delta\varepsilon$ LCs, and any further use of polar groups to enhance $\Delta\varepsilon$ often causes solubility problems or increases the rotational viscosity. Different off-axis polar groups have been employed to induce perpendicular dipole moment, such as cyano group, or fluoro groups. To avoid image flickering⁶⁶, high resistivity is another crucial requirement for obtaining a high voltage-holding-ratio for active matrix liquid crystal displays (LCDs). A sufficiently large $\Delta\varepsilon$ helps to lower the driving voltage, which in turn lower the power consumption of a mobile display. Fluoro group provides an excellent resistivity, modest dipole

moment, and low viscosity. Laterally fluorinated liquid crystals⁶⁷, i.e. (2,3) difluorinated biphenyl, terphenyl^{44,68} and tolane⁶⁹ usually exhibit a high resistivity and a modest $\Delta\varepsilon$.

A negative $\Delta\varepsilon$ LC can be used in homogeneous alignment or vertical alignment (VA), depending on the electric field direction. In an in-plane switching (IPS) cell^{6,7} or fringe-field switching (FFS) cell³⁻⁵, the electric field is mainly in the lateral direction, while in a VA cell^{8,9} or multi-domain VA (MVA) cell^{10,11}, the field is basically in the longitudinal direction. For mobile displays, IPS or FFS is a common choice because they are more robust to external pressure, which is crucial for touch panels. In comparison with IPS, FFS mode has narrower electrode width and gap to avoid dead zones so that its optical efficiency is higher. Moreover, the capacitor formed by the passivation layer between the pixel and common electrode acts as a storage capacitance. As a result, FFS mode has a larger aperture ratio. Recently, it is found that the FFS mode with a negative $\Delta\varepsilon$ LC (n-FFS) exhibits several advantages over the p-FFS in higher transmittance, single gamma curve, and cell gap insensitivity⁵. A simple VA cell has been employed in liquid-crystal-on-silicon (LCOS) for data projectors because of its unprecedented contrast ratio⁷⁰, while MVA is a common choice for wide-view LCD TVs. In this paper, we will review recent progress on the negative $\Delta\varepsilon$ LC development for FFS, VA LCOS and MVA display modes.

Based on Equation (3), the response time of an FFS or VA cell is proportional to the visco-elastic coefficient of the LC material employed and d^2 . A thin cell gap would help to reduce the response time effectively. However, to maintain adequate phase retardation with reduced cell gap, a high Δn LC is required. Similarly, terphenyl⁷¹ could be an optimal structure for the thin-

cell-gap VA LCOS. However, for FFS or MVA the required $d\Delta n$ is about 330-360 nm. If the cell gap is 3-4 μm , then $\Delta n \approx 0.09-0.12$; low viscosity is the major concern.

2.2.2 Negative $\Delta\epsilon$ LCs for FFS Mode

FFS^{4,72,73} mode has been widely used for mobile displays, such as smartphones and tablet computers. Low power consumption for long battery life, wide viewing angle for many simultaneous observers, high resolution for Retina display, and pressure-resistance for touch screen are the key requirements. In FFS, the electric-field-induced molecular reorientation takes place mainly in the horizontal direction. Presently, most FFS LCDs use positive $\Delta\epsilon$ LCs. The primary reason is that it is relatively easy to obtain a large $\Delta\epsilon$ (~ 10) while keeping a low viscosity. Large $\Delta\epsilon$ helps to reduce operation voltage while low viscosity helps to shorten response time. However, positive $\Delta\epsilon$ LC-based FFS (p-FFS) has some problems: 1) its peak transmittance is limited to $\sim 88\%$; 2) the voltage-dependent transmittance (VT) curves do not overlap well for RGB colors, thus three gamma curves are required, which increases the complexity of driving electronics; 3) the VT curves are sensitive to the cell gap, and 4) a small but noticeable image flickering due to splay- and bend-induced flexoelectric effect.⁷⁴

To overcome these problems, recently we have reported a n-FFS mode using a high performance negative $\Delta\epsilon$ LC⁵. The n-FFS mode has been investigated previously,^{4,7,75} but mainly by simulations. In this session, we compare the results of four different negative $\Delta\epsilon$ LC mixtures with relatively high Δn and low viscosity. The phase retardation effect on peak transmittance and on-state voltage is also investigated.

2.2.2.1 Low Viscosity Negative $\Delta\epsilon$ LCs Development

For high yield manufacturing, it is desirable to keep the cell gap above $3\mu\text{m}$. Thus, the required Δn is around 0.12. Previously we reported a high performance n-FFS with UCF-N1,⁵ consisting of 60 wt. % MLC-6882, 18% lateral difluoro akoxy-biphenyl, 17% lateral difluoro cyclohexane-biphenyl⁶⁷ and 5% bicyclehexane compounds. We compare our results with MLC-6882 and a positive $\Delta\epsilon$ LC (UCF-P1) with $\Delta\epsilon=10$ while other properties are assumed to be the same as UCF-N1.⁷⁶

Table 2. Physical properties of the liquid crystals studied (measured at $\lambda=633$ nm, $T\sim 22$ °C and $f=1$ kHz).

LC Mixture	T_c (°C)	Δn (633nm)	Δn (550nm)	γ_1/k_{33} (ms/ μm^2)	γ_1 (mPa.s)	$\Delta\epsilon$
MLC 6882	69	0.097	0.098	8.44	108	-3.1
UCF-N1	73.3	0.116	0.119	9.06	122.8	-3.82
UCF-P1	73.3	0.116	0.119	9.06	122.8	10
HAV	89.5	0.108	0.110	6.97	98.53	-3.79
ZOC	79	0.101	0.103	5.60	93.34	-4.36
UCF-N2	75	0.112	0.117	6.00	94.71	-3.77

Table 2 includes three new negative $\Delta\epsilon$ LCs to be considered for FFS mode: HAV (HAV-634117, HCCH, China), ZOC (ZOC-7003xx, JNC, Japan), and UCF-N2. From Table 1, JNC ZOC has the lowest visco-elastic coefficient γ_1/k_{33} , but its Δn is slightly too small. For LCOS, the panel size is small; so a submicron cell gap can be controlled without too much difficulty.

However, a high Δn LC is needed to maintain $d\Delta n \sim 165$ nm. To obtain high Δn , we first formulated a binary LC mixture (Mix A) with two lateral difluoro-terphenyl homologs.⁷⁷ Its physical properties are: $\Delta n = 0.235$ (at $\lambda = 633$ nm and $T \sim 22^\circ\text{C}$), $\Delta \epsilon = -1.8$ and clearing temperature $T_c \sim 112.3^\circ\text{C}$. Next, we doped 10% Mix A and 5% biphenyls to ZOC. The final mixture is denoted as UCF-N2. Table 2 lists the physical properties of the six LC mixtures studied. The dielectric anisotropy was determined by measuring the capacitance of a homogeneous cell and a homeotropic LC cell.^{54,78}

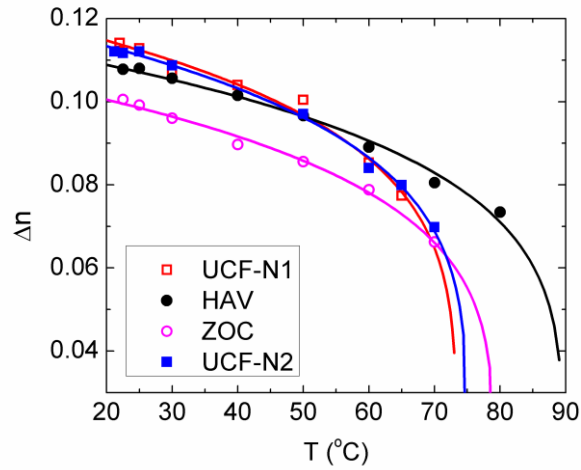


Figure 5. Temperature dependent Δn of UCF-N1, HAV, ZOC and UCF-N2 at $\lambda = 633$ nm.

We evaluated birefringence by measuring the phase retardation of a VA cell sandwiched between two crossed polarizers.⁴⁹ The VA cell has strong anchoring energy and cell gap $d \sim 9$ μm . A 1 kHz square-wave AC voltage signal was applied to the LC cell. A He-Ne laser ($\lambda = 633$ nm) and a tunable Argon ion laser ($\lambda = 457$ nm, 488 nm and 514 nm) were used as probing beams. The Δn of UCF-N1, HAV, ZOC and UCF-N2 was measured from 22°C (RT) to a temperature close to T_c . Results are plotted in Figure 5. Dots represent the measured data and solid lines are

the fitting curves using Equation (8). At RT and $\lambda = 633$ nm, the Δn of ZOC, HAV and UCF-N2 is 0.101, 0.108 and 0.113, respectively.

For a full color display, we need to know the birefringence at red, green and blue wavelengths. Figure 6 depicts the measured birefringence dispersion of UCF-N1, HAV, ZOC and UCF-N2. Dots represent the measured data and solid lines are the fitting curves using the single-band birefringence dispersion model:²⁹

$$\Delta n = G\lambda^2\lambda^{*2} / (\lambda^2 - \lambda^{*2}), \quad (15)$$

where G is a proportionality constant and λ^* is the average resonant wavelength of the LC. Through fitting, we obtained $G = 2.10 \mu\text{m}^{-2}$, $2.57 \mu\text{m}^{-2}$, $3.40 \mu\text{m}^{-2}$ and $2.13 \mu\text{m}^{-2}$ and $\lambda^* = 218.4$ nm, 194.6 nm, 165.7 nm and 215.8 nm for UCF-N1, HAV, ZOC and UCF-N2, respectively. With a higher Δn , UCF-N1 and UCF-N2 have a longer resonant wavelength as expected. With these fitting parameters, we can obtain the birefringence at a desired wavelength by Equation (15).

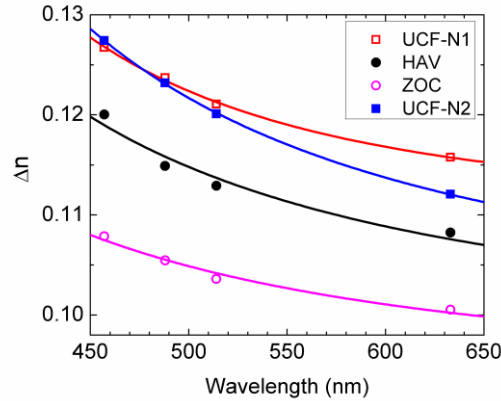


Figure 6. Birefringence dispersion of the four LC mixtures studied.

From the relaxation time measurement of the VA cell, we can obtain the visco-elastic coefficient (γ_1/k_{33}).⁵⁴ We measured γ_1/k_{33} at different temperatures and fitted the experimental

results with Equation 12), where γ_1/k_{11} is replaced by γ_1/k_{33} for the VA cell. The results are shown in Figure 7(a).

Through fittings, we obtained $E_a = 279, 270.1, 260.7$ and 274.5 meV for UCF-N1, HAV, ZOC and UCF-N2, respectively. The overall performance of the negative LC was evaluated based on a figure of merit (FoM) defined as $(\Delta n)^2 / (\gamma_1 / k_{33})$. The temperature dependent FoM is similar to positive LCs, shown in Equation (13). Figure 7(b) depicts the measured data and fitting curve. Near RT, UCF-N2 possesses the highest FoM , hence the fastest response time for the same phase retardation. Indeed, as will be shown later, the calculated response time of an n-FFS cell using UCF-N2 is 32% faster than that of UCF-N1. At 22°C, the FoM of UCF-N2 is $2.05 \mu\text{m}^2/\text{s}$, and it increases to $3.62 \mu\text{m}^2/\text{s}$ at 50°C. As the temperature increases, visco-elastic coefficient decreases more quickly than birefringence initially, resulting in an increased FoM . As T approaches T_c , Δn decreases more quickly than γ_1/k_{33} leading to a sharply declined FoM , as Figure 7(b) depicts. High T_c is also important for wide operating temperature range.

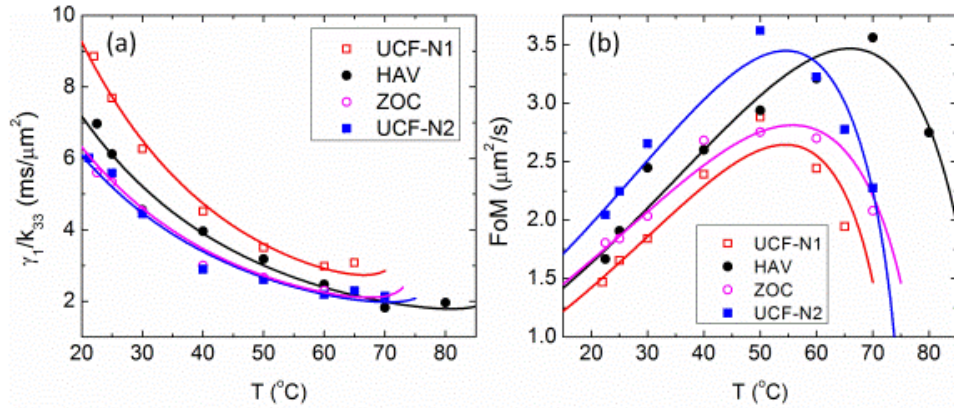


Figure 7. Temperature dependent (a) γ_1/k_{33} and (b) FoM of the four LCs studied.

2.2.2.2 Device Configuration

The electro-optic properties of both n-FFS and p-FFS are calculated by a commercial LCD simulator DIMOS.2D and the extended Jones matrix.⁷⁹ As will be shown later, the preferred $d\Delta n$ value for achieving high transmittance at $\lambda=550$ nm and fast response time is ~ 360 nm for n-FFS and ~ 380 nm for p-FFS. This difference results from the more efficient LC director reorientation in the n-FFS. To make a fair comparison between n-FFS and p-FFS, we use the same electrode width $w=2$ μm and gap $l=3$ μm , same pretilt angle (2°) but the rubbing angle is 10° and 80° respectively w.r.t. the horizontal axis.

Figure 8(a) and 4(b) show the device configuration, calculated equal-potential lines and LC director deformation in a voltage-on state. The passivation layer between the pixel and common electrodes is SiO_x whose thickness is $d_p=250$ nm and dielectric constant is $\epsilon_p=4.5$.⁸⁰ The cell is sandwiched between two crossed linear polarizers, and the transmission axis of the bottom polarizer is parallel to the rubbing direction. Thus, the transmittance at a given position and voltage V can be expressed as:^{3,49}

$$T / T_0 = \sin^2(2\Psi(V)) \sin^2(\pi d \Delta n_{\text{eff}}(V) / \lambda), \quad (16)$$

where $\Psi(V)$ is the voltage dependent azimuthal component of the angle between the polarizer and LC director's optic axis, T_0 is the transmitted light through parallel polarizers and Δn_{eff} is the effective birefringence of LC at voltage V and wavelength λ . Please note that the electric field in a FFS cell is not uniform. So, the transmittance at each position may not be the same. We have to do the spatial averaging for each pixel. The dark state of a FFS cell happens when $V=0$, and the transmittance reaches a maximum when the LC directors are reoriented by 45° .

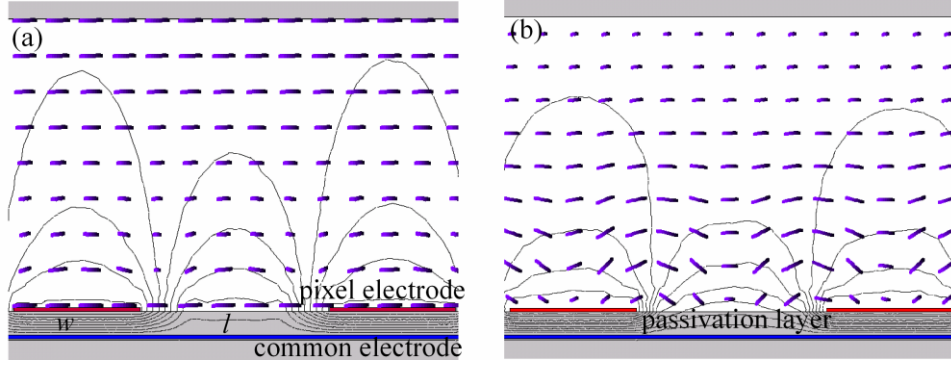


Figure 8. Device configuration of FFS structure, equal-potential lines, and LC director deformation in voltage-on state of (a) n-FFS and (b) p-FFS.

2.2.2.3 Phase Retardation Effect

Both peak transmittance and on-state voltage (V_{on}) are dependent on the phase retardation, or $d\Delta n/\lambda$ of the FFS cell. Figure 9 depicts the calculated T_p and V_{on} at different $d\Delta n/\lambda$ values for both n-FFS (with UCF-N1) and p-FFS (with UCF-P1). For n-FFS, as $d\Delta n/\lambda$ increases from 0.35 to 1.1, T_p climbs to a peak of 98.1% at $d\Delta n/\lambda \approx 0.67$ and then gradually decreases. Meanwhile, V_{on} decreases to a minimum at $d\Delta n/\lambda \approx 0.7$ and then bounces back. Since green light is the major component of white light, we optimize the cell gap at $\lambda = 550$ nm. Therefore, for n-FFS we choose $d\Delta n \sim 360$ nm for $\lambda = 550$ nm, in order to achieve high transmittance and fast response time. However, for p-FFS, T_p and V_{on} increases continuously in the $d\Delta n/\lambda$ range studied. The insufficient phase retardation results from the large tilt angle of the directors in the p-FFS, because the positive $\Delta\epsilon$ LC directors tend to align parallel to the electric fields. Compromising the performance between transmittance, V_{on} and response time, we chose $d\Delta n \sim 380$ nm at $\lambda = 550$ nm as the optimal value for p-FFS.

Moreover, for n-FFS, both T_p and V_{on} are quite inert to the $d\Delta n/\lambda$ variation in the 0.60-0.78 range, which provides a reasonable manufacturing tolerance. By contrast, in the same range the V_{on} of p-FFS climbs almost linearly from 4V to 5.2V and T_p increases from 82% to 91.7%.

However for $d\Delta n/\lambda > 0.7$, T_p of p-FFS gradually saturates and becomes insensitive to $d\Delta n/\lambda$. If $d\Delta n/\lambda$ is optimized > 0.82 , T_p is quite insensitive to cell gap or wavelength. In order to achieve large $d\Delta n/\lambda$, either a thick cell or high Δn LC can be employed. Thick cell would lead to slow response time while high Δn LCs usually exhibit large viscosity also resulting in slow response time. On the other hand, V_{on} becomes very high for larger $d\Delta n/\lambda$, which is not desirable for power consumption reduction. Moreover, the significant variation on V_{on} for different $d\Delta n/\lambda$ indicates that V_{on} is very sensitive to cell gap or wavelength.

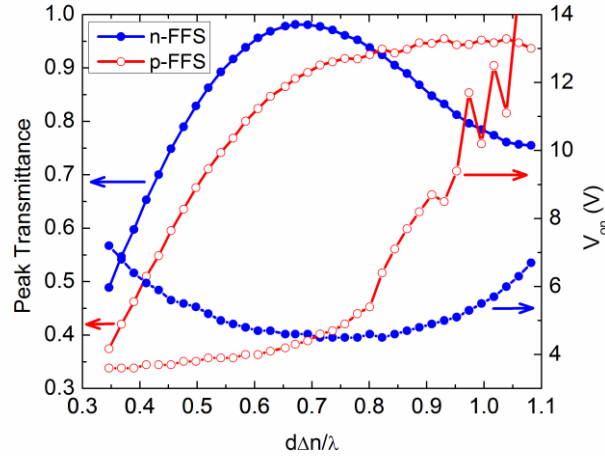


Figure 9. T_p and V_{on} at different $d\Delta n/\lambda$ for n-FFS and p-FFS.

2.2.2.4 Wavelength Effect

To achieve high transmittance, we optimize the cell gap for $\lambda=550\text{nm}$. However, $d\Delta n/\lambda$ varies for RGB colors due to the change in λ and birefringence dispersion, as shown in Figure 6. For a

normal dispersive material, Δn is larger at blue than red. Thus, the phase retardation for blue will be larger than the optimized value for green, but red will be smaller. Larger birefringence dispersion would lead to more noticeable deviation from the optimal phase retardation and hence lower the peak transmittance. To study the birefringence dispersion effect on the transmittance for RGB ($\lambda=650, 550$ and 450 nm respectively) colors, we calculated the VT curves of n-FFS with three different LCs: UCF-N0, UCF-N1 and UCF-HB, as shown in Figure 10(a)-(c). UCF-N0 is an imaginary material; it has the same properties as UCF-N1 but without dispersion at all. UCF-HB is a high birefringence negative $\Delta\varepsilon$ LC, whose $\Delta n=0.208, 0.218$ and 0.254 for RGB colors, respectively. For UCF-N0, $d\Delta n/\lambda(B)=0.8$ and $d\Delta n/\lambda(R)=0.55$. From Figure 9, $T_p(B)$ and $T_p(R)$ would drop from 98% to 91%, which is consistent with the calculated VT curves of UCF-N0 for RGB colors, as depicted in Figure 10(a). Moreover, both RGB colors have nearly the same V_{on} . The inset in Figure 10(a) depicts the normalized VT curves and they overlap amazingly well. Thus, a single gamma curve driving can be realized for n-FFS, which would simplify the driving circuit. This property holds true for UCF-N1 and UCF-HB. From Figure 9, V_{on} is relatively insensitive to $d\Delta n/\lambda$ in the range of 0.55-0.9. The peak transmittance of UCF-N1 reaches $\sim 98\%$ ($\lambda=550$ nm) at $V_{on}=4.6V$. As the birefringence dispersion gets larger, $T_p(B)$ and $T_p(R)$ drop further to 85% and 89% for UCF-N1, respectively. For UCF-HB, $T_p(B)$ decreases to 70%, since $d\Delta n/\lambda$ deviates from the optimized value too much.

For comparison, we also calculate the VT curves of a p-FFS cell using UCF-P1 ($d=3.19\mu m$). Let's call it FFS-P1. Results are shown in Figure 10(d). The dispersion of VT curves for RGB colors is quite noticeable. At 550nm, T_p reaches $\sim 88\%$ and $V_{on}=4.4V$. The V_{on} for 650nm is 4.0V

and $T_p=78.3\%$. For $\lambda=450\text{nm}$, T_p can reach 88.1%, but at a much higher voltage (6.8V). The inset in Figure 10(d) depicts the normalized VT curves. Obviously, they do not overlap well. Thus, three different gamma curves are needed to drive the RGB pixels.

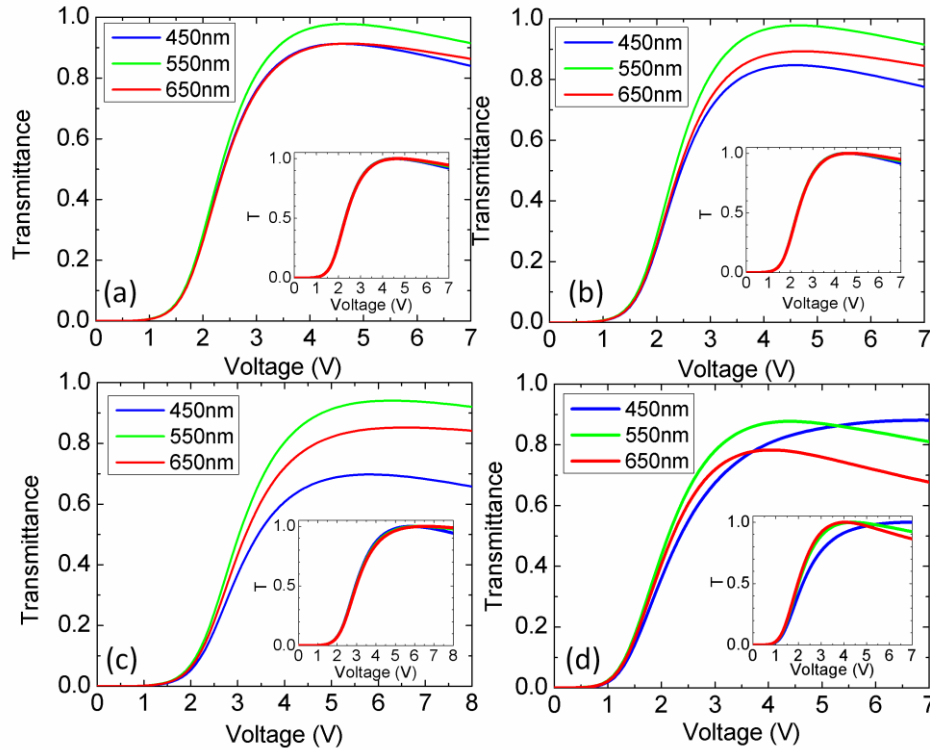


Figure 10. VT curves for FFS cell using (a) UCF-N0 (b) UCF-N1 (c) UCF-HB and (d) UCF-P1 for RGB colors. Inset plots show the normalized VT curves.

2.2.2.5 Director Deformation Distribution

In order to better understand the transmittance and gamma curve differences, we investigate the LC twist angle and tilt angle distributions for both FFS-N1 (n-FFS cell using UCF-N1) and FFS-P1 at five positions (A to E as Figure 11(a) shows). To obtain maximum transmittance, the twist angle should occur at 45° , as Equation (16) shows. From Figure 11, the LC directors are largely twisted near the bottom of the cell ($z/d < 0.4$) by the electric field and gradually reoriented

back to the rubbing direction due to the strong anchoring force provided by the top surface. For FFS-N1, the maximum twist angle from the initial rubbing direction is around 46° at A and E. The tilt angle at A and E is close to 0, which contributes effectively to the phase retardation. At B, C, and D, the horizontal electric field is stronger and the maximum twist angle is $\sim 55^\circ$. Meanwhile, the tilt angle at $z/d \sim 0.1$ is $\sim \pm 10^\circ$, which would slightly decrease the phase retardation and compensate the over twist. Moreover, the on-state n-FFS cell is like two cascaded TN cells⁸⁰ due to the small tilt angle. As a result, polarization rotation effects dominate and the color dispersion is suppressed. Because of the small tilt angle, the V_{on} for RGB color is mainly determined by the twist angle, according to Equation (16), resulting in a single gamma curve.

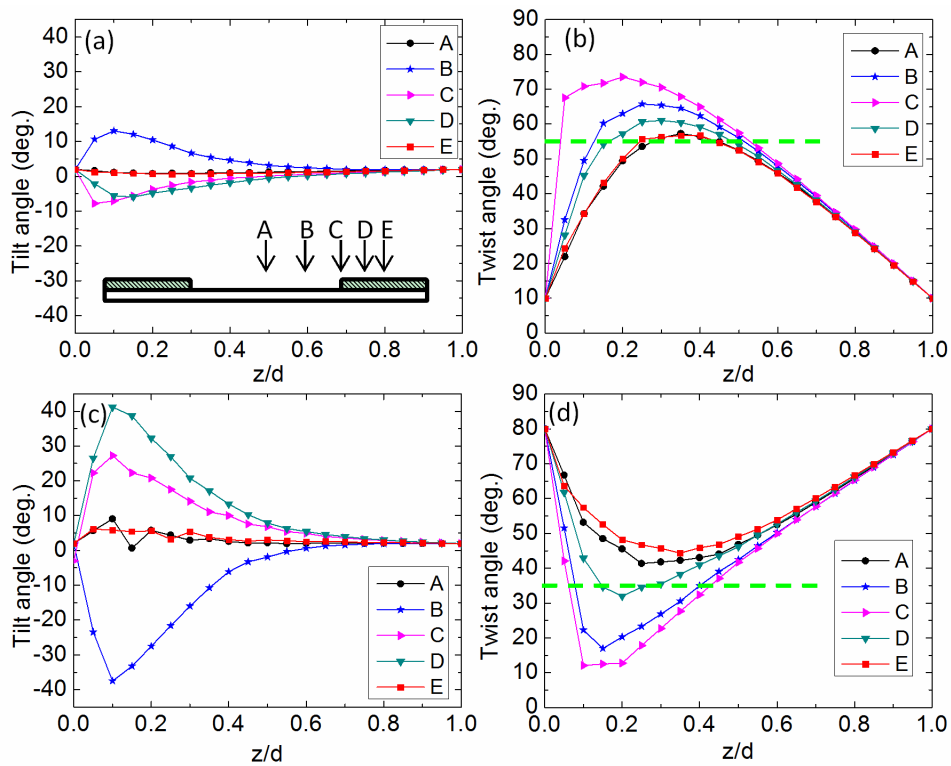


Figure 11. Simulated twist angle distribution of (a) FFS-N1 and (c) FFS-P1; Tilt angle distribution of (b) FFS-N1 and (d) FFS-P1.

In contrast, the maximum twist angle of FFS-P1 is either larger than 63° (B and C) or smaller than 38° (A and E). The over- or under-twist leads to inefficient phase retardation. Only at position D, the maximum twist angle is about 48° , however the tilt angle is about 41° at $z/d=0.1$. The large tilt angle caused by the strong vertical field dramatically decreases the effective birefringence and hence the peak transmittance. Meanwhile, with a large tilt angle at positions B, C, and D, the phase retardation effect (which is wavelength sensitive) becomes quite obvious, resulting in severe wavelength dispersion. Also from Figure 11(b), splay and bend deformation occurs and electric polarization is induced, which is known as flexoelectric effect⁷⁴. The light transmittance would change slightly from negative to positive frames, resulting in a small image flickering. By contrast, this effect is negligible in n-FFS due to the small tilt angle.

As Figure 10 shows, FFS-P1 has a lower threshold voltage than FFS-N1 because its $\Delta\varepsilon$ (+10) is much larger than that of UCF-N1 (-3.82), assuming their k_{22} is the same. However, the on-state voltage of FFS-P1 ($V_{on}\sim 4.4V$) is nearly the same as that of FFS-N1 (4.6V). This can be explained by the LC director distributions shown in Figure 11(a)-(d). FFS-N1 has more efficient twist angle ($\sim 45^\circ$) and smaller tilt angle than FFS-P1 so that its effective birefringence is higher. As a result, a smaller voltage swing ($\Delta V = V_{on} - V_{th}$) is needed to reach the peak transmittance. Therefore, FFS-N1 has a comparable V_{on} to FFS-P1, although its $\Delta\varepsilon$ is much smaller.

2.2.2.6 Reducing V_{on}

Power consumption of a mobile display is a critical issue as it affects the battery life. The power consumption of a LCD originates from two parts: electronic and backlight. Generally speaking, the power consumption is proportional to the pixel resolution, circuit frame rate,

capacitance, and square of the operation voltage. Therefore, for a given resolution and frame rate, the power consumption is closely related to the optical efficiency and operation voltage.

To lower V_{on} , one approach is to decrease the rubbing angle.^{3,81} The tradeoff is slower rise time, although the decay time remains almost the same. In FFS mode, the capacitor formed by the passivation layer between the pixel and common electrode acts as a storage capacitor ($C_s \sim \epsilon_p A_{pixel}/d_p$), which is in parallel to the LC capacitor. Another possible approach to lower V_{on} is to use a thin and large ϵ_p dielectric layer for increasing C_s and reducing the voltage shielding effect.⁸² For example, if we reduce the SiO_x layer thickness from 250 nm to 100 nm, then V_{on} would decrease from 4.6V to 3.9V for FFS-N1. If we use 100 nm Si_3N_4 passivation layer ($\epsilon_p=6.5$), V_{on} drops to 3.8V. A tradeoff is the increased charging time resulting from the increased C_s . But for a high resolution mobile display, its pixel size is small so that C_s can still be kept relatively small for quick addressing.

From material aspect, a straightforward way to reduce V_{on} is to increase $\Delta\epsilon$. As shown in Figure 12, as $\Delta\epsilon$ increases, the V_{on} of n-FFS decreases dramatically initially and then gradually saturates for both 250-nm SiO_x layer (solid circle) and 100-nm Si_3N_4 layer (open circle). The two sets of data points are well fitted by the following empirical equation:

$$V_{on} = \rho \cdot \pi \sqrt{\frac{k_{22}}{\epsilon_0 \Delta\epsilon}}, \quad (17)$$

where ρ is a device constant related to the configuration and the passivation layer. From the fitting, we obtained $\rho=3.4$ and 2.83 for the 250-nm SiO_x layer and 100-nm Si_3N_4 layer, respectively. Smaller ρ indicates less voltage shielding effect and more efficient driving. The

deviation for large $\Delta\epsilon$ comes from the larger dielectric constant mismatch between liquid crystal and SiO_x , resulting in severe voltage shielding effect. On the other hand, further increasing $\Delta\epsilon$ could substantially increase the viscosity and result in a slower response time. Meanwhile, the reduction in V_{on} would gradually saturate, as Figure 12 shows. Thus, a too large $\Delta\epsilon$ is not desirable for n-FFS.

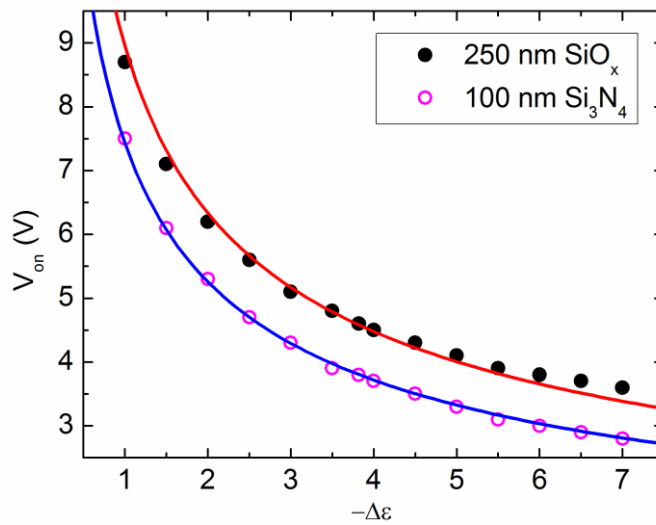


Figure 12. $\Delta\epsilon$ effect on the V_{on} of n-FFS under two types of passivation layers.

2.2.2.7 Response Time

Both rise time and decay time are calculated between the 10% and 90% transmittance change. For FFS-P1 with $d=3.19\ \mu\text{m}$, the simulated [rise time, decay time] is [23.8ms, 25.7ms]. For the n-FFS cell with MLC-6882 ($d=3.66\ \mu\text{m}$ and $V_{on}=4.5\text{V}$) the simulated [rise time, decay time] is [23.4ms, 34.8ms]. With our UCF-N1 ($d=3.02\ \mu\text{m}$), the calculated [rise time, decay time] is [16.2ms, 24.1ms]. Our UCF-N1 has faster response time than MLC-6882 because of its thinner cell gap. On the other hand, UCF-N1 has faster response time than FFS-P1 due to its more uniform twist and tilt angles. A lower viscosity LC would further reduce the response time. For

example, if we use a lower viscosity LC, such as UCF-N2, the calculated [rise time, decay time] decreases about 30% to [10.9ms, 16.5ms]. Continuous effort for lowering the viscosity of negative $\Delta\epsilon$ LCs is highly desirable from the viewpoint of faster response time.

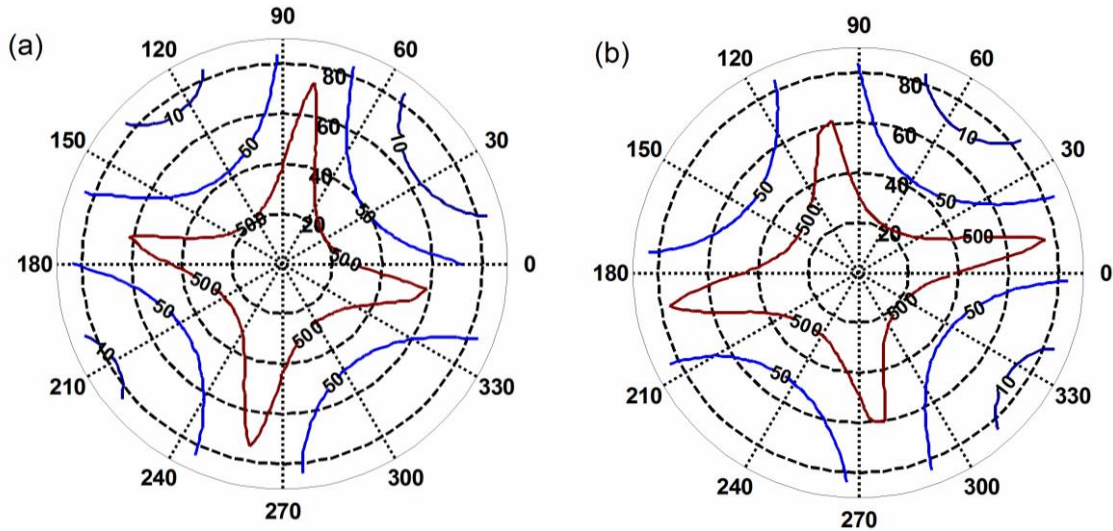


Figure 13. Simulated isocontrast plots for: (a) FFS-P1 and (b) FFS-N1.

2.2.2.8 Viewing angle

We also compare the viewing angle for the FFS cells using both positive and negative $\Delta\epsilon$ LCs. Figure 13(a) and (b) show the isocontrast plot for FFS-P1 and FFS-N1. Since their dark states are similar due to the same alignment, the contrast ratio (CR) is mainly determined by the bright state. FFS-N1 has a slightly better isocontrast performance due to its higher transmittance and more uniform in-plane director twist and small tilt angle in the bright state. Due to the homogeneous alignment and horizontal molecular orientation, n-FFS has intrinsic wide viewing angles. To achieve wide view, various compensation films for FFS mode have been developed.^{83,84} With one biaxial film, a CR over 100:1 can be achieved in almost the entire

viewing zone ($\pm 80^\circ$). To further widen the viewing angle, multi-domain structures can be considered.⁷²

We have demonstrated a new negative $\Delta\varepsilon$ LC mixture with modest birefringence and low viscosity for FFS LCDs. Our n-FFS shows superior performances to p-FFS in following aspects: 1) higher transmittance (98% vs. 88%); 2) single gamma curve vs. 3 gamma curves for RGB pixels; 3) both on-state voltage and peak transmittance are less sensitive to cell gap variation ($d\Delta n/\lambda=0.6-0.78$), 4) faster response time due to a slightly thinner cell gap and more uniform LC twist and tilt angles, and 5) comparable on-state voltage to p-FFS although the LC mixture has a smaller $\Delta\varepsilon$ (-3.8 vs. +10). Therefore, n-FFS has potential to replace p-FFS for next-generation mobile displays or even TV applications. Moreover, due to the homogeneous alignment and horizontal molecular orientation, n-FFS has intrinsic wide viewing angles. In terms of fast response time, we have demonstrated a low viscosity negative $\Delta\varepsilon$ LC mixture (UCF-N2, $\gamma_1=94$ mPa.s and $\Delta n\sim 0.12$) for n-FFS with a 3- μm cell gap.

2.2.3 Negative $\Delta\varepsilon$ LCs for VA Mode

Two types of VA cells will be discussed here: single domain VA LCOS for projection displays and multi-domain VA for direct-view LCD TVs.

2.2.3.1 LCOS

Single domain VA has been extensively used in LCOS for projection displays because of its unprecedented contrast ratio (CR)⁷⁰. To enable color sequential projection display,^{14,85,86} which requires only a single monochrome LCD panel so that the optical system is much simpler than that using three panels, fast response time (< 1 ms) is critically needed in order to suppress color

breakup. To achieve submillisecond response time, several approaches have been proposed, such as thin VA LCOS cell,^{8,9} mixed-mode twisted nematic (MTN) cell⁸⁷ and ferroelectric cell.⁸⁸ Among these methods, thin VA LCOS is attractive because of its high CR and fast response time. However, fringing field degrades the contrast ratio and reduces the display brightness.⁸⁹ A straightforward way to suppress fringing field effect is to reduce the cell gap. A major challenge for the thin cell approach is the need of a high birefringence and low viscosity LC. For a VA LCOS, the required $d\Delta n$ is ~ 165 nm (at $\lambda=550$ nm) in order to achieve high reflectance at a low voltage (<5 V).⁹⁰

In projection displays, high power arc lamp or LED lamp is commonly used as light source. Because of heating effect, the LCOS panel is usually operated at $40-50^\circ\text{C}$. As the temperature increases, both birefringence and visco-elastic coefficient decrease. The former vanishes at T_c . Therefore, it is important to design a LC with high T_c ($\gg 50^\circ\text{C}$). In an LCOS, the electric field is in the longitudinal direction. To realize the electro-optic effect of a VA cell, we need a negative $\Delta\varepsilon$ LC. To achieve high resistivity, fluorinated LCs are commonly used as mentioned earlier⁶⁷. However, some laterally difluoro high Δn compounds are difficult to align, especially at elevated temperatures.⁷⁷ A poor LC alignment leads to a low contrast ratio.

UV stability is another critical issue for a high Δn LC due to its relatively long conjugation length. In an LCOS projector, the arc lamp is relatively bright. Although filters are used to block the unwanted UV and infrared lights from the lamp, residual UV contents could still decompose the LC materials if the molecular structures are not intrinsically stable.

2.2.3.1.1 LC Materials

In experiment, we doped 40 wt% of lateral difluoro alkoxy- biphenyls, -cyclohexane phenyls, -cyclohexane biphenyls⁹¹ into the Mix A host in order to increase $\Delta\varepsilon$ while keeping low viscosity. A large $\Delta\varepsilon$ leads to a low driving voltage. For convenience, we name this mixture as UCF-N3. An excellent dark state was achieved in the entire nematic range. The clearing point is $T_c \sim 93.2^\circ\text{C}$.

2.2.3.1.2 Physical Properties

We first measured the dielectric anisotropy of UCF-N3 at $f=1$ kHz. Results are: $\Delta\varepsilon = -3.74$ at 23°C and -2.91 at 50°C . Next, we measured the temperature dependent Δn of UCF-N3 at $\lambda=633$ nm from 25°C to 90°C . Results are plotted in Figure 14(a), where blue dots represent the measured data and red solid line is the fitting curve using Equation (7). Through fitting, we obtained $\Delta n_0=0.265$ and $\beta=0.177$.

To investigate the electro-optical performances at RGB colors, we measured the birefringence dispersion of UCF-N3 at 50°C ; the intended operation temperature for an LCOS projector. Results are shown in Figure 14(b); here dots are the measured data and solid line represents fitting results using Equation (15). From fitting we obtained $G=2.64\text{E-}6 \mu\text{m}^{-2}$ and $\lambda^*=241.1$ nm. With higher Δn , UCF-N3 has longer λ^* than the previous mentioned mixtures for FFS. With these parameters and through Equation (15), the birefringence at any wavelength can be calculated. For example, we find $\Delta n=0.19$ at $\lambda=550\text{nm}$ and 50°C . Thus, for a VA LCOS we need $d=0.93 \mu\text{m}$ to achieve $\sim 100\%$ reflectance (normalized to parallel polarizers) at a relatively low operating voltage ($<5\text{V}$). Although challenging, ferroelectric LCOS with $d\sim 0.8 \mu\text{m}$ has been commercialized.

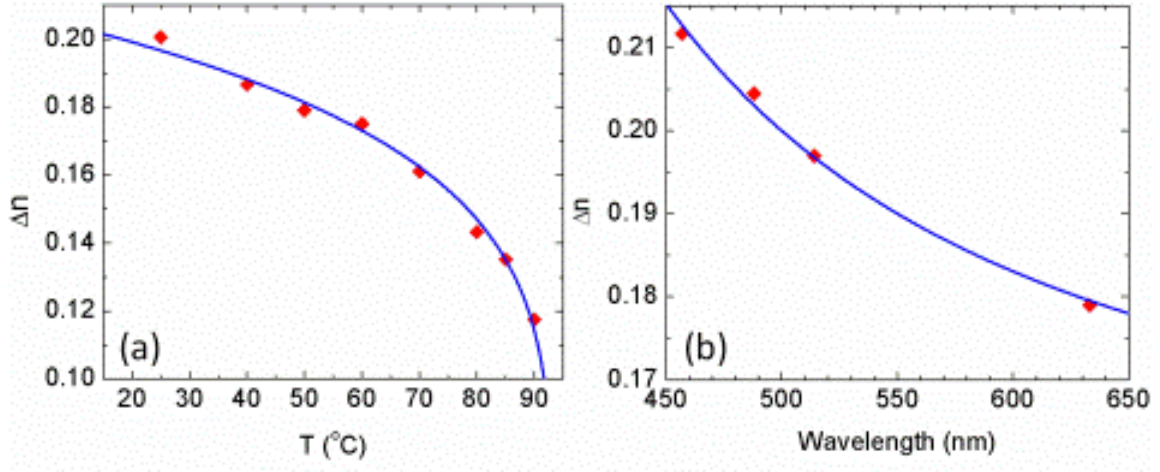


Figure 14. (a) Temperature dependent Δn of UCF-N3 at $\lambda=633\text{nm}$. (b) Wavelength dependent Δn of UCF-N3 at $T=50$ $^{\circ}\text{C}$

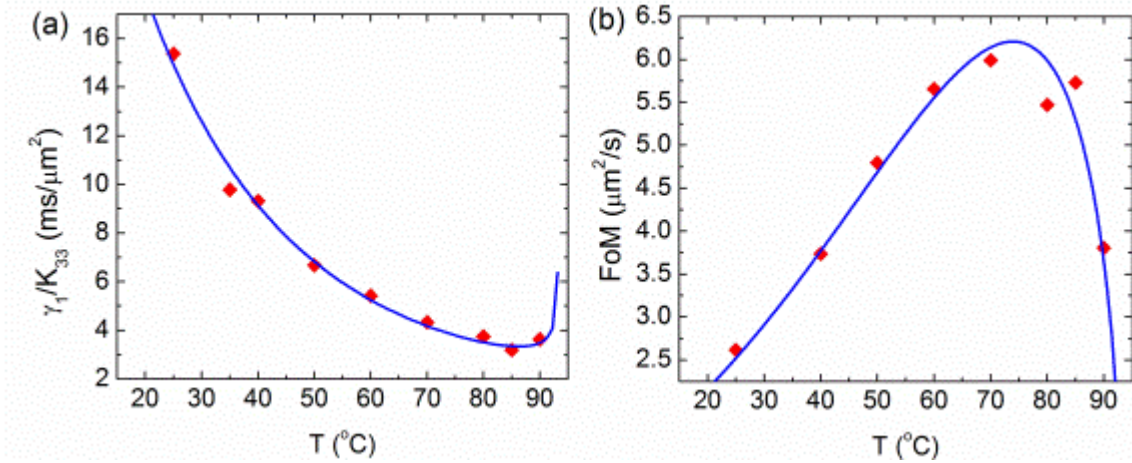


Figure 15. Temperature dependent (a) γ_1/K_{33} and (b) FoM of UCF-N3.

We also measured the γ_1/K_{33} of UCF-N3 at different temperatures and fitted the experimental data with Equation (12), as shown in Figure 15(a). Here the activation energy is $E_a=286.9$ meV, which is larger than that of UCF-N2 developed for FFS. Usually higher birefringence involves longer conjugation length and hence higher viscosity, which leads to larger activation energy. To evaluate the overall performance of UCF-N3 at different temperature, Figure 15(b) depicts the

measured FoM data and fitting curve based on Equation (13). At room temperature, the FoM of UCF-N3 is $\sim 2.6 \mu\text{m}^2/\text{s}$, and it increases to $4.8 \mu\text{m}^2/\text{s}$ at 50°C .

2.2.3.1.3 Simulation Results for VA LCOS

The electro-optical characteristics of UCF-N3 in a VA-LCOS are calculated using a commercial LCD simulator DIMOS 2.0. In simulation, we used $d=0.93\mu\text{m}$, $\Delta n=0.191$ at $\lambda=550$ nm, and $\gamma_1/K_{33} \sim 6.7 \text{ ms}/\mu\text{m}^2$ at $T=50^\circ\text{C}$. The initial pretilt angle is 88° and the azimuthal angle is 45° w.r.t. the optic axis of the polarizing beam splitter (PBS). A reflector is placed on the inner surface of the VA cell. We calculated the voltage-dependent reflectance (VR) curves for RGB colors. As shown in Figure 16, for the green light, the on-state voltage occurs at 4.83V . The birefringence dispersion is relatively large for high birefringence LCs. As shown in Figure 14(b), $\Delta n=0.214, 0.191, 0.177$ at $\lambda=450\text{nm}, 550\text{nm}$ and 650nm , respectively. The peak transmittance for RGB colors occur at different voltages. Thus, three gamma curves are needed for driving the RGB frames.

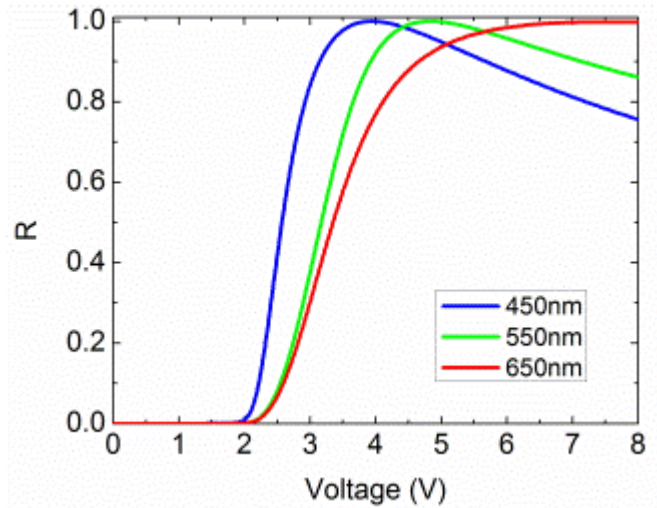


Figure 16. Simulated VR curves for RGB of a VA LCOS using UCF-N3 at 50°C . $d=0.93 \mu\text{m}$

We also calculated the gray-to-gray (GTG) response times of the VA LCOS, and results are summarized in Table 3. Taking green color as an example, the VR curve was uniformly divided into eight gray levels (1-8) and the response time between every two gray levels was calculated. Here both rise time and decay time are calculated between 10% and 90% reflectance change. From Table 3, we find the rise time is 0.26ms and decay time is 0.40ms between gray levels 1 and 8. The average GTG rise time is 0.75 ms and decay time is 0.79 ms. With such a fast response time, image blur and color breakup can be greatly suppressed.

Table 3. Calculated GTG response time (unit: ms) of the UCF-N3 VA LCOS at 50°C. $d=0.93\ \mu\text{m}$.

		Rise Time (ms)							
		1	2	3	4	5	6	7	8
Decay time (ms)	1		2.36	1.75	1.39	1.13	0.91	0.69	0.26
	2	0.34		1.31	1.13	0.95	0.79	0.60	0.22
	3	0.33	1.33		1.02	0.88	0.73	0.56	0.20
	4	0.34	1.19	1.03		0.83	0.69	0.53	0.18
	5	0.34	1.10	1.01	0.91		0.68	0.53	0.17
	6	0.35	1.04	0.98	0.88	0.78		0.53	0.16
	7	0.37	1.01	0.96	0.88	0.79	0.68		0.15
	8	0.40	1.01	0.97	0.90	0.83	0.74	0.63	

The estimated operation temperature range for the proposed color sequential VA-LCOS is from 20°C to 70°C. As the operation temperature decreases, the response time would be slower

because of the increased γ_1/k_{33} . For example, if the application is at room temperature, then from Figure 15(a) the estimated response time would be $\sim 2.3X$ slower than that at 50°C . To shorten response time, overdrive and undershoot voltage method can be applied. On the other hand, if the operation temperature exceeds 70°C , then the birefringence decreases noticeably as Figure 14(a) depicts. As a result, the optical efficiency will decline because the phase retardation is less than 1π .

2.2.3.1.4 UV Stability

As mentioned above, UV stability is an important concern for an arc-lamp-based LCOS projector. UV light could damage the polyimide alignment layers and the LC material⁹². To investigate UV stability, we exposed our UCF-N3 cell (ITO glass substrates) with a UV LED lamp ($\lambda\sim 385\text{nm}$ and light intensity $\sim 300\text{mW/cm}^2$) for five hours. After UV exposure, UCF-N3 shows no sign of degradation: clearing point, dark state, threshold voltage, and electro-optic properties all remain unchanged within the experimental error.

For a high pressure Mercury arc lamp, the emission spectrum contains some harmful UV components in the 380-400 nm range. Therefore, a UV filter with cutoff wavelength $\sim 420\text{ nm}$ is commonly employed. With such a UV filter, our LC mixture should have an excellent stability. For a typical RGB LED backlight unit, its UV content is negligible.

Our fluorinated high birefringence, low viscosity and negative $\Delta\varepsilon$ LC mixture UCF-N3 enables a VA LCOS to achieve high contrast ratio, low voltage, and submillisecond GTG response time at an elevated temperature. Such a fast response time enables color sequential display using a single monochrome LCD panel. As a result, the optical system is greatly

simplified. Moreover, good UV stability makes this LC mixture practical for projection displays. A thin cell gap (0.93 μm) also helps to suppress fringing field effect. Although making a submicron cell gap is technically challenging, it has been done in ferroelectric LCOS devices.

2.2.3.2 MVA Mode

For wide-view LCD TVs, MVA^{11,93-95} and multi-domain IPS^{83,96} are the two major approaches. In MVA transmissive LCDs, the required $d\Delta n$ is 330nm (at $\lambda=550\text{nm}$) for achieving high transmittance and low driving voltage. The cell gap currently employed is around 3-4 μm . Thus, a low viscosity negative $\Delta\epsilon$ LC with $\Delta n\sim 0.08-0.11$ is required. Many such LC mixtures are commercially available. For a 3- μm cell gap, the response time is about 4-5 ms. As the manufacturing technology continues to advance, a thinner cell gap could be used in the near future for shortening the response time. For example, if the cell gap can be reduced to 2.5 μm , then the required Δn is about 0.13. Our low viscosity UCF-N2 can be considered for MVA LCD TV applications.

If we keep the cell gap unchanged, but just using our UCF-N2 in a 3.07- μm cell gap, the on-state voltage would be reduced, as shown in Figure 17. For UCF-N2, $V_{on}=5.6\text{V}$. If we use MLC 6882 and keep $d\Delta n=330$ nm at $\lambda=550$ nm ($d=3.37$ μm), then $V_{on}=7.6\text{V}$.

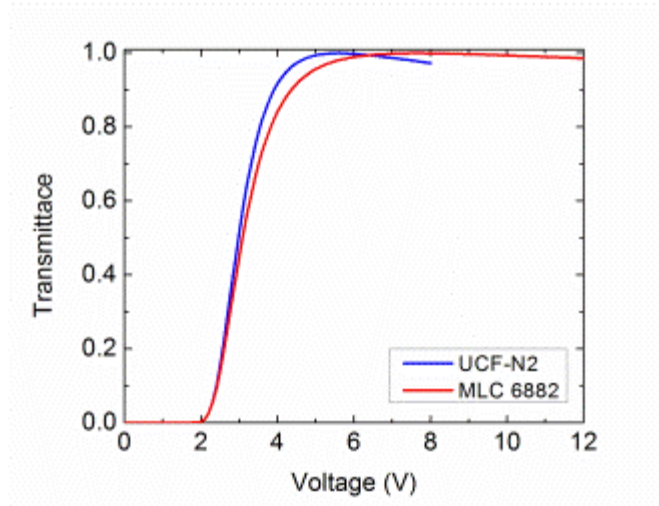


Figure 17. VT curves for VA cell with UCF-N2 ($d=3.07 \mu\text{m}$) and MLC 6882 ($d=3.37 \mu\text{m}$), respectively.

We have discussed on the negative $\Delta\epsilon$ LCs development for FFS and VA display applications. With our UCF-N2, n-FFS shows superior performance such as high transmittance, single gamma curve, cell gap insensitivity, and negligible flexoelectric effect, comparable response time and driving voltage, to the presently employed p-FFS. Using our UCF-N3 for VA LCOS, we have demonstrated a submillisecond gray-to-gray response time for color sequential projection displays. Our low viscosity UCF-N2 can also be used for MVA LCD TVs if the cell gap can be reduced to $2.5\mu\text{m}$. As compared to the $3\text{-}\mu\text{m}$ cell gap currently employed, the response time can be reduced by $\sim 40\%$.

CHAPTER THREE: POLYMER-STABILIZED BLUE PHASE LIQUID CRYSTALS

3.1 Background and Current Progress

Blue phases (BPs)^{97,98} exist between chiral nematic and isotropic phases. When the first such compound was discovered, it happened to appear blue color because of Bragg reflection. Therefore, it was termed blue phase liquid crystal (BPLC) since. For many applications, such as transmissive displays, the Bragg reflection is shifted to UV region so that such a BPLC is actually transparent in the visible region. With nano-structured double twist cylinders and self-assembled three dimensional cubic lattice structures, blue phases are of interest in fast electro-optic components, tunable photonic crystals,⁹⁹ and three dimensional lasers.¹⁰⁰ However, the narrow temperature range due to the frustration between the double twist cylinders limits the application. In 1993, Kitzerow et al. formed blue phases of polymeric liquid crystal monomers and polymerized these monomers while maintaining blue phase structure, leading to a solid resin of fixed blue-phase structure.¹⁰¹ Although this system maintains blue-phase structure, the liquid crystal cannot be dynamically switched because all the constituent molecules were polymerized. In 2002, Kikuchi et al. successfully extended the BP temperature range to over 60 °C including room temperature through polymer stabilization process.¹⁶ By refilling the blue phase templated polymer network with achiral nematic liquid crystal, Coles et al. demonstrated a thermally stable blue phase from -125 to 125 °C.¹⁰² Polymer-stabilized blue-phase liquid crystal (PS-BPLC)¹⁶⁻²⁰ opens a gateway for next-generation display and photonics applications.²⁴ With self-assembled microscopic structure, PS-BPLC exhibits three distinctive features: 1) self-assembly process so

that no surfactant (e.g., polyimide layer) is needed to generate uniform molecular alignment, 2) nanoscale (~100 nm) double-twist cylinder diameter and short coherence length which leads to microsecond response time,^{22,23} and 3) three-dimensional lattice structure resulting in optically isotropic voltage-off state, provided that Bragg reflection is in the UV region. Therefore, BPLC holds promises for fast-response transmissive display,^{19,20,103} reflective display,¹⁰⁴ and photonics applications.²⁵⁻²⁷

PS-BPLC has many attractive features, however high operation voltage, noticeable hysteresis, and large capacitance still hinder its widespread applications. Among these three technical barriers, high voltage is the root cause. If the voltage is low (<10V), then the electrostriction effect, which causes lattice distortion would be suppressed, hysteresis would be negligible (<1%), and moreover high frame rate (>180Hz) can be achieved by the bootstrapping circuits.¹⁰⁵

Therefore, the most fundamental issue for BPLC studies is to lower the operation voltage to below 10V, without sacrificing other desirable properties, such as high transmittance, submillisecond response time, high contrast ratio, and wide viewing angle. To achieve this goal, both device structures and BPLC materials have been investigated extensively. From device structure viewpoint, two major approaches have been developed: 1) implementing protrusion electrodes so that the fringing field can penetrate deeply into the LC bulk,¹⁰⁶⁻¹⁰⁸ and 2) vertical field switching (VFS)¹⁰⁹ to generate uniform longitudinal field across the BPLC layer. From material aspect, developing BPLC materials with a large Kerr constant (K)¹¹⁰⁻¹¹² helps reduce driving voltage because the on-state voltage is inversely proportional to \sqrt{K} .¹⁰⁶ From Gerber's

model, Kerr constant is governed by the birefringence (Δn), dielectric anisotropy ($\Delta\epsilon$), average elastic constant (k), and pitch length (p) of the chiral LC host as:¹¹³

$$K \approx \Delta n \cdot \Delta\epsilon \frac{\epsilon_o P^2}{k\lambda(2\pi)^2}. \quad (18)$$

Fast response time is probably the most attractive feature for PS-BPLC. The relaxation time of a BPLC is determined by rotational viscosity (γ_1), elastic constant and pitch length as:¹¹³

$$\tau \approx \frac{\gamma_1 P^2}{k(2\pi)^2}. \quad (19)$$

It is known that the BPLC response time in the low field region where lattice distortion does not occur is primarily governed by the viscosity, average elastic constant, and pitch length.^{23,113} Polymer structure and polymer concentration also play important roles.

All the properties are closely related to the PS-BPLC materials. We will discuss the material system of PS-BPLC and the contribution of each component to the physical properties in the following section.

3.2 PS-BPLC Material System

A PS-BPLC precursor typically comprises of 70-90wt% of nematic LC host as switching molecules, 5-10wt% of chiral dopant to induce blue phase, and 8-15wt% of photo-curable monomers and ~1% of photo initiator for polymer stabilization. Figure 18 shows the chemical structures of some nematic LC compounds, chiral dopants, and monomers.^{114,115} The properties and influence of each component on the PS-BPLC will be described in details later. To form BPLC composite, the precursor is cooled from

isotropic phase to blue phase, and then exposed to UV light. After UV irradiation, polymer-stabilized BPLC nano-composites are self-assembled, exhibiting the characteristic small platelet structures.

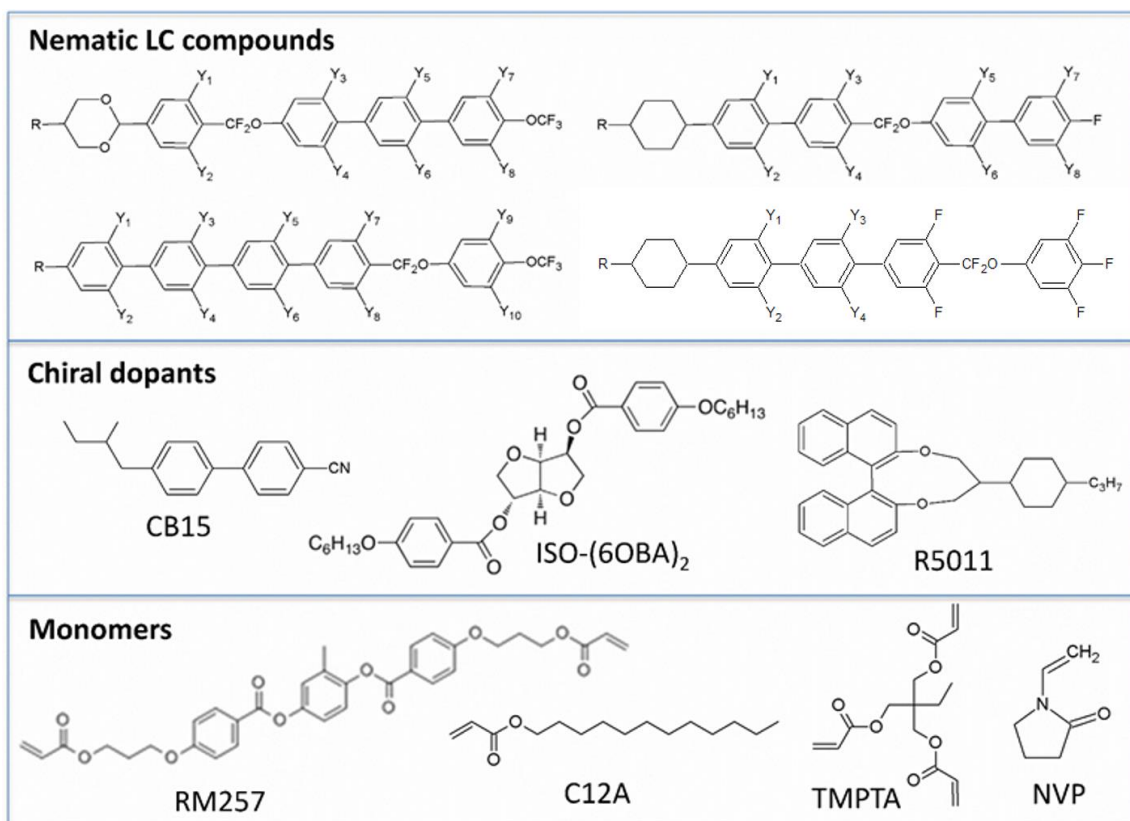


Figure 18. Chemical structures of some exemplary nematic LC hosts, chiral dopants, and monomers used in polymer-stabilized BPLC systems.²¹

3.2.1 Nematic Liquid Crystal Host

A PS-BPLC typically consists of 70-90% nematic liquid crystal host. As a major component, the properties of the LC host would significantly affect the properties of the PS-BPLC, e.g., Kerr constant and response time. Choi et al. has experimentally demonstrated that Kerr constant is

proportional to $\Delta n \Delta \varepsilon k_{33}/k_{11}$ of the nematic LC host.¹⁸ Besides, the viscosity and relaxation frequency of nematic LC host also significantly affect the performance of a PS-BPLC.

3.2.1.1 Birefringence

From Equation (18), a straightforward approach to increase Kerr constant is to boost $\Delta n \cdot \Delta \varepsilon$ because k of the LC host is more difficult to control.¹⁸ The birefringence can be increased by elongating the liquid crystal molecular conjugation length. But the photo-stability and solubility of high birefringence LCs should be taken into consideration. Considering the material stability, melting temperature, and viscosity, terphenyl derivatives could be the longest conjugation for BPLCs. For a stable material, the birefringence is usually smaller than 0.28. It's challenging to get large K through increasing Δn alone. On the other hand, since Δn is wavelength dependent, λK also follows the same dispersion trend as its nematic host LC, and can be described well by the single-band birefringence dispersion model, as reported by Jiao, et al.¹¹⁶

3.2.1.2 Dielectric anisotropy

Increasing $\Delta \varepsilon$ is an effective approach to improve Kerr constant. Indeed, LC hosts with $\Delta \varepsilon$ (>90) have been developed by JNC¹¹⁰ and by Merck¹¹¹ independently. Figure 18 depicts some examples for large $\Delta \varepsilon$ LC compounds.¹¹⁴ Such a large $\Delta \varepsilon$ LC would require several polar groups so that its rotational viscosity and response time would increase dramatically. Indeed, the response time of JC-BP01M is about 2 ms at room temperature (RT~22°C) using an in-plane-switching (IPS) cell.¹¹⁰ In addition, the hysteresis is about 6% because of the strong peak electric field near the IPS electrode edges. A delicate balance between operating voltage, response time, hysteresis, and relaxation frequency has to be taken into consideration.

Recently, we demonstrated a low voltage, submillisecond response time, and hysteresis-free PS-BPLC employing a very large $\Delta\varepsilon$ (~470) LC host JC-BP06N (by JNC) whose clearing point is $T_c=73.8^\circ\text{C}$.¹¹² The rotational viscosity of JC-BP06N is over 1470mPa.s due to the huge $\Delta\varepsilon$.

3.2.1.3 Viscosity

With such a large $\Delta\varepsilon$, the rotational viscosity of the nematic LC for PS-BPLC would be inevitably high due to the addition of several polar groups. For example, at room temperature the rotational viscosity of JC-BP06N is over 1470 mPas, which is about 7X higher than that of Merck E7 ($\gamma_1\sim 200$ mPas). Fast response time is one of the major attractions of PS-BPLC devices. However, if the BPLC is too viscous the response time could be relatively slow (~2 ms), according to Equation (19). Diluters have been widely used for lowering the viscosity and melting temperature of a nematic LC. The diluter effects have also been investigated on polymer-stabilized BPLC.¹¹⁷ The details will be described in Session 3.3.3. A small amount of diluter slightly decreases the birefringence and dielectric anisotropy, but it dramatically reduces the viscosity of the LC host. For example, by doping 6% of 5CC3 [4-pentyl-4'-propyl-1,1'-bi(cyclohexyl)] into a viscous LC host (HTG-135200, HCCH), the rotational viscosity γ_1 is reduced by 200% at 25 °C, Δn by 6%, and $\Delta\varepsilon$ by 10%. The decay time of the resultant PS-BPLC could be reduced by 2X–3X while keeping the Kerr constant unchanged. The decay time was measured between 90% and 10% transmittance change at 25 °C. The measured decay time of PSBP without diluter is 1700 μs . After adding a diluter, the decay time is reduced by 2X-3X.

3.2.1.4 Relaxation Frequency

Since the relaxation frequency f_r is proportional to $1/(\eta l^3)$,¹¹⁸ a large $\Delta\varepsilon$ LC would lead to a fairly low relaxation frequency; e.g., JNC JC-BP01M has a relaxation frequency of 1.3 kHz, and its Kerr constant decreases by $\sim 2X$ as the frequency increases from 60 Hz to 1 kHz.¹¹⁹ When driving this BPLC at 1 kHz for color sequential displays, two serious problems are encountered: 1) the operation voltage is increased by $\sim 40\%$, and 2) the dielectric heating effect¹²⁰⁻¹²² due to the imaginary part (absorption) of dielectric constant, which has a peak value at the relaxation frequency, will affect the performance stability of the BPLC device. An effective diluter would help to dramatically reduce the viscosity and increase the relaxation frequency.

3.2.2 Chiral Dopants

Chiral dopants are essential to introduce high chirality to the nematic LC host and induce blue phases. The pitch length p is inversely proportional to the HTP (helical twisting power, which could vary slightly depending on the nematic LC host) and concentration (c) of the chiral dopant as $p=1/(HTP*c)$. Thus we can tune the pitch length and hence Bragg reflection wavelength by choosing different chiral dopants or varying the concentration of the chiral dopant. If a chiral dopant has a weaker HTP, then its concentration should be increased, leading to some disadvantages: a) The corresponding ratio of nematic LC host (switching molecules) would be lower, which could result in a smaller Kerr constant; b) Most chiral dopants do not have mesogenic phase, therefore adding more chiral dopant would decrease the clearing point of the BPLC; 3) The solubility of the chiral dopant is usually limited: a too high concentration might cause saturation in pitch length or even precipitation. As a result, the stability of the PS-BPLC

will be affected. The *HTP* value of some commercial chiral dopants is relatively low, i.e. *HTP*~8/ μm for CB15. While for BPLC, a high *HTP* chiral dopant, such as R5011 (*HTP*> 100/ μm , whose structure is shown in Fig. 3) has been commonly employed.¹¹⁵

For transmissive displays, the Bragg reflection of blue phases is shifted into UV region (<380nm) in order to obtain an optically isotropic state in the visible region. A shorter Bragg reflection wavelength helps to improve the CR.²³ However, blue phase is not perfectly optically isotropic but with a tiny optical rotatory power.¹²³ Based on this property, approaches have been proposed to compensate the light leakage and thereby improve the contrast ratio and widen the viewing angle of a BPLC display.¹²⁴

As shown in Equation (18), the Kerr constant is proportional to the square of pitch length. Kikuchi and coworkers^{125,126} experimentally demonstrated that the Kerr constant increases significantly with the increased pitch length. By shifting the Bragg reflection from 350 nm to 600 nm, the Kerr constant was improved and the on-state voltage reduced by 35%, as reported by Yan, et al.¹⁰⁴ In principle, we can even shift the Bragg reflection to near infrared region. However, some problems associated with this long-pitch approach are found: 1) In order to retain high contrast ratio, two circular polarizers have to be employed. A circular polarizer is usually comprised of a linear polarizer and a quarter-wave plate so that its cost is more expensive. 2) The long-pitch BPLC leads to slower response time as Gerber's model predicts. 3) A longer pitch length implies to a lower chirality and blue phases may no longer exist. 4) Higher order Bragg reflection could appear in the visible region, which would degrade the contrast ratio.

The Bragg reflection wavelength can be intentionally tuned to a visible wavelength for reflective display^{104,127} or laser applications.¹²⁸

The handedness of the chiral dopant also plays an interesting role on the physical properties of PS-BPLC. Chen et al investigated the polarization ellipse of the reflected light for both RCP and LP incident lights for an electric field-induced monodomain BPLC.¹²⁷ With a right-handed chiral dopant, the reflected light has right-handed circular polarization for both RCP and LP incident beams. The details will be discussed in Section 3.4.3.

3.2.3 *Polymer Network*

As shown in Figure 19, BPLC has double twist cylinder (DTC) structures and these cylinders further form periodic lattice. When these DTCs are in contact, there are disclination lines. Blue phases must coexist with disclinations for topological reasons, which maintains the balance of BP thermodynamically.¹²⁹ Due to the defect lines, BP only exists in a narrow temperature range. Polymer networks play a key role in the PSBP system as they concentrate on the disclination core in a random coil conformation in the lattice structures and stabilize the blue phases.¹⁶ Certain amount of monomers is needed to expand the temperature range. Typically, a diacrylate monomer (e.g. RM257) and a mono-functional monomer (C12A) or tri-functional monomer (TMPTA) are jointly employed to stabilize a blue phase. The chemical structures for these monomers are shown in Figure 18. After polymerization, the miscibility of the polymer chains with liquid crystal molecules cannot be too high, otherwise, the polymer would be homogeneously dispersed in the liquid crystal and there is no stabilization effect.¹⁶ With

Confocal Laser Scanning Microscope, Kikuchi et al. have directly observed the periodic pattern images of PS-BPLC, due to (110), (100), (111), and (211) planes of bcc lattice in BPI.⁵⁹

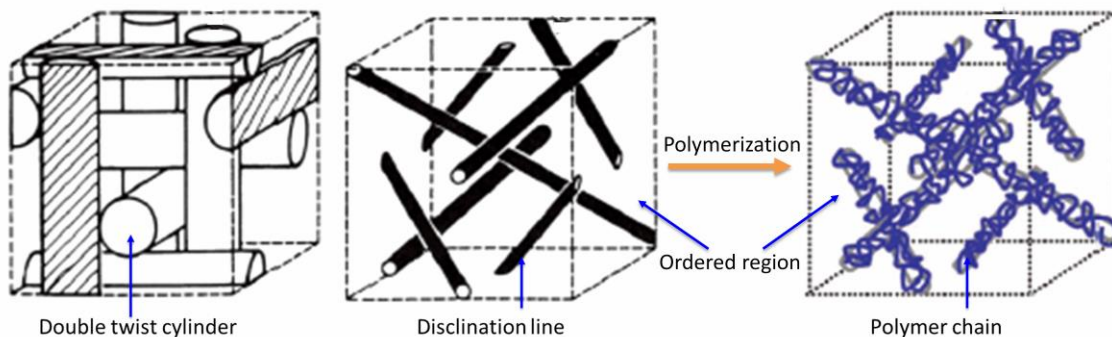


Figure 19. Illustration of the mechanism for polymer stabilization effect on blue phase

Besides temperature stability, polymer network also influences the electro-optic properties. Increasing monomer concentration in a certain range leads to higher operating voltage, smaller hysteresis, lower residual birefringence, and faster response time.^{130,131} The copolymerization reactivity ratio of two different monomers, and types of monomers would also change the formation of the polymer network. We have achieved record fast response time - microsecond by employing more rigid polymer network. The details will be described in Session 3.4.1.

By doping a low molecular weight monomer (N-vinylpyrrolidone, NVP)¹³² into a conventional BPLC system (with RM257 and TMPTA), Zhu et al¹³² found that the resultant Kerr constant is increased by 54% while response time shortened by 23%. A reactive diluent can be formed by NVP and acrylic functional groups of the RM257 and TMPTA after polymerization. It can degrade the strength of polymer network and reduce the interfacial energy at the interface between the polymer network and DTCs that increase the Kerr constant. Meanwhile, it helps to

reduce the effective rotational viscosity of the material system resulting in faster response time of PS-BPLC.

Besides the monomer composition and concentration, the polymerization conditions also affect the formation of the polymer network, such as curing temperature, exposure wavelength and intensity of UV light and so on.^{133,134} In order to better understand and elaborate the mechanism of polymer network formation under different conditions and the effects on the corresponding electro-optic properties of PS-BPLC, further experimental investigations are necessary.

3.3 Properties of PS-BPLC

3.3.1 *Blue Phase Appearance*

Generally speaking, blue phases appear in a highly twisted chiral nematic liquid crystal.¹³⁵ Depending on the structure, there are up to three blue phases: BPI, BPII and BPIII. BPI shows body-centered cubic structure, BPII has simple cubic structure while BPIII exhibits the same symmetry as isotropic phase.¹³⁵ The local refractive index variation in the blue phase structure results in selective Bragg reflections. However, blue phases are not necessarily blue. The reflection wavelength is governed by the lattice structure as:¹²⁹

$$\lambda_B = \frac{2na}{\sqrt{h^2 + k^2 + l^2}}, \quad (20)$$

where h , k , and l are the Miller indices of a crystal plane, n and a denote average refractive index and lattice constant of blue phases. The lattice constant is related to the pitch length p . For BPI, $a=p$, while for BPII $a=p/2$.¹²⁹ As the pitch length decreases, the reflected color shifts from red, green to blue. When blue phase grows from isotropic phase without any electric field, multiple

diffraction peaks can be observed from (110), (200) and (211) directions (with these lattice surfaces parallel to the substrate) of BPI.¹²⁹ This forms the characteristic platelet texture of blue phase, as shown in Figure 20(a), (c), and (e).¹²⁷

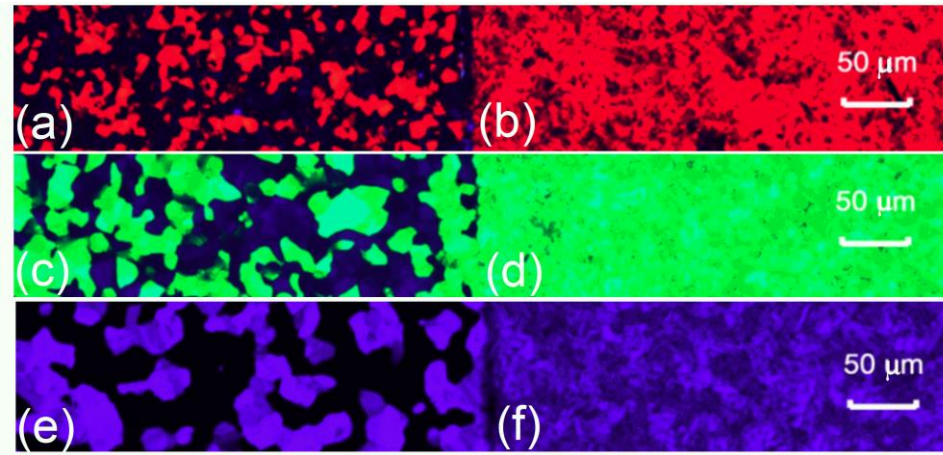


Figure 20. (a),(c),(e) Typical multi-domain blue phase platelet texture (b),(d),(e) monodomain blue phase texture with different pitch length. Reflective images.

3.3.2 Electric Field Effect

Blue phase liquid crystal molecules are anisotropic and dynamically switchable by electric field (E), which attracts tremendous attention. There are different electric field effects on blue phases, such as lattice orientation effect, Kerr effect, lattice distortion, phase transition and so on.^{113,136,137} When the multi-domain BP lattice is subject to a uniform electric field, the nonzero torque exerted on the blue phase lattice will rotate the lattice to the nearest stable position where the torque vanishes.¹³⁶ Thus, the electric field-induced monodomain blue phase with single Bragg reflection peak is created, as shown in Figure 20(b), (d), and (f).¹²⁷ Blue phase texture could be changed and narrow band reflection color is generated. It's worth to mention that

surface alignment¹⁰⁴ and surface free energy engineering¹³⁸ have also been demonstrated to induce monodomain blue phases.

Besides the lattice reorientation effect, blue phase liquid crystal is optically isotropic at a wavelength considerably longer than the Bragg reflection and can be treated as a Kerr media. When an electric field is applied, liquid crystal molecules tend to align with the electric field if the dielectric anisotropy $\Delta\varepsilon > 0$ (or perpendicular to the electric field if $\Delta\varepsilon < 0$). As a result, birefringence is induced. In the low field region, the induced birefringence can be described by Kerr effect as:

$$\Delta n_{ind} = \lambda K E^2, \quad (21)$$

where λ is the wavelength, E is the electric field and K is the Kerr constant. Typically K is positive since positive $\Delta\varepsilon$ LCs are usually employed. However, with negative $\Delta\varepsilon$ LCs, PS-BPLC with a negative Kerr constant has also been reported,¹³⁹ although its Kerr constant is relatively small because of the relatively small $|\Delta\varepsilon|$ (<10) of the negative LC host.

To better describe the saturation phenomenon of the induced birefringence, Yan et al. proposed the extended Kerr effect:¹⁴⁰

$$\Delta n_{ind} = \Delta n_s (1 - \exp[-(E / E_s)^2]), \quad (22)$$

where Δn_{sat} is saturation birefringence and E_s is the saturation electric field. Kerr effect exhibits a fast response time (<1 ms) because of the short coherent length of BPLC. However, a higher electric field could lead to lattice distortion and hence Bragg reflection wavelength shift.¹²⁹ The relaxation time of lattice distortion is in the order of 10-100 ms. Under a sufficiently high electric field, blue phase may transform to new phases, to chiral nematic phases, and ultimately to

nematic phases.^{137,141} This transition is usually very slow (a few seconds or even longer), which causes undesirable hysteresis or residual birefringence. In the case of PS-BPLC, local reorientation (Kerr effect) mostly occurs upon application of the electric field, since the lattice structure is restricted by the polymer network.¹⁷ The Bragg reflection color change under electric field should be very minor.^{16,127}

3.3.3 Diluter Effects on PS-BPLC

From Equation (18), increasing $\Delta\varepsilon$ is a straightforward way for enhancing Kerr constant. Indeed, BPLC hosts with $\Delta\varepsilon > 100$ have been developed recently.¹¹⁰⁻¹¹² For comparison, a typical nematic LC has $\Delta\varepsilon < 10$. Therefore, BPLC represents a paradigm shift in LC material development. The problems associated with such a huge $\Delta\varepsilon$ LC are threefold: 1) its viscosity is large, so that the device response time goes back to 1-ms range and the one-drop fill panel fabrication process becomes more difficult; 2) the pixel's capacitance is increased by $\sim 10X$, so that a longer circuit charging time is needed;¹⁰⁵ 3) lower relaxation frequency; e.g., JNC JC-BP01M has a relaxation frequency of 1.3 kHz, and its Kerr constant decreases by $\sim 2X$ as the frequency increases from 60 Hz to 1 kHz.¹¹⁹ When driving this BPLC at 1 kHz for color sequential displays, two serious problems are encountered: 1) the operation voltage is increased by $\sim 40\%$, and 2) the dielectric heating effect¹²⁰⁻¹²² due to the imaginary part (absorption) of dielectric constant, which has a peak value at the relaxation frequency, will affect the performance stability of the BPLC device.

Diluters have been widely used for lowering the viscosity and melting temperature of a nematic LC.¹⁴²⁻¹⁴⁸ However, diluter effect on the BPLC properties has not been investigated.

Here, we report the diluter effects on a BPLC host which has a large $\Delta\varepsilon$. When we dope 6 wt% of a diluter to the LC host, the mixture's viscosity (η) is dramatically reduced, while the decrease in Δn and $\Delta\varepsilon$ is mild. Most diluter molecules are fairly short, while the large $\Delta\varepsilon$ BPLCs have bulky and long molecules with several dipole groups. Thus, after the addition of diluters the average molecular length l is shortened. Since the relaxation frequency f_r is proportional to $1/(\eta l^3)$,¹¹⁸ diluters help to increase f_r . This increased relaxation frequency is less critical to nematic LCs because their relaxation frequency is already high (>50 kHz), but is important to BPLCs because their relaxation frequency is usually low (<10 kHz).

In this session, several diluters, including compounds and mixtures, were employed. Doping 6% of some diluters not only reduces the response time by 2X–3X but also improves the Kerr constant. To compare the performance with and without diluters, we use a Figure of Merit for BPLC (FOM_{BP}) defined as the ratio of Kerr constant to decay time (K/τ).¹⁴⁹ Higher diluter concentration helps to further decrease the response time, but its tradeoff is the decreased Kerr constant.

3.3.3.1 LC Host Properties

In experiment, we used LC1 (HTG-135200, HCCH, China) as the nematic host. Its physical properties are listed as follows: $\Delta n=0.205$ at $\lambda=633$ nm, $\Delta\varepsilon=99$ at 1 kHz, $\gamma_1=700$ mPas at 25 °C, and clearing temperature $T_c=98$ °C. We mixed 94 wt% of LC1 with 6% of a nonpolar diluter 5CC3 [4-pentyl-4'-propyl-1,1'-bi(cyclohexyl)]. For convenience, we call this mixture as LC2.

Both Δn , $\Delta\varepsilon$, viscoelastic constant (γ_1/k_{11}) and γ_1 of the LC mixture are all temperature dependent, as described by Equation (8), (10), (12) and the following equations:^{29,54,56,57,149,150}

$$\Delta\varepsilon = aS \exp(U / k_B T), \quad (23)$$

where U is a parameter related to dipole moment, and a is proportionality constants. After doping 6% of 5CC3, the T_c of LC2 drops slightly from 98 °C to 96 °C.

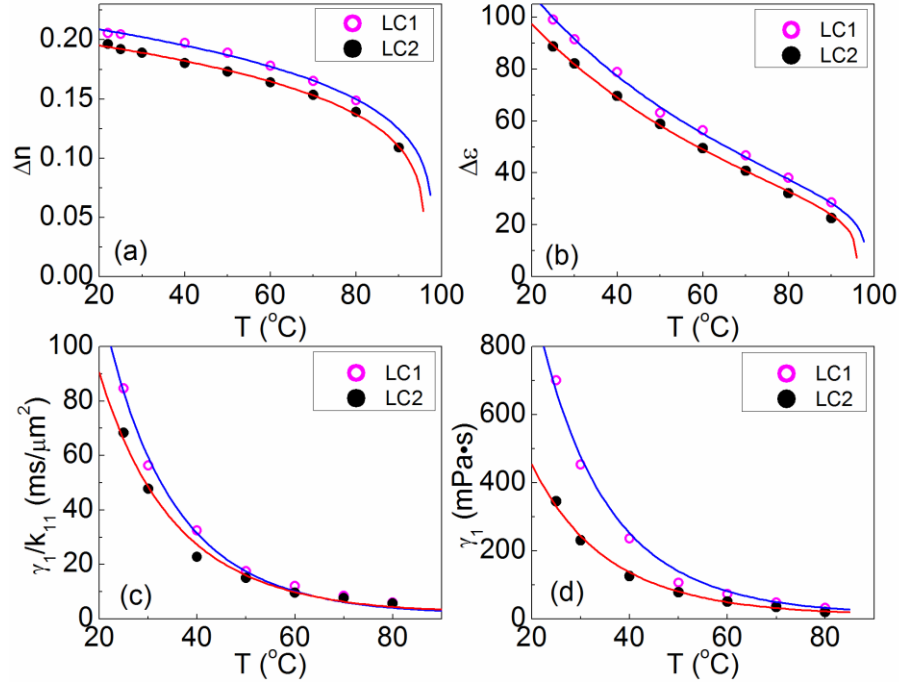


Figure 21. Temperature dependent (a) Δn at $\lambda=633$ nm, (b) $\Delta\varepsilon$ at 1 kHz, (c) γ_1/k_{11} and (d) γ_1 of LC1 and LC2. Dots represent the measured data and lines are fitting results by Equation (8), (10), (12) and (23), respectively.

Figure 21 depicts the temperature dependent Δn (at $\lambda=633$ nm), $\Delta\varepsilon$ (at 1 kHz), γ_1/k_{11} and γ_1 of LC1 and LC2. Please note that these are the LC hosts without chiral dopants and photo-curable monomers. Here, dots are experimental data and lines are fitting results with Equation (8), (10), (12) and (23). Table 4 lists the fitting parameters. The agreement is quite good. After doping 6% 5CC3 to LC1, the Δn of LC2 is decreased by about 6%, $\Delta\varepsilon$ by 10%, and more amazingly the rotational viscosity γ_1 is reduced by 200% at 25°C (Figure 21(d)). However, doping a low molecular weight diluter also lowers the elastic constant. As a result, γ_1/k_{11} is only reduced by

20% (Figure 21(c)). From Table 4, the activation energy E_a of LC2 is about 10% smaller than that of LC1 because of the lower viscosity induced by the diluter.

Table 4. Fitting parameters for LC1 and LC2 .

LC Host	Δn_0	β	U (meV)	a	E_a (meV)	A	c
LC1	0.297	0.226	109	2.07	550	2.9E-8	2.3E-7
LC2	0.279	0.227	109	1.87	501	1.5E-7	7.7E-7

3.3.3.2 Relaxation Frequency

For color sequential displays, a higher operation frequency (up to 1 kHz) is needed in order to suppress color breakup. In a BPLC, the relaxation frequency of Kerr constant is closely related to the dielectric relaxation frequency f_r of the LC host.¹¹⁹ For a low- viscosity nematic LC host, its f_r is usually over 50 kHz. For a BPLC host with a large $\Delta\epsilon$, the molecules tend to be long and bulky because multiple dipole groups are employed. Therefore, its dielectric relaxation frequency is reduced significantly. For a positive $\Delta\epsilon$ LC material, ϵ_{\perp} remains almost unchanged in the low frequency region due to its much higher f_r compared to ϵ'_{\parallel} (real part of the permittivity).¹⁵¹ The relaxation of $\Delta\epsilon$ basically follows that of ϵ'_{\parallel} . The frequency dependent ϵ'_{\parallel} was obtained by measuring the capacitance of a homeotropic LC cell (results are not shown here) and fitting the experimental data with Debye relaxation equation:^{152,153}

$$\epsilon'_{\parallel} = \epsilon_{\infty} + \frac{\epsilon_0 - \epsilon_{\infty}}{1 + (f / f_r)^2}, \quad (24)$$

where ϵ_0 is the static permittivity along the long molecular axis at low frequency, and ϵ_{∞} is the permittivity at the high frequency limit. The measured f_r at 25°C for LC1 and LC2 is 12.6 kHz and 15.4 kHz, respectively. When we dope 6wt% 5CP3 (structure shown in Table 5) into LC1, f_r

increases to 17.2 kHz. Diluters help to increase the relaxation frequency of the LC host due to the reduced viscosity and shortened average molecular length. This is particularly favorable for high frequency operation of the LC host and PS-BPLC. This effect becomes more critical for the LCs with low relaxation frequency, say $f_r \sim 1$ kHz. Let us illustrate this principle using following example.

As shown in Figure 22, the LC host has a very large $\epsilon'_{//}$ (190; black solid line) at 100 Hz, but it declines sharply as the frequency increases. At $f_r=500$ Hz, $\epsilon'_{//}$ drops by 2X, and at 1 kHz it further decreases to 40. By adding a diluter, the relaxation frequency shifts rightward to 2 kHz (red solid line). Although at 100 Hz, its real part is decreased from 190 to 160, at 1 kHz (the intended operation frequency for color sequential displays) its $\epsilon'_{//}$ remains as large as 130 (c.f., 40 for the host without diluter). Meanwhile, the dielectric absorption (imaginary part $\epsilon''_{//}$) peak also shifts to a higher frequency (red dashed lines), which helps to reduce dielectric heating effect.

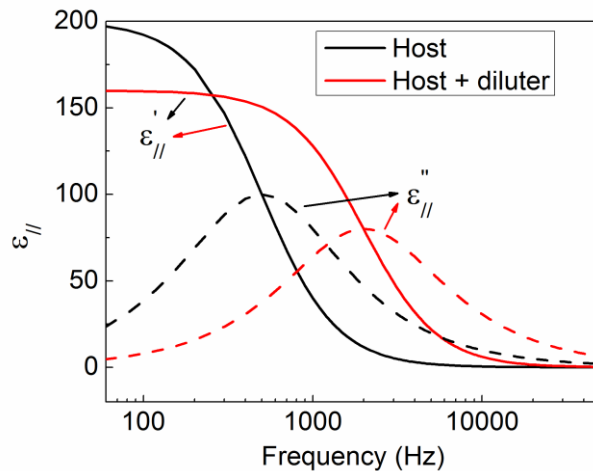


Figure 22. Illustration of relaxation frequency shifting by doping a low viscosity diluter to a LC host.

Moreover, the relaxation frequency decreases exponentially with temperature. Thus, low temperature and high frequency operation for large viscosity PS-BPLCs would be limited.¹⁵⁴ Even the temperature is still above the melting point of a blue phase (ultimate limit), the dramatic plunge of $\Delta\epsilon$ results in a tremendously high driving voltage, which makes the device difficult to operate. Again, an effective diluter would help to increase the relaxation frequency and benefit the low temperature operation.¹¹⁷

3.3.3.3 Diluter effects on PS-BPLC

To investigate the diluter effect on a PS-BPLC without affecting its pitch length and monomer concentration, we keep the ratio of LC host to chiral dopant/monomer the same for the 12 PSBP samples studied. In Table 5, the eleven LC hosts (LC2-12) all consist of 94wt% of LC1 and 6wt% of different diluters. We prepared BPLC mixtures with 4.5wt% chiral dopant R5011 (HCCH) and 95.5wt% LC host. Afterwards, 8 wt% of photocurable monomers [4.8 wt% RM257 (Merck) + 3.2 wt% C12A, Sigma Aldrich] and 0.5 wt% of photoinitiator were blended with 91.5 wt% of the BPLC mixture to form the precursor. Next, we injected the LC/monomers mixture into an in-plane-switching (IPS) cell in an isotropic phase. The IPS electrode width and gap are 10 μm and the cell gap is $\sim 7.3 \mu\text{m}$. The cell was placed on a heating/freezing stage and cooled to BP phase and then exposed to UV light ($\lambda=365 \text{ nm}$) with intensity of 8 mW/cm^2 for 10 min. After UV irradiation, the BPLC nano-composites were self-assembled and the blue phase to isotropic phase transition temperature (T_{c_BP}) for PSBP-1 was $82.3 \text{ }^\circ\text{C}$. With diluters, the T_{c_BP} is few degrees lower, as listed in Table 5, because of the relatively low clearing point of the diluter itself. The impact of $1\text{-}2^\circ\text{C}$ decrease in T_{c_BP} with some diluters is not significant. On the other hand, the chiral nematic to blue phase transition temperature (T_{m_BP}) could be lowered by adding

a proper diluter, which helps to increase the low temperature stability. For PSBP-11, although 6% of FPPF lowers the T_{c_BP} by 10 °C, the T_{m_BP} is also lowered from 5.6 °C to -13 °C, which is favorable for low temperature operation. The color of these PSPB samples looks almost the same, indicating the pitch length variation after adding diluter is negligible.

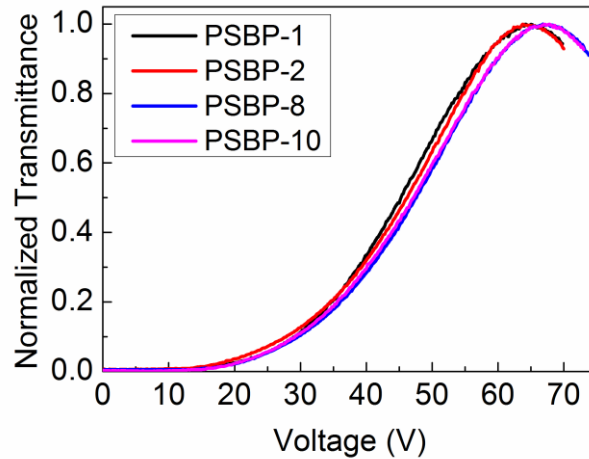
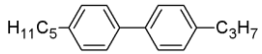
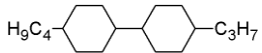
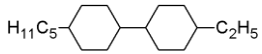
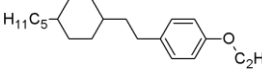
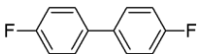


Figure 23. Measured VT cures for PSBP-1, 2, 8 and 10. $\lambda=633$ nm.

Table 5. Physical properties of PSBP samples containing 6% of different diluters. Here, Kerr constant and decay time were measured at $\lambda=633$ nm, and 25°C. (*The FoM_{BP} is normalized to that of PSBP-1).

PSBP #	LC host	Diluter type	Diluter Structure	K (nm/V ²)	Decay time (τ , μ s)	FoM_{BP}	T_{m_BP} (°C)	T_{c_BP} (°C)
1	LC1	No diluter		8.27	1700	1	5.6	82.3
2	LC2	5CC3	<chem>CCCCCCCC1CCCCC1C2CCCCC2</chem>	8.04	573	2.90	7.9	81
3	LC3	5CP3	<chem>CCCCCCCC1CCCCC1C2=CC=CC=C2</chem>	8.83	740	2.46	-1	75.4
4	LC4	5CCV	<chem>CCCCCCCC1CCCCC1C2=CC=CC=C2C=C</chem>	7.48	1200.8	1.29	-4.5	79.5
5	LC5	5CP02	<chem>CCCCCCCC1CCCCC1C2=CC=C(C=C2)OCC</chem>	9.11	988	1.90	0	81

6	LC6	5PP3		9.44	737.3	2.64	4.5	76
7	LC7	4CC3		7.39	633.4	2.41	3	80.5
8	LC8	5CC2		7.4	678.7	2.25	1	79.3
9	LC9	5CAP02		7.36	738.2	2.06	-1.1	78.2
10	LC10	MLC-6686		7.36	1062.4	1.43	3.5	81.5
11	LC11	FPPF		6.37	638.4	2.06	-13	72.5
12	LC12	5CC3 & 4CC3 at 1:1 ratio		7.44	792	1.94	4.2	81.5

The IPS cell was mounted on the heating stage and sandwiched between two crossed polarizers. A linearly polarized He-Ne laser ($\lambda=633$ nm) was used as probing beam. A 1-kHz square-wave AC signal was applied to the IPS cell. The light transmittance was measured by a photodiode detector. Figure 23 depicts the measured voltage-dependent transmittance (VT) curves for PSBP-1, 2, 8 and 10. The first peak occurs at 61.6V, 62.4V, 66V and 66.6V respectively. Through fitting with extended Kerr model,^{19,140} we obtained the Kerr constant $K=8.27$ nm/V² for sample PSBP-1. After adding 6% of diluters, the Kerr constant of PSBP-2, 8 and 10 decreases to 8.04, 7.40 and 7.36 nm/V², respectively. The variation is within 11%, since the effect of diluter on Δn and $\Delta \epsilon$ is small. On the contrary, the on-state voltage of PSBP-3, 5 and 6 decreases slightly to 61V, 61V and 59.6V. This is a pleasant surprise because the employed diluters are non-polar and low birefringence compounds. We expect they would decrease the mixture's Δn and $\Delta \epsilon$ significantly so that the on-state voltage would increase instead of decrease.

To understand this unexpected phenomenon, we have to examine what factors determine the Kerr constant. From Equation (18), Kerr constant of a BPLC is primarily governed by the ratio of $\Delta n \cdot \Delta \varepsilon / k$ (note here k is the average elastic constant of the PSBP, which is different from the k_{11} of the LC host), provided that the pitch length and wavelength remain the same. As discussed above, after doping a diluter both Δn , $\Delta \varepsilon$, k_{11} and γ_1 decrease but at different rates. Therefore, it is possible for $\Delta n \cdot \Delta \varepsilon / k$ to either increase or decrease, depending on the relative change of Δn , $\Delta \varepsilon$, and k induced by the diluter, which is related to the sophisticated inter-molecular interactions between the elongated, bulky host LC and the short, small-sized diluter molecules.

Fast response time is one of the major attractions of PS-BPLC devices. In experiment, we compared the decay time of those 12 PSBP samples because the rise time depends on the applied voltage, which is more complicated. The decay time was measured between 90% and 10% transmittance change at 25 °C. The measured decay time of PSBP-1 (without diluter) is 1700 μ s. After adding diluters, the decay time is decreased by 2X-3X, as listed in Table 5.

To explain this dramatic change in response time, we refer to Equation (19)¹¹³. Here γ_1 represents the rotational viscosity of PSBP. In our samples with 6wt% diluters, the variation of p is unnoticeable. The average elastic constant k of PS-BPLC becomes more complicated, since it involves the strong anchoring energy provided by the polymer network and also the interaction between LCs and the chiral dopant. When polymer network is involved, the elastic constant could be 1000X larger than that of the LC host.¹⁵⁵ The diluter effect on the elastic constant of the PSBP is not as significant as the polymer network effect. On the other hand, the viscosity tends to increase noticeably after adding the bulky chiral dopant to the LC host for a PS-BPLC. The

small diluter molecules could break the rigid arrangement of the BPLC mixture, which in turn reduces the viscosity effectively and hence the response time.

To eliminate the effect of k , the FoM_{BP} (defined as $K/\tau \propto \Delta n \cdot \Delta \varepsilon / \gamma_l$)¹⁴⁹ of the 12 PSBP samples are calculated for comparing the performance of PS-BPLC materials. To see the difference more clearly, we normalized the FoM_{BP} to that of PSBP-1. From Table II, the FoM_{BP} can be improved by 1.3X-2.9X with different diluters. Specifically, our data show that the γ_l of PSBP-2 is 3.4X lower than that of PSBP-1 (without any diluter). Plugging these values to Equation (18), we find k is ~15% smaller after adding 5CC3, which proves that the dramatic decrease of response time results from the significant decrease in viscosity.

3.3.3.4 Temperature effect

To investigate the activation energy, which is related to the viscosity of the PS-BPLC, we measured the temperature dependent decay time of PSBP-1 and PSBP-2. Results are shown in Figure 24. The decay time decreases as the temperature increases, as described by following equation:¹⁵⁶

$$\tau \approx B \cdot \frac{\exp(E_a / k_B T)}{(1 - T / T_{c_BP})^\beta}, \quad (25)$$

where B is a proportionality constant, E_a is the activation energy of the PSBP, and T_{c_BP} is the clearing point of the PS-BPLC. The material constant β has been obtained from the LC host (listed in Table I). From fittings, we obtained $E_a=738$ meV and $B=4.0 \cdot 10^{-10}$ μ s for PSBP-1, and $E_a=573$ meV, $B=7.8 \cdot 10^{-8}$ μ s for PSBP-2. As expected, PSBP-2 has lower activation energy than PSBP-1, since the diluter in PSBP-2 helps to make the PS-BPLC less viscous. Moreover, PS-

BPLC has a higher activation energy than the nematic LC host, indicating that the added chiral dopant indeed increases the viscosity.

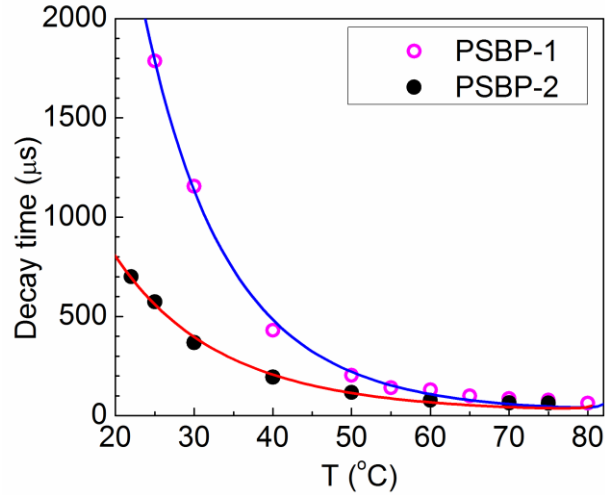


Figure 24. Temperature dependent decay time of PSBP-1 and PSBP-2. Dots are measured data and lines are fitting with Equation (25).

3.3.3.5 Concentration Effect

Higher concentration of diluter helps to further reduce the viscosity, but it could have some side effects, such as poor solubility when the diluter has smectic phase, smaller Kerr constant and reduced T_{c_BP} . We prepared another two PSBP samples with 10wt% and 15wt% of 5CC3. The decay time decreases significantly with more diluters, as listed in Table 6, however the Kerr constant also decreases noticeably. Moreover, T_{m_BP} increases a lot with increased 5CC3 concentration, which is unfavorable for practical applications. Therefore, for a given diluter there exists an optimal concentration. Mixing diluters at a proper ratio is also a common practice for nematic LCs. We could do the same for BPLC in order to increase its solubility.

Table 6. Influence of diluter concentration on the PS-BPLC properties.

5CC3 ratio	K (nm/V²)	Decay time (τ, μs)	FoM_{BP} (K/τ)	$T_{m_{BP}}$ (°C)	$T_{c_{BP}}$ (°C)
0	8.27	1700	1	5.6	82.3
6%	8.04	573	2.90	7.9	81
10%	7.50	516	3.00	10.4	80.7
15%	7.10	383	3.83	22	79.8

3.3.3.6 Conclusion

We have investigated the effects of different diluters on PS-BPLC from various aspects. A small amount of diluter will slightly decrease the birefringence and dielectric anisotropy but dramatically reduce the viscosity of the LC host. By doping 6% of diluter, the decay time of the PS-BPLC could be reduced by 2X–3X while keeping the Kerr constant unchanged. We also studied the diluter effects on the relaxation frequency, melting point and clearing point. By increasing the concentration of a small molecular weight diluter (or a mixture among diluters), the response time of the BPLC can be further decreased, but some undesirable side effects (e.g., smaller Kerr constant) would become noticeable. Therefore, an optimal concentration of diluter should be considered for optimizing the overall performance of the BPLC composite.

3.4 Advanced PS-BPLC Materials and Devices

3.4.1 *A Microsecond Response Time PS-BPLC*

From Equation (19), three approaches can be considered for improving response time: 1) to reduce pitch length by increasing chiral concentration, 2) to increase elastic constant by strengthening polymer network, and 3) to reduce viscosity by operating the cell at an elevated temperature. However, each approach has its pros and cons. In approach (1), reducing pitch

length by increasing chiral concentration could lead to a higher operation voltage [as described in Equation (18)] and lower clearing temperature of the BPLC composite. For example, CB-15 is a chiral compound; its clearing point is $\sim 4^{\circ}\text{C}$. Adding CB-15 to a BPLC mixture would dramatically decrease the clearing temperature. In approach (2), a strong polymer network would reduce response time and suppress hysteresis, but its operating voltage will be inevitably increased. In approach (3), elevated temperature would substantially reduce rotational viscosity, but the tradeoffs are reduced Kerr constant and increased operation voltage. Therefore, a delicate balance between abovementioned parameters should be taken.

In the experiment, we prepared a nematic LC host designated as JM2069-145 (ITRI, Taiwan). It is a multi-component mixture comprising of cyano-biphenyl and terphenyl compounds. Its physical properties are listed as follows: $\Delta n=0.215$ at $\lambda=633$ nm, $\Delta\epsilon=50$ at 1 kHz and 21°C , and clearing temperature $T_c=80^{\circ}\text{C}$. In order to induce chirality into the host nematic LC, we mixed 93 wt% JM2069-145 with 7 wt% of a high helical twisting power (HTP $\approx 100/\mu\text{m}$) chiral compound.¹¹⁵ Blue phase was found from 57°C to 62°C during the heating process. From the chiral concentration and HTP, we estimated that the pitch length is about 140 nm. To compare the influence of the polymer network on the electro-optic properties of PS-BPLC, we prepared two samples with different monomer composition. Sample A is using C12A while Sample B is using TMPTA. For each sample, 10 wt% of monomers [6 wt% RM257 (Merck) + 4 wt% C12A or TMPTA] and 0.8 wt% of photoinitiator were blended with 89.2 wt% of the BP host to form the precursor. Next, we injected the LC/monomers mixtures into vertical field switching (VFS) cells in isotropic phase. The VFS cell was comprised of two ITO (indium tin oxide) glass

substrates, but without polyimide alignment layer. The cell gap was measured to be 5.44 μm (For Sample A) and 5.27 μm (Sample B), respectively. Afterwards the cells were placed on a Linkam heating/freezing stage controlled by a temperature programmer. The cells were cooled to BP phase, and then exposed to UV light ($\lambda=365\text{ nm}$) with intensity of 2 mW/cm^2 for 30 minutes.

After UV irradiation, polymer-stabilized BPLC nano-composites were self-assembled. The Bragg reflection is in the UV range due to the short pitch length. The texture of the BPLC under crossed polarizer is shown in Figure 25(a). We intentionally increased the illumination intensity of the microscope in order to see the small platelet structures of the blue phase.

Figure 25(b) depicts the measurement setup. A linearly polarized He-Ne laser ($\lambda=633\text{ nm}$) was used as probing beam. In order to acquire phase retardation, the laser beam was incident on the VFS cell at an 80° oblique angle. The VFS cell was immersed in a glass container filled with glycerol ($n=1.47$) so that the beam could enter the LC layer at a large angle due to the refractive index match between the glass and glycerol. The container was placed between two crossed polarizers, and the light transmittance was measured.

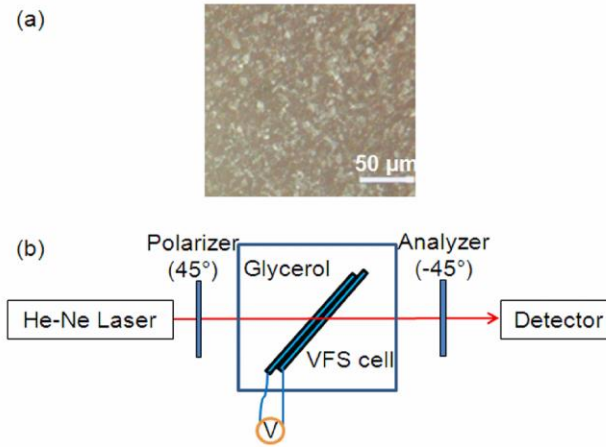


Figure 25. (a) Microscopic image of the PS-BPLC under crossed polarizers, and (b) Experimental setup for electro-optic measurement of the VFS cell.

Figure 26 depicts the measured VT curves, where the dots represent the measured data and the lines are the fitting curves. For Sample B, the first transmission peak occurs at $V_p=44.2$ V, which corresponds to an electric field of 8.39 V/ μm . In the voltage-off state, blue phase is optically isotropic. The contrast ratio is defined as T_p/T_{dark} , where T_p is the peak transmittance at V_p and T_{dark} is the dark state light leakage at $V=0$. Our measured contrast ratio is over 1300:1, indicating that the dark state is pretty good due to the short pitch length of the BPLC. As voltage increases, the induced birefringence increases as described by extended Kerr model.¹⁴⁰ Through fitting,¹⁹ we obtained the Kerr constant $K=\Delta n_s/(\lambda E_s^2)=0.6$ nm/V². By contrast, the on state voltage for Sample A is 35.8 V and the Kerr constant is 0.97 nm/V². Since the pitch length, Δn and $\Delta \epsilon$ are the same for both Samples, we find that the elastic constant of Sample B is 1.6X larger than that of Sample A. The increased elastic constant is believed to originate from the strong polymer

network¹⁵⁵ formed with RM257 and TMPTA which has three functional groups while C12A only has one. A strong polymer network helps to reduce hysteresis and response time.

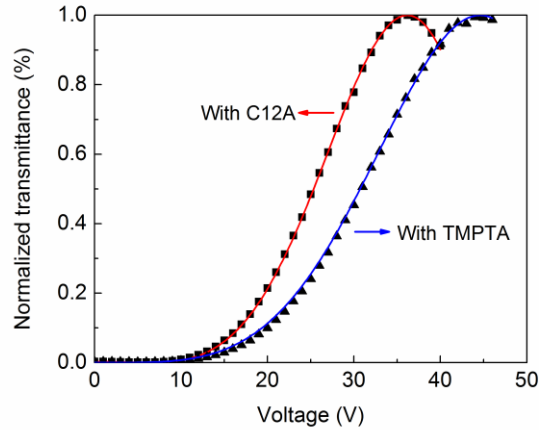


Figure 26. VT curve for cell with TMPTA (blue line) and for cell with C12A (red line).

Hysteresis affects gray scale accuracy of a BPLC device and should be minimized. To measure hysteresis, we drove the VFS cell by ascending the voltage to V_p and then gradually descending it to 0. Hysteresis is defined as $\Delta V/V_p$, where ΔV is the voltage difference between the forward and backward scans at half of the peak transmittance, shown in Figure 27. For Sample B, the measured $\Delta V/V_p$ is only 0.68%. Although the maximum electric field is as strong as 8.39 V/ μm , the hysteresis is still negligible, indicating the polymer network is quite stable.¹⁵⁷ If the cell is driven to 31 V (i.e., 50% of the peak transmittance) and then back to zero (result not shown), hysteresis is too small (<0.1%) to be detected by our measurement system. For Sample A, the hysteresis is free when driving to its peak voltage of 35.8V but increases to 1.8% when driving to 44.2V. This again indicates that the polymer network with TMPTA is stronger than that with C12A. The comparison between Sample A and B is listed in

Table 7.

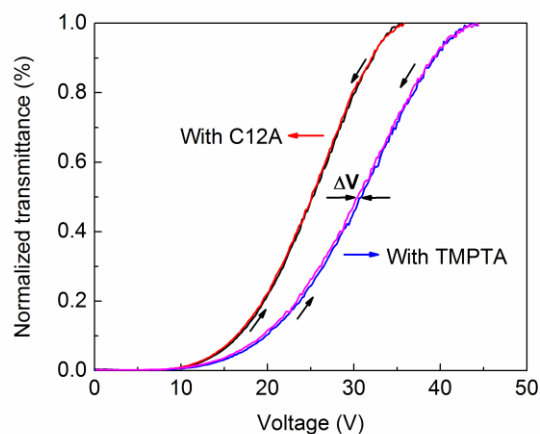


Figure 27. Hysteresis loop for Sample A and Sample B.

Fast response time is probably the most attractive feature for BPLC. Both rise time and decay time were measured between 10% and 90% transmittance change. The measured decay time at room temperature (21 °C) for Sample A is 332.5 μ s, and rise time is 541.9 μ s. On the other hand, Sample B exhibits much faster response, with decay time of 39.4 μ s, and rise time of 46 μ s. We believe that the fast response time originates from the short pitch length and strong polymer network. Based on Equation (19), the decay time is proportional to p^2 , so a shorter pitch length would lead to a faster response time. On the other hand, TMPTA is a tri-functional monomer, while the normally used EHA or C12A¹⁵⁸ are mono-functional monomers. The crosslink between TMPTA and RM257 is much stronger, which helps the molecules to relax back when the voltage is released.

Table 7. Comparison between Sample A and Sample B.

Sample	Compositions					V_{on} (V)	K (nm/V ²)	Hysteresis		Decay time (μ s)
	BP host	RM257	C12A	TMPTA	PI			Drive to 35.8V	Drive to 44V	
A	89.2 wt%	6 wt%	4 wt%	0	0.8 wt%	35.8	0.97	~0	1.8%	332.5
B	89.2 wt%	6 wt%	0	4 wt%	0.8 wt%	44.2	0.6	~0	0.68%	39.4

In addition, the decay time decreases as the temperature increases, as described by Equation (25).¹⁵⁶ This equation is derived based on the order parameter S as described in Ref. ⁵⁰, and the denominator $(1 - T / T_{c_BP})^\beta$ is the approximated expression for S using Haller's semi-empirical equation. This approximation is valid only for the temperature not too close to T_{c_BP} (e.g., $T_{c_BP} - T > 1^\circ\text{C}$). Although Equation (25) has three unknowns (B , E_a , and β), β can be obtained by measuring the temperature dependent birefringence of the LC host JM2069-145 or the BPLC composite.¹¹⁶ The Δn of the LC host was measured through phase retardation of a homogeneous cell sandwiched between two crossed polarizers. The results are fitted by Equation (8). The blue line in Figure 28 shows the measured temperature dependent Δn of our LC host at $\lambda=633$ nm. Through fitting, we found $\Delta n_o=0.350$ and $\beta=0.267$.

Next, we measured the temperature dependent decay times of our Sample B, since it has a much faster response time. Results are depicted in Figure 28. As the temperature increases from 25.4 °C to 44.3 °C, the peak voltage increases slightly from 44.2 V to 50 V because of the reduced Kerr constant. Meanwhile, the decay time is reduced from 32.8 μ s to 9.63 μ s. We used

the same β value to fit the decay time data by Equation (25), and found quite good agreement. From the fitting, we obtained $E_a=613.5$ meV and $B=7.35\cdot 10^{-10}$ μs . This activation energy is smaller than that of JNC's JC-BP01M whose $\Delta\varepsilon\approx 94$, Kerr constant is 7.5 nm/V², but its response time at 23°C is 870 μs in a 5.74 μm VFS cell.^{109,110}

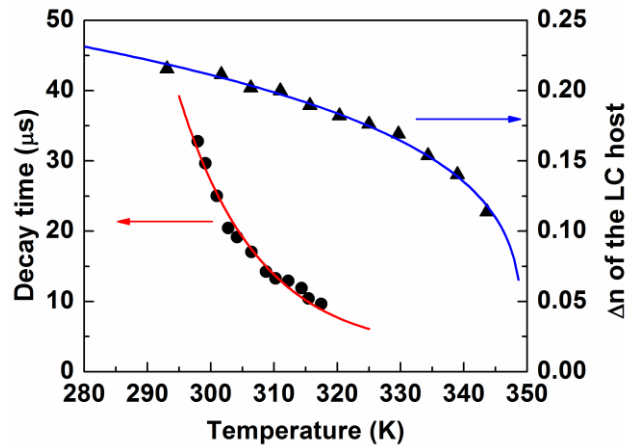


Figure 28. Blue line: Temperature dependent Δn of the LC host; Red line: Temperature dependent decay time for the VFS PSBP cell (Sample B). Dots: experimental data.

In conclusion, we compared two PS-BPLC samples using different types of monomers (C12A or TMPTA), and find out that the response time of the PS-BPLC with TMPTA is much faster. By using TMPTA, we demonstrated a microsecond-response and “hysteresis-free” ($\leq 0.68\%$) polymer-stabilized BPLC device. The decay time at room temperature is 39.4 μs , and is reduced to 9.64 μs as the temperature increases to 44.3 °C. The peak voltage is 44.2 V and the contrast ratio is over 1300:1. With these attractive features, our PS-BPLC exhibits great potential for next generation high speed display and photonics devices.

3.4.2 Large Kerr Constant and Low Voltage Blue Phase Liquid Crystal

3.4.2.1 Large $\Delta\varepsilon$ LC host

We prepared a large $\Delta\varepsilon$ nematic LC host JC-BP06N (by JNC) whose clearing point is $T_c=73.8^\circ\text{C}$. To evaluate the birefringence of the LC host, we measured the phase retardation of a homogeneous cell sandwiched between two crossed polarizers.⁴⁹ The cell has strong anchoring energy and cell gap $d\sim 5\ \mu\text{m}$. A 100 Hz square-wave AC voltage was applied to the LC cell. In this experiment, we employed a tunable Argon ion laser ($\lambda=514\ \text{nm}$) as the probing light source. Unfortunately, this LC host does not align well in the homogeneous cell.

As shown in Figure 29(a), when the LC alignment direction is parallel to the optic axis of the polarizer, the cell shows severe light leakage between crossed polarizers, indicating the bulky LC molecules do not follow the rubbing direction perfectly. The voltage-dependent transmittance (VT) curve shown in Figure 29(c) also suggests a poor alignment, because the transmittance (blue line) does not touch 0. The Δn cannot be measured accurately due to poor alignment. Similar alignment problem of negative $\Delta\varepsilon$ LCs in vertically aligned (VA) cells has been reported before, and diluters can be used to improve the alignment.⁷⁷ Therefore, we doped 5 wt% diluter: 4-pentyl-4'-propyl-1,1'-bi(cyclohexyl) (5CC3) into JC-BP06N. For convenience, let us call this mixture LC1 and its T_c is measured to be 74°C , which is similar to JC-BP06N. LC1 shows good alignment and it appears dark under crossed polarizers when the alignment direction is parallel to the optic axis of the polarizer, as shown in Figure 29(b). The contrast ratio can be further improved by doping more diluters, but the tradeoff is the reduced $\Delta\varepsilon$ and Δn . From the VT curve, we can calculate the phase retardation and then birefringence, and the obtained result is $\Delta n=0.156$. Through the relaxation time measurement of the homogeneous cell,⁵⁴ we obtained the

viscoelastic constant $\gamma_1/k_{11} = 199 \text{ ms}/\mu\text{m}^2$, and rotational viscosity $\gamma_1 = 1.47 \text{ Pas}$. This γ_1/k_{11} is about 10X larger than that of nematic E7 mixture. Diluter tends to decrease Δn of the large $\Delta\epsilon$ LC slightly and γ_1 dramatically. Therefore, JC-BP06N should have a larger viscosity and slightly higher Δn (~ 0.17) than LC1.

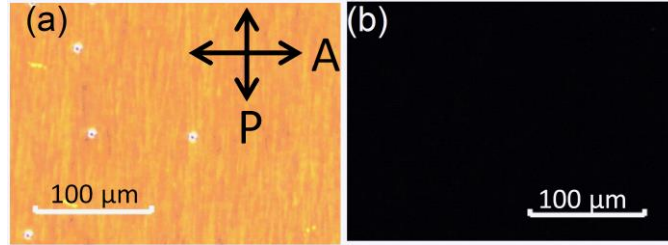


Figure 29. POM images of the homogeneous cells filled with (a) JC-BP06N and (b) LC1 (with alignment direction parallel to the optic axis of the polarizer).

Dielectric anisotropy of a LC is defined as $\Delta\epsilon = \epsilon_{//}' - \epsilon_{\perp}'$, here $\epsilon_{//}'$ and ϵ_{\perp}' represent the real part of the parallel and perpendicular dielectric permittivity. To determine the $\Delta\epsilon$ of these two LCs, we measured the capacitance of a homogeneous cell and a VA cell using an HP-4274 multi-frequency LCR meter.⁵⁴ Both LCs align well in the VA cell. However, the poor alignment of JC-BP06N in the homogeneous cell could result in a larger ϵ_{\perp}' than the actual value. The measured ϵ_{\perp}' of JC-BP06N is 17.9 at 100 Hz, which is much smaller than $\epsilon_{//}'(491)$, therefore the error in ϵ_{\perp}' will not affect $\Delta\epsilon$ too much.

Figure 30 depicts the measured results. The solid and open circles are the measured $\epsilon_{//}'$ for JC-BP06N and LC1, respectively and the lines are fitting results with Equation (24).^{152,153} From these data, we obtain $\epsilon_0 = 491$ at low frequency region for JC-BP06N. As the frequency increases,

$\epsilon_{//}'$ decreases dramatically due to the slow dielectric relaxation time resulting from the large viscosity and bulky molecular structure.¹¹⁸

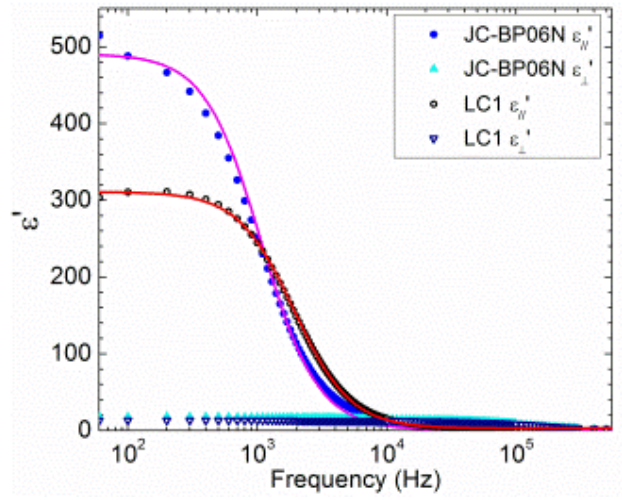


Figure 30. Frequency-dependent $\epsilon_{//}'$ and ϵ_{\perp}' of JC-BP06N and LC1.

Through fitting with Equation (24), we find $f_r=1.07$ kHz. For conventional nematic LCs, the relaxation frequency is usually quite high (>50 kHz). After doping a small amount of diluter, the f_r of LC1 shifts to 1.92 kHz because of the dramatically reduced viscosity.¹¹⁷ However, ϵ_0 drops significantly from 491 to 311 after adding 5wt% 5CC3. The small molecules of 5CC3 are uniformly distributed in JC-BP06N. According to Lichtenecker formula, the dielectric constant ϵ_m of a binary mixture of liquids can be expressed as:¹⁵⁹

$$\epsilon_m = \exp(\epsilon_1 \ln(\Omega_1) + \epsilon_2 \ln(1 - \Omega_1)), \quad (26)$$

where ϵ_1 and ϵ_2 are the parallel dielectric constant of the two components and Ω_1 is the volume fraction of component 1. If we substitute $\epsilon_1=2.35$ (measured data for 5CC3), $\epsilon_2=491$, and $\Omega_1=0.05$ (wt%) into Equation (26), we find $\epsilon_m=376$. However, Ω_1 should be larger than the wt%

because of the smaller molecular weight of 5CC3, compared to JC-BP06N. If we assume $\Omega_I=0.085$, then we obtain $\epsilon_m=312$, which is quite close to the measured result (~ 311).

3.4.2.2 PSBP Properties

Although we are able to get good alignment and measure the physical properties of LC1, LC1 has much smaller $\Delta\epsilon$ (298 vs. 473) and will result in much smaller K than JC-BP06N. Therefore, we prepared a PSBP sample employing JC-BP06N. The blue phase precursor consists of 88.17 wt% JC-BP06N with 2.92 wt% of chiral dopant R5011 (HCCH), 5.24 wt% RM257 (Merck), 3.46 wt% TMPTA and 0.21 wt% photoinitiator. Next, we injected the LC/monomers mixture into a VFS cell¹⁰⁹ in an isotropic phase. The VFS cell is comprised of two ITO (indium tin oxide) glass substrates, but without polyimide alignment layer. The cell gap is controlled at ~ 3.2 μm . Afterwards the cell was cooled to blue phase and then exposed to UV light ($\lambda\sim 365$ nm) with intensity of 2 mW/cm² for 30 minutes. After UV irradiation, nano-structured BPLC composites were self-assembled. The measured Bragg reflection wavelength is ~ 380 nm, which is about the same as that of JC-BP01M (our benchmarking BPLC material).

The experimental setup for characterizing the electro-optic properties of a VFS cell has been reported previously.¹⁰⁹ A linearly polarized Argon ion laser ($\lambda=457$ nm and $\lambda=514$ nm) and a He-Ne laser ($\lambda=633$ nm) were used as probing beams. In order to acquire phase retardation, the laser beam was incident on the VFS cell at 70° oblique angle. The VFS cell was immersed in a transparent container filled with Glycerol ($n=1.47$) so that the beam could enter the LC layer at a large angle due to the refractive index match between the glass and Glycerol. The container was

placed between two crossed polarizers, and the light transmittance was measured by a photodiode detector.

In order to compare the electro-optic properties of our PS-BPLC to JC-BP01M,¹¹⁰ we measured our cell using the same driving frequency 100 Hz. As shown in Figure 30, the $\Delta\varepsilon$ of JC-BP06N decreases as frequency increases. Accordingly, the Kerr constant will decrease following the extended Coles-Coles model.¹¹⁹ Ideally, a driving frequency higher than 180Hz is required for color sequential displays. If we increase the driving frequency to 240 Hz, Kerr constant will drop by 8%, which in turn increases the on-state voltage by ~4%. This prediction is validated experimentally.

Figure 31 depicts the measured VT curve at different wavelengths. Here, the transmittance is normalized to that of two parallel polarizers. From Figure 31, we find the on-state voltage (corresponding to peak transmittance) is $V_{on} = 7.3, 8.4$ and $9.9 V_{rms}$ for $\lambda=457, 514$ and 633 nm, respectively. In the voltage-off state, blue phase is not perfectly optically isotropic but with a tiny optically rotatory power.¹²³ At $\lambda=514$ nm, our measured contrast ratio (CR) is 580:1 under crossed polarizers. If we rotate the analyzer by 1.8° , CR is boosted to 1900:1. It can be further improved by shifting the Bragg reflection wavelength to the shorter wavelength side, but the operating voltage will increase. The depolarization from the oblique incidence might also degrade CR. As voltage increases, the induced birefringence increases as described by Equation (22). Through fitting the VT curves,¹⁹ we obtained $K=\Delta n_s/(\lambda E_s^2)=24.9, 20.9$ and 17.4 nm/V² for $\lambda=457, 514$ and 633 nm, respectively. For comparison, at $\lambda=633$ nm the Kerr constant of our

BPLC is $\sim 2.3X$ larger than that of JC-BP01M (also from VFS cell). We also studied the IPS cells and results will be discussed later.

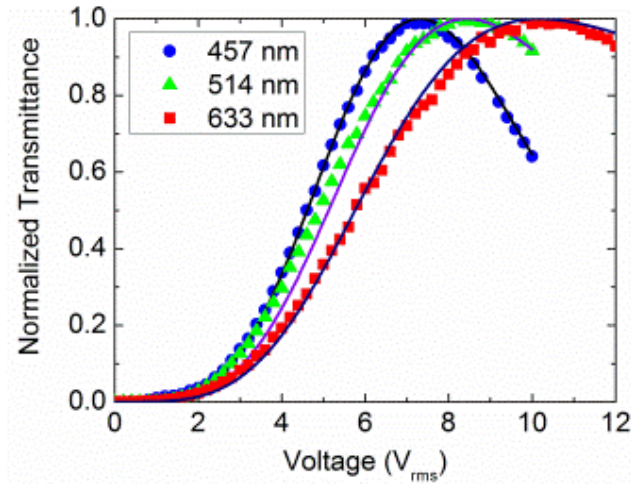


Figure 31. VT curves of the VFS cell at the specified wavelengths. Dots are measured data and lines are fitted curves with extended Kerr model. Cell gap $d=3.2 \mu\text{m}$

Next, we measured the rise time and decay time of the VFS cell by swinging the voltage between 0 and V_{on} . The response time is defined as 90% to 10% transmittance change. At $\lambda=514$ nm and room temperature, the rise time is 460 μs and decay time is 950 μs . It is known that the BPLC response time in the low field region where lattice distortion does not occur is primarily governed by the viscosity, average elastic constant, and pitch length.^{23,113} Polymer structure and polymer concentration also play important roles.¹³⁰ Although the viscosity of our JC-BP06N is quite high, the monomer (TMPTA) we employed has three functional groups which provides strong crosslinking networks and helps reduce the response time. A tradeoff is higher voltage.

Hysteresis affects grayscale accuracy of a BPLC device and should be minimized.¹⁶⁰ To characterize hysteresis, we drove the VFS cell by ascending the voltage to V_{on} and then gradually descending it to 0. Hysteresis is defined as $\Delta V/V_{on}$, where ΔV is the voltage difference between

the forward and backward scans at half of the peak transmittance. For the VFS cell, the measured hysteresis is only $\sim 0.9\%$ ($\Delta V=0.08\text{V}$) at $\lambda=514\text{ nm}$, which is negligible. If the applied voltage exceeds $8.4\text{ V}_{\text{rms}}$, then the hysteresis will gradually increase. Here we define a critical field as $E_c=V_{on}/d$. For the BPLC we studied, its $E_c=2.67\text{ V}/\mu\text{m}$. Above E_c , hysteresis will gradually grow and response time becomes slower.^{157,161} Therefore, the cell gap of a VFS cell plays an important role affecting the on-state voltage and hysteresis.

For VFS mode, the on-state voltage depends on the cell gap. When a BPLC layer is subject to a longitudinal field, the induced birefringence is along the electric field direction and the cell behaves as a C-plate.⁸⁴ The phase retardation can be described by:

$$\Gamma = \frac{2\pi}{\lambda} n_o d \left[\sqrt{1 - \frac{n_g^2 \sin^2 \theta}{n_e^2}} - \sqrt{1 - \frac{n_g^2 \sin^2 \theta}{n_o^2}} \right], \quad (27)$$

where n_g is the refractive index of Glycerol, θ is the incident angle, and n_e and n_o are the ordinary and extraordinary refractive indices of the BPLC. When $\Gamma(V)=\pi$, we get the peak transmittance and V_{on} under crossed polarizers. We assume the following equations hold for n_e and n_o .¹⁴⁰

$$\begin{aligned} n_o &= n_i - \Delta n / 3, \\ n_e &= n_i + 2\Delta n / 3, \end{aligned} \quad (28)$$

where n_i is the isotropic refractive index of BPLC in the voltage-off state. Combining Equation (27) and Equation (28) and plugging the fitting parameters E_s and Δn_s , we can obtain n_o , n_e and hence Γ at different voltages. Figure 32 depicts the cell gap effect on V_{on} . A thinner cell gap results in a stronger electric field so that the induced birefringence is larger, which in turn lowers V_{on} . However, as d continually decreases the accumulated phase retardation would be smaller

than 1π . Eventually, V_{on} will increase as the cell gap gets too thin. When d varies from $2.13 \mu\text{m}$ to $5.9 \mu\text{m}$, V_{on} stays below 10V for our PS-BPLC. However, to suppress hysteresis, the peak electric field should not exceed the critical field E_c , i.e., $V_{on} < E_c * d$. In Figure 32, the red dashed lines show the critical voltage ($E_c * d$) for different cell gaps. To keep hysteresis negligible, the cell gap should be larger than $3.1 \mu\text{m}$. Therefore, the optimized cell gap should be $3.1 \mu\text{m} < d < 5.9 \mu\text{m}$.

The above discussions are all focused on VFS cell, in which the electric field is in longitudinal direction. VFS mode offers several spectacular properties, such as low voltage, high transmittance, fast response time, and negligible hysteresis. However, it requires a directional backlight and sophisticated phase compensation in order to achieve wide view.¹⁶² Another possible driving method is to use fringing field generated from in-plane switching (IPS) electrodes. The major advantages of IPS mode are twofold: 1) a normal backlight can be used, and 2) wide viewing angle can be obtained by a simple biaxial compensation film.⁸⁴

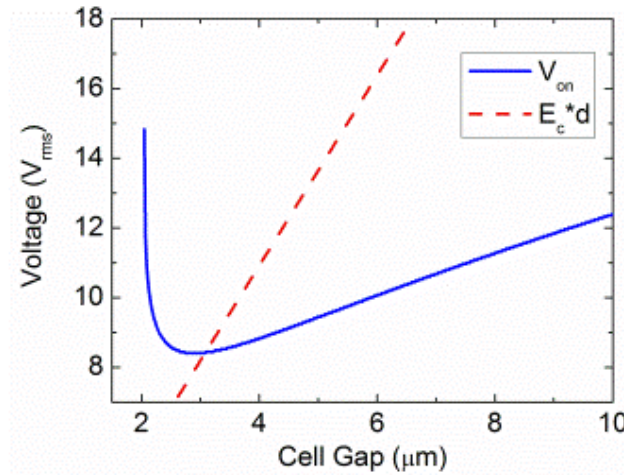


Figure 32. Cell gap effect on V_{on} and optimized cell gap for hysteresis-free and $V_{on} < 10\text{V}$.

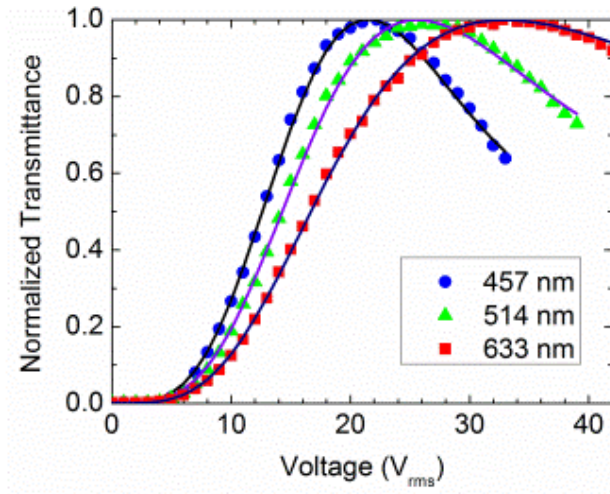


Figure 33. The VT curves (data and fitting) at the specified wavelengths of an IPS-5/5 cell.

In experiment, we filled the PS-BPLC to an IPS-5/5 cell: the electrode width and gap are both $5\mu\text{m}$, and cell gap is $7\mu\text{m}$. The PSBP stabilization procedure is the same as the VFS cell. After polymer stabilization, the IPS cell was sandwiched between two crossed polarizers and the voltage dependent transmitted light was focused by a lens so that different diffraction orders²⁴ can be collected by the detector. The peak transmittance of the IPS-5/5 cell is about 60% because of the dead zones on top of the electrodes. Figure 33 is a plot of the normalized transmittance at different wavelengths. From Figure 33, we find $V_{on}= 22.2, 25.4$ and $32.8 V_{rms}$ at $\lambda=457, 514$ and 633 nm , respectively. Through fitting the data with the extended Kerr model,^{19,140} we get $K=39.7, 33.1,$ and 26.9 nm/V^2 , correspondingly. These Kerr constants are larger than those obtained from VFS cell because of the nonuniform electric field distribution in the IPS cell. By contrast, the Kerr constant of our BPLC is $\sim 2.1\text{X}$ larger than that of JC-BP01M at room temperature (also in IPS cell).¹¹⁰ This improvement is close to 2.3X by using the VFS cells,

considering the measurement and fitting errors. So, on average our PS-BPLC shows a 2.2X larger Kerr constant than JC-BP01M.

3.4.2.3 Conclusion

In conclusion, we have demonstrated a BPLC host with $\Delta\varepsilon\sim 470$ and estimated $\Delta n\sim 0.17$. Good alignment of this BPLC in homogeneous cells was obtained by doping ~ 5 wt% of a diluter so that its physical properties can be estimated. Using such a huge $\Delta\varepsilon$ BPLC in a 3.2- μm VFS cell, we have achieved following outstanding results: operation voltage ~ 8.4 V_{rms}, rise time ~ 460 μs and decay time ~ 950 μs at room temperature ($\sim 22^\circ\text{C}$), and hysteresis $\sim 0.9\%$. The Kerr constant is about 2.2X higher than previous record.

3.4.3 Electric Field-Induced Monodomain Blue Phase

Both transmissive and reflective BPLC devices have been demonstrated. In transmissive mode, Bragg reflection is shifted to ultraviolet region by employing a high concentration chiral dopant so that it is optically isotropic in the visible spectral region. To realize amplitude modulation, the BPLC is sandwiched between two crossed polarizers. Both fringing field and longitudinal field can be used, depending on the device configurations. On the other hand, for reflective mode the pitch length is adjusted to reflect colors in the visible region and no polarizer is needed. As a result, flexible display can also be realized.

Electrically tunable colors using BPLCs have been demonstrated based on the deformation of blue phase lattice.^{137,163,164} However for polymer-stabilized blue phases, the cubic structures are stabilized by polymer network so that the lattice deformation can only take place in the high field region.¹⁶⁵ In the weak field region, the applied electric field mainly reorients the LC molecules,

but not deforms the lattices. Recently, a vivid full-color reflective display using surface alignment-induced monodomain PS-BPLC has been demonstrated.^{104,166} It exhibits several attractive features, such as no need for a polarizer and color filters, relatively narrow reflection band, submillisecond response time, and analogous grayscales by controlling the applied voltage. However, the voltage will be partially shielded by the surface alignment layer because of the large dielectric constant ($\Delta\epsilon\sim 100$) of the employed BPLC.⁸² Besides reflective displays, monodomain blue phase has also been used in photonics application, such as lasing,^{27,100,128} where large area and uniform monodomain blue phase is critical.

In this session, we demonstrate a large area vertical field-induced monodomain BPLC without any alignment layer. To distinguish from conventional multidomain structures, here we refer to monodomain as having a poly-crystalline structure but with the same lattice orientation. The electric field is used to rotate the blue phase lattice and induce uniform texture.^{136,167} As a result, Bragg reflection has a narrower bandwidth so that the reflected color looks vivid.

The Bragg reflection wavelength of a BPLC is governed by the lattice structure as described in Equation (20).¹²⁹ When blue phase grows from isotropic phase without any electric field, multiple diffraction peaks can be observed from (110), (200) and (211) directions (with these lattice surfaces parallel to the substrate) of BP-I.¹²⁹ To generate narrow band reflection color, we applied a uniform electric field (E) perpendicular to the substrates to change the lattice orientation. The torque Γ exerted on the blue phase lattice of volume Ω can be described by:¹³⁶

$$\Gamma = \Omega A \sum_{i=1}^3 (n_i \cdot E)^3 (n_i \times E) = \Omega p \left[E_2 E_3 (E_2^2 - E_3^2) n_1 + E_1 E_3 (E_3^2 - E_1^2) n_2 + E_1 E_2 (E_1^2 - E_2^2) n_3 \right], (29)$$

where p is a proportional coefficient dependent on the material and n_i is the unit vector. When one of the following conditions is met, the torque will vanish: 1) $|E_1|=|E_2|=|E_3|$, i.e., E is normal to the (111) surface; 2) $E_i=E_j=0$ and $|E_k|\neq 0$; $i=1,2,3$; $i\neq j\neq k$, i.e., E is normal to the (100) surface; and 3) $E_i=0$ and $|E_j|=|E_k|$; $i=1,2,3$; $i\neq j\neq k$, i.e., E is normal to the (110) surface. Thus, when the multi-domain BP lattice is subject to an electric field, the nonzero torque will rotate the lattice to the nearest stable position where $\Gamma=0$. To prove the concept, we prepared vertical field switching (VFS) cells, comprised of two ITO (indium tin oxide) glass substrates but without polyimide alignment layer. The cell gap was controlled at 5 μm . The blue phase textures with and without electric effect are compared.

In experiment, we used HTG-135200 (mentioned in Session 3.3.3) as the nematic LC host. Its physical properties are listed as follows: $\Delta n=0.205$ at $\lambda=633$ nm, $\Delta\varepsilon=99$ at 1 kHz, $\gamma_1=700$ mPa·s at 25 °C, and clearing temperature $T_c=98$ °C. To tune the reflection band from red to green and blue, we prepared BPLC mixtures with different concentration of chiral dopant R5011 (HCCH). The chiral concentration is 3.46wt%, 3.94wt% and 4.47wt% for the red, green and blue cells, respectively. Afterwards, 10 wt% of photocurable monomers [6 wt% RM257 (Merck) + 4 wt% TMPTA] and 0.1 wt% of photoinitiator were blended with 89.9 wt% of the BPLC mixture to form the precursor. Next, we injected the LC/monomers mixture into a VFS cell and the cell was cooled to BP phase. Different domains with different reflective colors appear, as shown in Figure 20(a), (c), and (e). When the cell is subject to an AC electric field (1 kHz) of $\sim 2\text{V}/\mu\text{m}$ for about 1s before UV curing, the torque created by the electric field helps to reorient the blue phase lattice. In our case, the (110) surface tends to align perpendicular to the electric field and the

reflective color becomes uniform, shown in Figure 20(b), (d), and (f). The preferred electric field strength depends on the blue phase material, pitch length and temperature.

Empirically, a smaller dielectric anisotropy and shorter pitch blue phase at a temperature closer to the chiral nematic phase requires a stronger electric field. As shown in Figure 20(b), (d) and (f), mono-domain blue phase is formed after the electric field pulse. Once the voltage is removed, the uniform BP texture remains unless it is heated up to an isotropic phase. These cells were then exposed to UV light ($\lambda=365$ nm) with intensity of 6 mW/cm^2 for 10 min. After UV irradiation, polymer-stabilized BPLC nano-composites were self-assembled and the blue phase textures were stabilized.

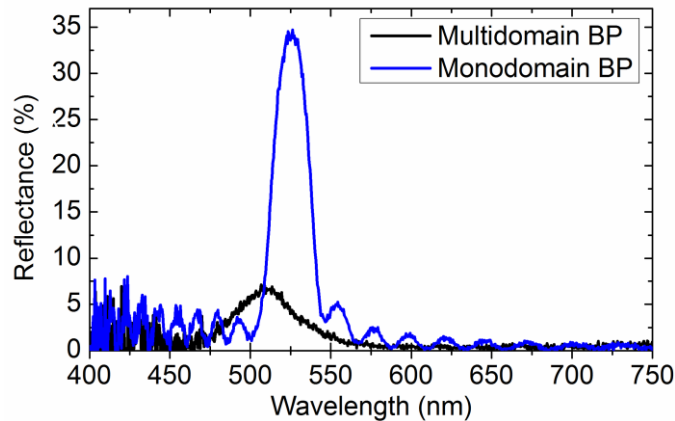


Figure 34. Measured reflection spectra of the green PSBP cell.

To quantitatively compare the differences between multi-domain and mono-domain blue phase cells, we measured their reflection spectra. A DH-2000 unpolarized light source (Mikropack) was coupled into a multi-mode fiber and incident on the PSBP cell normally. The reflected light was coupled back to the fiber and recorded by a high resolution spectrometer (HR2000 CG-UV-NIR, Ocean Optics). The reflection spectrum was normalized to that of a

mirror. To avoid reflection from the glass and air surface, we attached an anti-reflection (AR) film to the front surface and a black tape to the back surface. Figure 34 depicts the measured reflection spectra of the green PSBP cell. Without electric field effect, the blue phase shows a relatively low reflectance (black line). By contrast, the electric field-induced mono-domain blue phase exhibits a fairly high reflectance and narrow bandwidth (blue line). The peak reflectance (R_p) of the green cell is 35% at $\lambda=527\text{nm}$. The full width at half maximum (FWHM) of the reflection band is about 25 nm, so the appearance color is quite saturated and vivid. From here on, we will focus on the measured properties of electric field-induced mono-domain blue phase.

The reflection spectra of red and blue cells were also measured [Figure 35(a) and (c)]. Blue cell shows a reasonably high reflectance $R_p\sim 35.4\%$ at $\lambda\sim 472\text{ nm}$ and FWHM $\sim 21.4\text{ nm}$. For the red cell, its peak reflectance ($R_p\sim 25.3\%$) occurs at $\lambda=628\text{ nm}$ and FWHM $\sim 35.2\text{ nm}$. The lower reflectance for the red cell is because Bragg reflection requires about ten pitch periods to establish. For a 5- μm cell gap, the red cell has fewer pitch periods because of its longer pitch. When an AC voltage is applied, the double-twist cylinders are gradually unwound, which leads to a decreased reflectance.

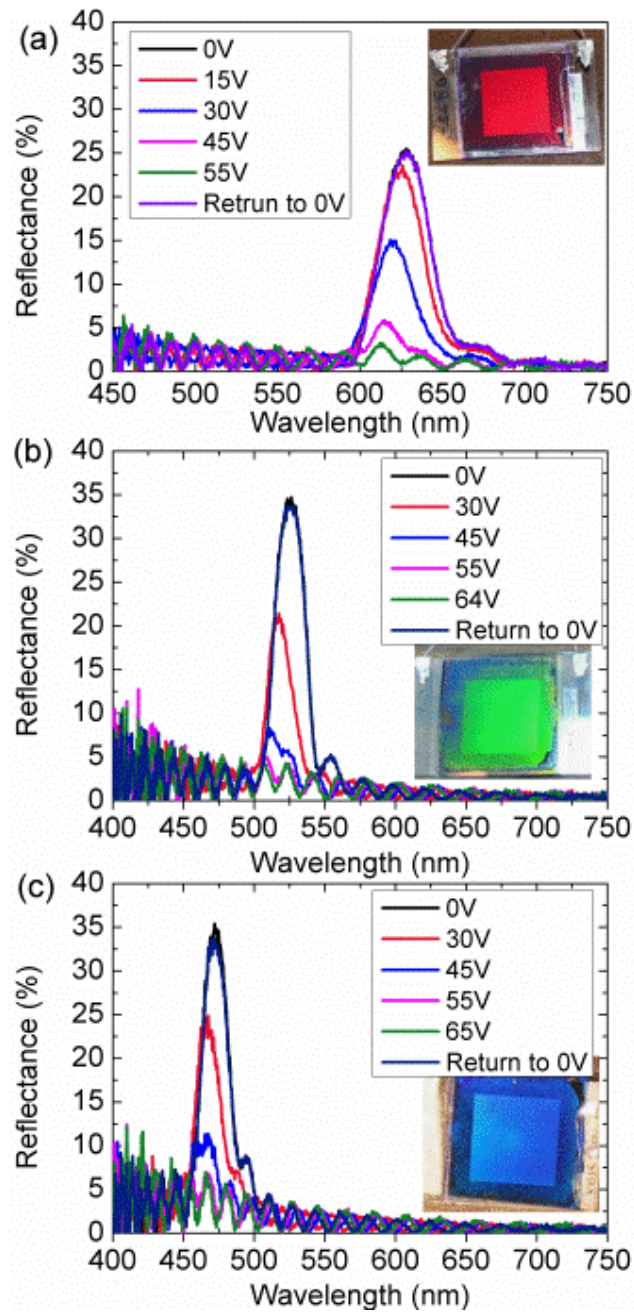


Figure 35 Reflection spectra at different voltages for (a) red, (b) green, and (c) blue cells. The inset photos are the corresponding images at 0V (ITO area in the center: 12mm X 12mm).

Figure 35 depicts the reflection spectra at different operating voltages for the red, green and blue cells. Analogous grayscale can be controlled by the applied voltage. A tiny blue shift (<5

nm) on the peak reflection wavelength is observed, indicating the lattice deformation of the PS-BPLC is very minor. The reflection drops to baseline as the voltage keeps increasing. This is because the LC molecules have been reoriented by the electric field. The reflectance (R_0) at a high voltage gives the dark state. The contrast ratio (CR) is defined as R_p/R_0 . To improve CR, we should minimize R_0 , which is governed by the reflections of the ITO/PSBP and ITO/glass interfaces. A more noticeable R_0 is found for the blue BPLC cell because of the increased index mismatch between the ITO/PSBP and ITO/glass. The calculated CR is 9.4:1 at 65V, 14.9:1 at 64V and 16.6:1 at 55V for the blue, green, and red cells, respectively. The CR can also be improved with the index-matched electrode. To reduce operation voltage, a BPLC with a larger Kerr constant can be considered.¹¹⁰⁻¹¹²

The properties of reflected light from the PSBP cells are also studied. The inset plots in the Figure 36 show the reflected beam pattern from a red cell (right) and a green cell (left) for example. A He-Ne laser beam was used as a probing beam for the red cell, and an Argon laser beam ($\lambda=514\text{nm}$) for the green cell, respectively. The incident angle was kept small ($<5^\circ$). The intensity distribution of the reflection pattern is quite symmetric, and the FWHM angle is about 8° for the red cell, based on the angular intensity distribution plotted in Figure 36. This phenomenon happens to the blue and green cells as well, but with a smaller spreading angle. For the green cell, the reflective beam size is more collimated compared to the red cell, as shown in Figure 36. The FWHM angle is estimated to be 2.4° . Unlike the surface alignment-induced mono-domain blue phase which exhibits a specular reflection as a mirror does, the electric field-induced mono-domain blue phase is slightly diffusive. Before UV stabilization, the short electric

field pulse helps to rotate the BP lattice and align (110) surface parallel to the substrate. When the electric field is released, some of the (110) planes tend to relax back to the original state to some extent, but there is insufficient energy for these lattices to relax back because of the high viscosity of BP, resulting in some slightly tilted planes and hence the diffusive reflected beam. In the red cell, the viscosity is smaller due to the lower chiral dopant concentration and higher BP temperature range than that of the green and blue cells. Thus, the BP lattice of the red cell has freedom to rotate more, leading to a larger spreading angle in the reflected beam. This intrinsic diffusive reflection also helps to widen the viewing angle.

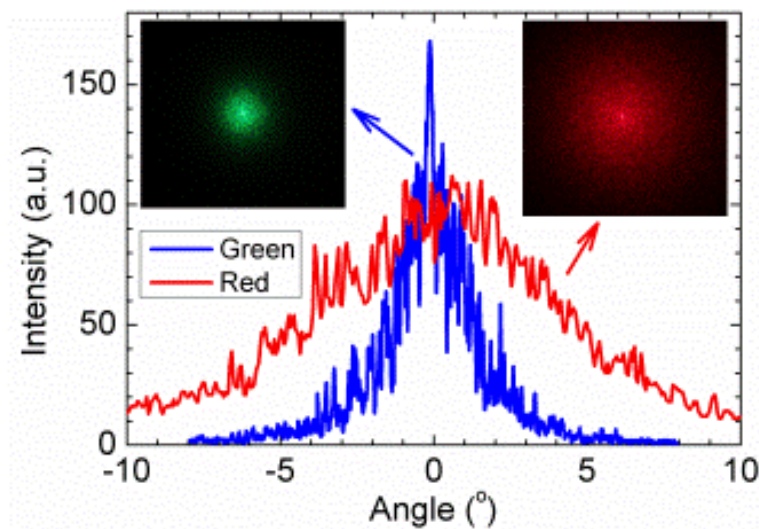


Figure 36 Angular intensity distribution of the reflected beam from the red and green PBLC cell (Incident light: He-Ne laser beam for red cell and Argon laser beam for the green cell). Inset plots show the beam patterns.

To study the viewing angle performance of the cells, we did an outdoor experiment and took pictures of the red, green and blue cells at different viewing angles, as Figure 37 shows. When viewing at normal direction (0°), we can observe vivid colors for all the red, green and blue cells. The actual color appears more saturated when viewing with eyes, as the CCD camera tends to

degrade the color quality. At 20° , we can still see vivid colors but the blue shift is gradually taking place, since blue phase has well organized photonic crystalline structure and has intrinsic angular dependent reflection wavelength. The blue shift becomes more evident as the viewing angle increases to $\sim 45^\circ$, which is consistent with those results reported previously.¹⁶⁸

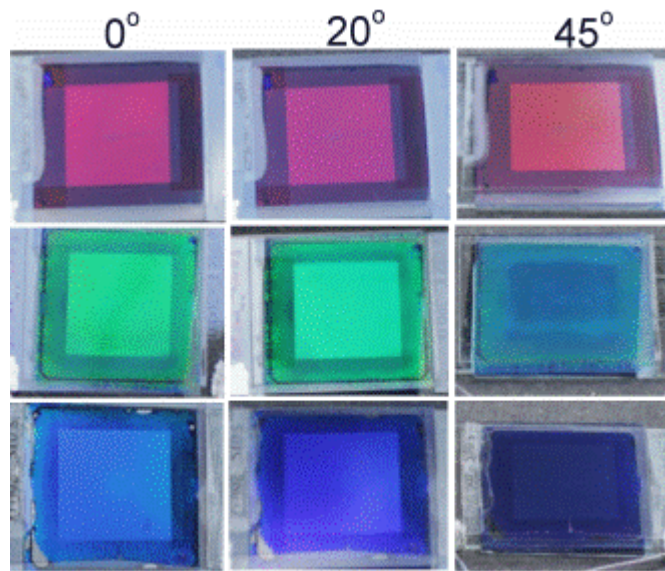


Figure 37. Outdoor viewing angle performance of the R, G, and B cells.

The voltage-dependent reflectance (VR) curve and the response time were measured using a He-Ne laser for the red cell as an example. Based on the above mentioned property, the reflected beam is divergent and a portion of the light is not coupled back into the fiber and the spectrometer. Therefore, a lens is inserted between the PSBP cell and the photodiode detector (New Focus Model 2031) to collect most of the reflected light. A 1-kHz square-wave AC signal was applied to the VFS cell, and the corresponding reflectance was recorded by a LabVIEW system. For a linearly polarized (LP) incident light, the reflectance is 34.4% at 0V and drops to 1.4% at 56V, shown as the black line in Figure 38. The dark state light leakage comes from the

reflection of the ITO/PSBP and ITO/glass interfaces. The CR is about 24.8:1 at $\lambda=633$ nm. A $\lambda/4$ plate was inserted to change the polarization state of the incident light. For the right-handed circularly polarized (RCP) light, the reflectance is 65.4%, which is almost doubled compared to the LP incident light. On the contrary, the reflectance is only 3.2% (red dot in Figure 38) when the incident light is left-handed circularly polarized (LCP). The chiral dopant used in our PSBP system is right handed, so only the RCP will be reflected. For a PSBP system with left-hand chiral dopant, only LCP light will be reflected. This polarization selectivity in the reflection makes this device promising for many photonic and display devices.

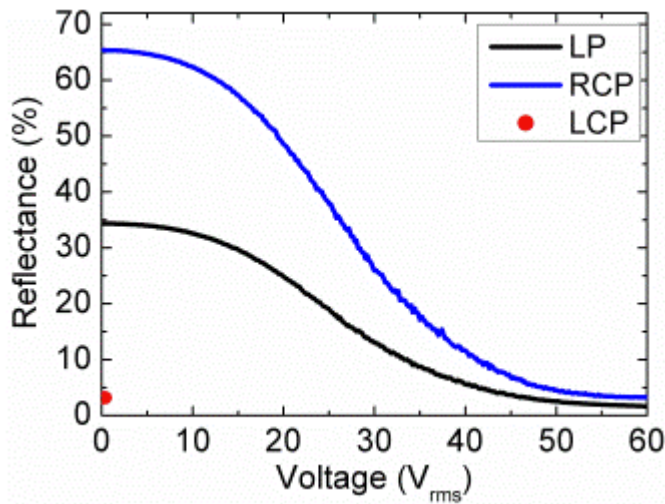


Figure 38. Measured VR curves for LP and RCP incident lights, and reflectance for LCP at 0V.

Fast response time is one of the most attractive features for BPLC. Both rise time and decay time were measured between 10% and 90% transmittance change. The measured decay time (56V-0V) at room temperature is 814 μ s, and rise time (0V-56V) is 64 μ s. Such a fast response time enables video-rate operation of the reflective display without image blurring.

There have been some arguments about the polarization state of the reflected light of blue phase liquid crystals.^{102,104,128,169,170} Here we experimentally investigated the polarization state with a $\lambda/4$ plate and a linear polarizer inserted before the detector. The reflected light is right-handed for both RCP and LP incident beams. We rotated the linear polarizer in front of the detector in step of 10° , and recorded the light intensity. Figure 39 shows the polarization ellipse of the reflected light for both RCP and LP incident lights. The ellipticity is defined as the ratio of the major axis to the minor axis of the polarization ellipse. Ellipticity of 0 or ∞ represents LP and ellipticity of 1 means circular polarization. The measured ellipticity of the reflected light is 0.985 and 0.991 for the RCP and LP incident lights, respectively, indicating the light is very close to circularly polarized, regardless of the polarization state of the incident light. Unlike the surface alignment induced mono-domain BP,¹⁰⁴ the alignment layers can also affect the LC molecular orientation which would further affect the polarization state, and resulting in a lower ellipticity.

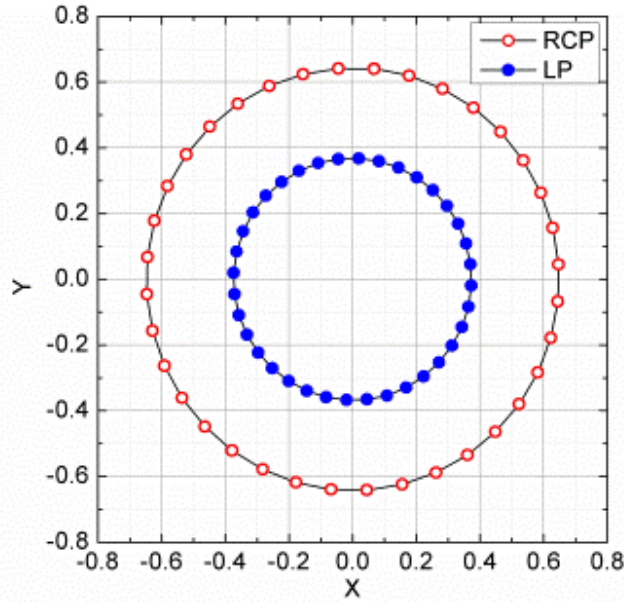


Figure 39. Polarization state of the reflected light for RCP (open circle) and LP (solid circle) incident beams.

In summary, we have demonstrated an electric field-induced mono-domain blue phase and its application for reflective displays. The reflection spectra for red, green and blue cells were studied. The bandwidth is fairly narrow so the color looks saturated and vivid. The reflectance gradually decreases with the increasing operating voltage, and analogous grayscales can be achieved. With analog grayscales and submillisecond response time, videos can be displayed using this reflective PSBP. Moreover, the electric-field-induced mono-domain blue phase selectively only reflects RCP light when the employed chiral dopant is right-handed, and the reflected light is almost circularly polarized.

CHAPTER FOUR: LOW ABSORPTION LIQUID CRYSTALS FOR MID-WAVE INFRARED APPLICATIONS

In previous chapters, we mainly focused on display applications in visible spectral range. Besides that, linearly conjugated liquid crystals also have wide application in IR region. A major concern for IR applications using LCs is the inherent absorption loss due to the existence of molecular vibration bands. In the mid-wave infrared (MWIR) region (3-5 μm), several molecular vibration bands exist, such as CH, CH₂, CH₃, CN, and NCS stretching. The CH, CH₂, and CH₃ absorption bands overlap closely and are centered at $\sim 3.4 \mu\text{m}$ with a bandwidth from 3.2-3.7 μm . On the other hand, the strong cyano (CN) absorption peak occurs at $\sim 4.48 \mu\text{m}$ and isothiocyanato (NCS) polar group has a broad and strong absorption in the 4.5-5.2 μm spectral regions.

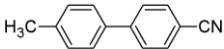
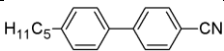
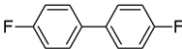
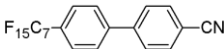
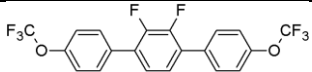
The molecular vibration frequency (ω) depends on the spring constant (κ) and reduced mass (μ) of the diatomic group as:

$$\omega = \sqrt{\kappa / \mu}. \quad (30)$$

As the reduced mass increases, the vibration frequency decreases, i.e., the absorption band shifts toward a longer wavelength.¹⁷¹ To prove this concept, a perdeuterated ($\sim 95\%$ ²H) 5CB (4'-pentylbiphenyl-4-carbonitrile) compound, designated as D5CB, has been developed.^{172,173} The carbon-deuteron (CD) absorption peak shifted from 3.5 μm to 4.6 μm . In both near IR (0.75-3 μm) and long wavelength IR (8-12 μm) regions, D5CB has a much cleaner absorption spectrum and lower absorption coefficient than 5CB in the off-resonance region while other physical properties, such as phase transition temperatures and birefringence remain more or less unchanged. To ensure a low absorption in the desired MWIR window, we need to shift the

absorption band further out to longer wavelength IR region. To do so, we need to replace hydrogen with a still heavier atom, such as fluorine.

Table 8. Chemical structures and properties of the compounds studied. Cr stands for crystalline, N for nematic, and I for isotropic phase.

Compound #.	Chemical Structure	Abbreviation	PTT (°C)	ΔH (cal/mol)
1		1CB	Cr109N(45)I ^a	5400
2		5CB	Cr24N35.3I	4100
3		FB	Cr88I	2198 ^b
4		F7CB	Cr120.4I	10719
5		FT	C85.8N87.6I	4921

^a() indicates a monotropic phase. ^bEnthalpy of sublimation

Fluorinated liquid crystals have often been used in active matrix liquid crystal displays, and their properties have been reviewed elsewhere.^{67,174} In these compounds the fluoro substitutions are installed mainly in the phenyl ring in order to create dielectric anisotropy ($\Delta\epsilon$), while keeping the alkyl chain untouched. As a result, the strong CH absorption bands still exist, although they are not important for display applications. Very little research has been done to tailor fluorinated liquid crystals for reduction of MWIR absorption as the molecular design strategies for these two applications (visible wavelength displays and IR phase modulators) are quite different. For MWIR applications of a liquid crystal material, besides a wide nematic temperature range, high birefringence (Δn), low viscosity, and a modest $\Delta\epsilon$, low absorption in MWIR is required, which would result in a different molecular structure and in turn affect the physical properties. Therefore, a good balance between physical properties and MWIR loss should be considered.

In this paper, we outline our molecular design strategy and demonstrate a first partially fluorinated LC compound to clean up the MWIR absorption bands, while exhibiting a nematic phase (although only about 2°C), high birefringence ($\Delta n \sim 0.2$), a low visco-elastic coefficient, and a modest dielectric anisotropy ($\Delta \epsilon = -2.7$).

4.1 Molecular Design Strategy

Substitution of all the CH bonds in the alkyl chain and phenyl rings with CF might appear to be a straightforward approach to suppress MWIR absorption. However, these completely fluorinated compounds themselves exhibit some undesirable properties, such as high melting temperature (T_m), large heat fusion enthalpy (ΔH), and no liquid crystalline phase (or, at least, a propensity to form smectic phases). In order for a compound to exhibit a nematic phase, the compound ought to have certain flexibility and aspect ratio. Based on the IR absorption spectra, the CH bonds in a phenyl ring have a much weaker and narrower absorption than those found for CH bonds in flexible alkyl chains. To further validate this concept, Compounds 1, 2, 3 and 4 (listed in Table 8)¹⁷⁵ were prepared, dissolved in CCl_4 at a concentration of $\sim 5 \times 10^{-5}$ mol/ml and then filled in a NaCl IR cell with cell gap (0.5 mm). The measurement of MWIR transmission spectra were carried out on a Perkin Elmer Spectrum One FT-IR Spectrometer. The transmission spectra of the compounds were normalized to that of CCl_4 . As illustrated in Figure 40, both 1CB (4'-methylbiphenyl-4-carbonitrile) and 5CB exhibit a much broader and stronger absorption near $\lambda = 3.4 \mu\text{m}$ than FB (#3, 4,4'-difluorobiphenyl) does. The reference compound FB has no alkyl chain, but has two phenyl rings. It does not have mesogenic phase. This comparison is to confirm that indeed the CH bonds in the alkyl chain make a stronger absorption near $\lambda = 3.4 \mu\text{m}$

than the CH bonds in the phenyl rings. The 5CB has a longer alkyl chain with more CH bonds in -CH₂- and -CH₃ structures. Therefore, its absorption near 3.4 μm is much stronger. The absorption from C≡N (4.48μm) in 1CB and 5CB is almost the same because of similar concentration.

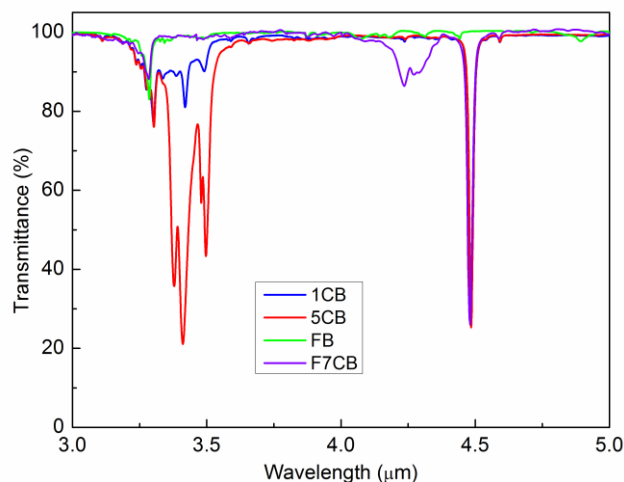


Figure 40. Measured transmission spectra of 5CB (Red), 1CB (Blue), FB (Green) and F7CB (Violet).

Next, we synthesized a compound (#4, F7CB) with all the hydrogen atoms in the alkyl chain of 7CB (4'-heptylbiphenyl-4-carbonitrile) replaced with fluorine. As expected, and like 5CB and 1CB, the F7CB has a strong absorption peak at 4.48μm due to C≡N stretching, but its absorption at ~3.4μm is significantly reduced since all the C-H bonds in the alkyl chain have been replaced by C-F bonds. It is known that -CF₂- and -CF₃ have a broad and strong absorption in 7.1-9.5μm,¹⁷⁶ while the relatively weak absorption at ~4.25μm is an overtone of the strong C-F vibration centered near 8.5 μm. This overtone can be further reduced by decreasing the number of CF groups, i.e., employing a shorter fluorinated alkyl chain. The residual absorption of C-H bonds in the phenyl rings, as in F7CB, is much more tolerable. The phase transition properties

and ΔH of F7CB were measured using Differential Scanning Calorimetry (DSC, TA Instruments Q2000). With a long perfluorinated alkyl chain, F7CB does not exhibit any mesogenic phase. Rather, its melting point is $\sim 120^\circ\text{C}$ (c.f. 30°C for 7CB) and its ΔH is increased dramatically so that its solubility in an LC host is limited to <5 wt%.

Therefore, a practical solution is to substitute only the CH bonds in the alkyl chain while keeping the core structure unaltered. Moreover, the fluorinated alkyl chain should not be too long, otherwise, the LC phase would be suppressed and the C-F vibrational overtone grows. Meanwhile, two or three phenyl rings are needed to ensure a high birefringence. To realize a useful electro-optic effect, the compounds should be polar with a modest $\Delta\epsilon$, either positive or negative. To replace CN, we could choose $-\text{F}$, $-\text{CF}_3$, or $-\text{OCF}_3$ as polar groups. Based on these guidelines, we synthesized a new fluorinated terphenyl compound (#5, abbreviated as FT) and evaluated its properties.

4.2 Absorption and Physical Properties

As shown in Figure 41, the absorption of FT at $\sim 3.4\mu\text{m}$ is significantly reduced, compared to that of 5CB. Only small absorption exists due to the residual CH bonds in the phenyl rings. The fairly weak absorption at $\sim 4\mu\text{m}$ is the overtone of C-F stretching vibration. Overall, from $3\mu\text{m}$ to $5\mu\text{m}$, the absorption is quite clean. Note that the absorption peak due to the C-O single bond stretching vibration is shifted to the wavelength longer than $7.5\mu\text{m}$,¹⁷⁶ which is out of MWIR window. For MWIR application, glass substrate and indium-tin-oxide (ITO) electrode are not quite transparent. Instead, we can use germanium substrate due to its low loss and high electrical

conductivity.^{177,178} Besides, the LC alignment layer is usually very thin (~80 nm) which will not cause much absorption.

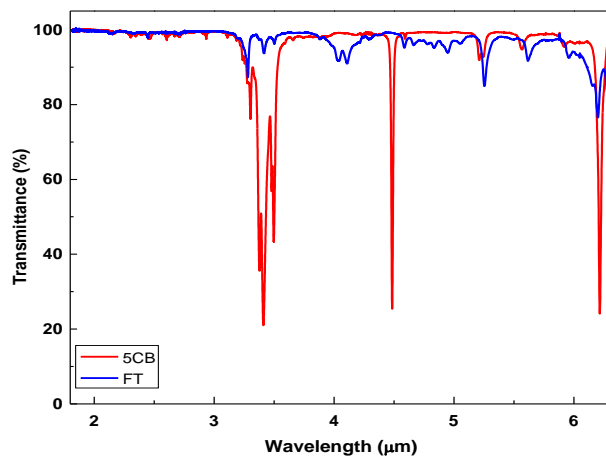


Figure 41. Measured transmission spectra of 5CB (red line) and FT (blue line) in MWIR region

We also compared the absorption spectrum of FT with 5CB in the 0.6-3.2 μm range. Since the absorption is relatively small in this spectral region, a 2-mm-thick quartz cell was used and the concentrations for both compounds were increased to 5×10^{-4} mol/ml in CCl_4 . A Cary UV/Vis/NIR spectrophotometer was employed to record the near IR transmission spectra. In Figure 42, the blue and red lines represent the transmission spectra for FT and 5CB, respectively. The overall outcome is that some overtone absorption bands appear in this region, but FT exhibits a much higher transmittance than 5CB. In the spectral range of 2.2-3.0 μm , where the absorption is due to the combination of C-H stretching, FT shows much weaker absorption than 5CB does. In addition, the $\lambda \sim 1.7$ μm band resulting from the second harmonic of the 3.4- μm CH band becomes narrower for FT.

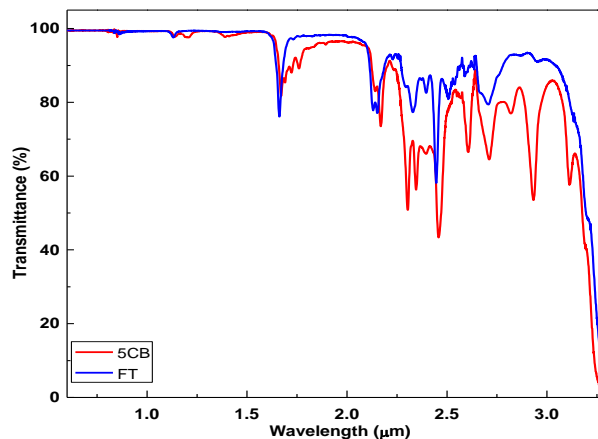


Figure 42. Measured transmission spectra of 5CB (red line) and FT (blue line) in near IR region.

For MWIR applications, in addition to low absorption we also require the compound to have a nematic phase, high birefringence, low viscosity, and a large dipole moment. Therefore, we also characterized the physical properties of FT. From DSC measurements, FT exhibits a narrow ($\sim 2^\circ\text{C}$) but enantiotropic nematic phase from 85.8°C to 87.6°C . To measure the physical properties, we doped FT into a commercial negative LC host, MLC-6882 (Merck) at 10 wt% and 15 wt% ratios. The Δn of the mixture was measured through phase retardation of a VA LC cell (cell gap $d \sim 9 \mu\text{m}$) sandwiched between two crossed polarizers. For the LC host cell with $d = 9.29 \mu\text{m}$ and $\delta = 2.77\pi$, we obtained $\Delta n = 0.094$ from Equation (7). Similarly, for the 10 wt% and 15 wt% doped samples, we obtained $\Delta n = 0.105$ and 0.111 , respectively. The birefringence of FT was extrapolated by weight ratio and the resulting $\Delta n \sim 0.205$ ($\lambda = 632.8 \text{ nm}$). According to the birefringence dispersion of liquid crystals, Δn decreases with wavelength and gradually saturates in the near IR region. In the MWIR region, the estimated Δn is ~ 0.18 . High Δn enables a thin cell gap to be used for achieving a certain phase change, say 2π , which in turn helps to reduce response time and absorption loss. For example, at the edge of C-H absorption band, say

$\lambda=3.5\mu\text{m}$, the estimated transmission of 5CB with 2π phase retardation is only 6.2%, but it is increased to 93% for the FT LC with the same phase retardation.

The $\Delta\varepsilon$ was determined through the capacitance measurements of parallel- and perpendicular-aligned LC cells.⁴⁹ An HP-4274 multi-frequency LCR meter was employed for the capacitance measurements. MLC-6882 has a modest dielectric anisotropy $\Delta\varepsilon= -2.56$ and a fairly low rotational viscosity ($\gamma_1\sim 70$ mPa·s) at room temperature (24°C). The extrapolated dielectric anisotropy of FT is $\Delta\varepsilon= -2.71$.

We measured the decay time constant τ_0 and calculated the γ_1/k_{33} of MLC-6682 and the 10 wt% and 15 wt% doped mixtures. Our results show that the τ_0 of the two doped samples decreases from 59.0 ms to 58.2 ms and 55.3 ms, and accordingly the calculated γ_1/k_{33} was slightly reduced from 6.75 ms/ μm^2 to 6.56 and 6.41 ms/ μm^2 , respectively. Although γ_1/K_{33} cannot be linearly extrapolated, the relative low γ_1/K_{33} of the doped mixtures indicates that FT has a somewhat lower γ_1/k_{33} than MLC-6682. Such a low viscosity originates from the $-\text{OCF}_3$ group.^{67,179-181}

The nematic range of our fluorinated terphenyl is only 2°C. This sample serves as an important first example for proving our design concepts, but its nematic range is too narrow for practical applications. To widen the nematic range, several compounds have to be developed in order to formulate eutectic mixtures. As illustrated in Figure 43, the general molecular structure shows some compounds which not only satisfy the low-loss criterion but also have potential for wider temperature range. However, the phase transition temperature of a compound is difficult to predict before it is synthesized.

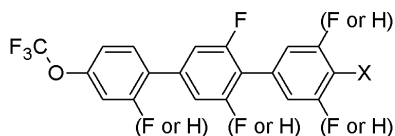


Figure 43. Molecular structure with potentially wider nematic range for forming eutectic mixtures (X=F or OCF₃).

We have demonstrated a fluorinated terphenyl liquid crystal with low absorption in both MWIR and near IR regions. Although this LC compound has a negative $\Delta\epsilon$ and narrow nematic phase range, it possesses some attractive properties, such as low absorption loss in MWIR, high birefringence, moderate $\Delta\epsilon$, and low visco-elastic coefficient. With additional molecular design and synthesis, e.g., substituting fluoro groups in different positions of the phenyl rings or employing $-\text{OCF}_3$ at one phenyl ring terminal as a polar group, a positive $\Delta\epsilon$ and potentially wider nematic range will result. In order to further widen the nematic range for room temperature operation, several homologues are needed to form eutectic mixtures. For eutectic mixture formulation, we have proposed some modified molecular structures. The FT compound proposed in this paper serves as an important first example for future development of low-loss MWIR liquid crystals, which would further enable the application of LCs for amplitude and/or phase modulation in MWIR region.

CHAPTER FIVE: SUMMARY

For nematic LCs, different methods for improving response time have been discussed, including thin cell gap, temperature effect, and overdrive/undershoot driving scheme. Experimentally, we have developed several high birefringence positive and negative $\Delta\epsilon$ liquid crystals to enable thin-cell-gap approach for achieving fast response time while keeping sufficient phase retardation. These LCs have relatively large dielectric anisotropy and high resistivity, which could be attractive candidates for active matrix LCDs. High performance negative $\Delta\epsilon$ LCs have been developed for FFS and VA display applications. With our UCF-N2, n-FFS shows superior performance such as high transmittance, single gamma curve, cell gap insensitivity, and negligible flexoelectric effect, comparable response time and driving voltage, to the presently employed p-FFS. Using our UCF-N3 for VA LCOS, we have demonstrated a submillisecond gray-to-gray response time for color sequential projection displays. Our low viscosity UCF-N2 can also be used for MVA LCD TVs if the cell gap can be reduced to 2.5 μm . As compared to the 3- μm cell gap currently employed, the response time can be reduced by ~40%.

To further reduce response time to submillisecond to enable color sequential displays, polymer-stabilized BPLC is a promising candidate. We have briefly discussed the material system and electro-optic properties of polymer-stabilized blue phase liquid crystals, including blue phase appearance, electric field effects and diluter effects. The compositions of PS-BPLC, including nematic LC host, chiral dopant, and polymer network, are discussed. Each component plays an essential role in affecting the stability and electro-optic properties of PS-BPLC. Because

of the collective effect of strong polymer network, short pitch length and temperature effect, a PS-BPLC with microsecond response time has been demonstrated. This response is 1-2 orders of magnitude faster than that of a typical BPLC device, which set a new record for BPLC response time. With rapid advances in PS-BPLC materials and device structures, we have reduced the driving voltage to below 10 V, while maintaining submillisecond response time, high contrast ratio, and negligible hysteresis. This paves the way for future widespread applications of PS-BPLCs. We have also demonstrated an electric field-induced mono-domain blue phase and its potential application for reflective displays. The reflection spectra for red, green and blue cells are also investigated. The bandwidth is fairly narrow so the color looks saturated and vivid. The reflectance gradually decreases with the increasing operation voltage, and analogous grayscales can be achieved. With analog grayscales and submillisecond response time, videos can be displayed using this reflective PSBP. Moreover, the electric-field-induced monodomain blue phase selectively only reflects RCP light when the employed chiral dopant is right-handed, and the reflected light is almost circularly polarized.

Besides application in visible spectral range, we have demonstrated a fluorinated terphenyl liquid crystal with low absorption in both MWIR and near IR regions. Some modified molecular structures have been proposed for eutectic mixture formulation in order to expand temperature range. This fluorinated terphenyl compound serves as an important first example for future development of low-loss MWIR liquid crystals, which would further enable the application of LCs for amplitude and/or phase modulation in MWIR region.

CHAPTER SIX: MAJOR ACCOMPLISHMENTS

The major accomplishments in this dissertation are summarized as follows:

- 1) I have experimentally demonstrated a microsecond-response PS-BPLC using a vertical-field-switching cell. This response time is 1-2 orders of magnitude faster than that of a typical BPLC device, which set a new record for BPLC response time.
- 2) Demonstrated a PS-BPLC with on-state voltage of 8.4V, hysteresis-free and submillisecond response time. These results imply that the dawn of BPLC era for high speed display and photonic devices has finally arrived.
- 3) An electric field-induced monodomain BPLC has been reported with high reflectance, narrow reflection band, natural gray levels and submillisecond response. Thus crisp video with vivid color can be displayed without image blur.
- 4) Diluter effects on PS-BPLC have been investigated and we found some diluters could help decrease the response time by 2X-3X while keeping the voltage unchanged. An increased relaxation frequency is observed. Moreover, due to viscosity reduction, one-drop-fill process of LCD panels becomes easier. This investigation provides valuable guidelines for scientific studies as well as for manufacturing processes.
- 5) Demonstrated a superior performance fringe-field-switching mode using negative dielectric anisotropy LCs (n-FFS), which shows high transmittance, single gamma curve, and cell gap insensitivity. It has potential to replace the current technology for mobile LCDs.
- 6) Demonstrated a fluorinated terphenyl liquid crystal with low absorption in both MWIR

and near IR regions. This compound serves as an important first example for future development of low-loss MWIR liquid crystals, which would further enable the application of LCs for amplitude and/or phase modulation in MWIR region.

**APPENDIX:
LIST OF PUBLICATIONS**

JOURNAL PUBLICATIONS

1. F. Peng, Y. Chen, S.-T. Wu, S. Tripathi, and R. J. Twieg “Low loss liquid crystals for infrared applications,” *Liq. Cryst.* 41, xxx (Accepted, 2014). DOI: 10.1080/02678292.2014.932452
2. D. Xu, J. Yan, J. Yuan, F. Peng, Y. Chen, and S.-T. Wu, “Electro-optic response of polymer-stabilized blue phase liquid crystals,” *Appl. Phys. Lett.* **105**, 011119 (2014).
3. **(Review paper)** Y. Chen and S.-T. Wu, “Recent advances in polymer-stabilized blue phase liquid crystal materials and devices,” *J. Appl. Polym. Sci.*, **131**(13), 6333-6342 (2014).
4. F. Peng, Y. Chen, J. Yuan, H. Chen, S.-T. Wu, and Y. Haseba, “Low temperature and high frequency effects on polymer-stabilized blue phase liquid crystals with large dielectric anisotropy,” *J. Mater. Chem. C*, **2**, 3597-3601 (2014).
5. Z. Luo, Y. Chen, and S.-T. Wu, “Wide color gamut LCD with a quantum dot backlight,” *Opt. Express* **21**, 26269-26284 (2013).
6. D. Xu, Y. Chen, Y. Liu, and S.-T. Wu, “Refraction effect in an in-plane-switching blue phase liquid crystal cell,” *Opt. Express* **21**, 24721-24735 (2013).
7. J. Yan, Y. Chen, D. Xu, and S.-T. Wu, “Angular dependent reflections of a monodomain blue phase liquid crystal,” *J. Appl. Phys.* **114**, 113106 (2013).
8. **(Review paper)** Y. Chen, F. Peng, T. Yamaguchi, X. Song, and S.-T. Wu, “High performance negative dielectric anisotropy liquid crystals for display applications,” *Crystals* **3**, 483-503 (2013).

9. Y. Chen, J. Yan, M. Schadt, S. H. Liu, K. L. Cheng, J. W. Shiu, and S.-T. Wu, "Diluter effects on polymer-stabilized blue phase liquid crystals," *J. Display Technol.* **9**, 592-597 (2013).
10. Y. Chen and S.-T. Wu, "Electric field-induced monodomain blue-phase liquid crystals," *Appl. Phys. Lett.* **102**, 171110 (2013).
11. Y. Chen, D. Xu, S.-T. Wu, S. Yamamoto, and Y. Haseba, "A low voltage and submillisecond-response polymer-stabilized blue phase liquid crystal," *Appl. Phys. Lett.* **102**, 141116 (2013).
12. Y. Chen, F. Peng, and S.-T. Wu, "Submillisecond-response vertically-aligned liquid crystal for color-sequential projection displays," *J. Display Technol.* **9**, 78 (2013).
13. Y. Chen, Z. Luo, F. Peng, and S.-T. Wu, "Fringe-field switching with a negative dielectric anisotropy liquid crystal," *J. Display Technol.*, **9**, 74 (2013)
14. C. D. Tu, C. L. Lin, J. Yan, Y. Chen, and S.-T. Wu, "Driving scheme using bootstrapping method for blue-phase LCDs," *J. Display Technol.* **9**, 3 (2013).
15. J. Yan, Y. Chen, S.-T. Wu, and X. Song, "Figure of merit of polymer-stabilized blue phase liquid crystals," *J. Display Technol.* **9**, 24 (2013).
16. J. Sun, Y. Chen, and S.-T. Wu, "Submillisecond-response and scattering-free infrared liquid crystal phase modulators," *Opt. Express* **20**, 20124-20129 (2012).
17. Y. Li, Y. Chen, J. Yan, Y. Liu, J. P. Cui, Q. H. Wang, and S.-T. Wu, "Polymer-stabilized blue phase liquid crystal with a negative Kerr constant," *Opt. Mater. Express* **2**, 1135-1140 (2012).

18. J. Yan, Y. Chen, S.-T. Wu, S. H. Liu, K. L. Cheng, and J. W. Shiu, "Dynamic response of a polymer-stabilized blue-phase liquid crystal," *J. Appl. Phys.* **111**, 063103 (2012).
19. J. Sun, R. A. Ramsey, Y. Chen, and S.-T. Wu, "Submillisecond-response sheared polymer network liquid crystals for display applications," *J. Display Technol.* **8**, 87-90 (2012).
20. Y. Liu, H. Ren, S. Xu, Y. Chen, L. Rao, T. Ishinabe, and S.-T. Wu, "Adaptive focus integral image system design based on fast-response liquid crystal microlens," *J. Display Technol.* **7**, 674-678 (2011).
21. Y. Chen, J. Yan, J. Sun, S.-T. Wu, X. Liang, S. H. Liu, P. J. Hsieh, K. L. Cheng, and J. W. Shiu, "A microsecond- response polymer-stabilized blue phase liquid crystal," *Appl. Phys. Lett.* **99**, 201105 (2011).
22. Y. Li, Y. Chen, J. Sun, S.-T. Wu, S. H. Liu, P. J. Hsieh, K. L. Cheng, and J. W. Shiu, "Dielectric dispersion on the Kerr constant of blue phase liquid crystals," *Appl. Phys. Lett.* **99**, 181126 (2011).
23. Y. Chen, J. Sun, H. Xianyu, S.-T. Wu, X. Liang, and H. Tang, "High birefringence fluoro-terphenyls for thin-cell-gap TFT-LCDs," *J. Display Technol.* **7**, 478-481 (2011).
24. J. Sun, H. Xianyu, Y. Chen, and S.-T. Wu, "Submillisecond-response polymer network liquid crystal phase modulators at 1.06-mm wavelength," *Appl. Phys. Lett.* **99**, 021106 (2011).
25. Y. Chen, H. Xianyu, J. Sun, P. Kula, R. Dabrowski, S. Tripathi, R. J. Twieg, and S.-T. Wu, "Low absorption liquid crystals for mid-wave infrared applications," *Opt.*

Express **19**, 10843-10848 (2011).

26. Q. Yang, X. Jiang, X. Guo, Y. Chen, and L. Tong, “Hybrid structure laser based on semiconductor nanowires and a silica microfiber knot cavity”, Appl. Phys. Lett. **94**, 101108 (2009).
27. Y. Chen, Z. Ma, Q. Yang, and L. Tong, “Compact optical short-pass filters based on microfibers”, Optics Lett. **33**, 2565 (2008).
28. X. Jiang, Y. Chen, G. Vienne, and L. Tong, “All-fiber add-drop filters based on microfiber knot resonators”, Opt. Lett. **32**, 1710 (2007).

BOOK CHAPTER

29. Y. Chen, J. Sun and S.-T. Wu, “Submillisecond response liquid crystals for display and photonics devices”, in book “Progress in Liquid Crystal (LC) Science and Technology”, (World Scientific, 2013)

CONFERENCE PROCEEDINGS

30. **(Distinguished student paper award)** Y. Chen, J. Yan, M. Schadt, S. H. Liu, K. L. Cheng, J. W. Shiu, and S.-T. Wu, “Diluter effects on large dielectric anisotropy blue phase liquid crystals”, SID Int. Symp. Digest Tech. Papers, **45**, 1392 (2014, San Diego, CA)
31. **(Distinguished student paper award)** D. Xu, Y. Chen, Y. Liu, and S.-T. Wu, “Low-voltage and high-transmittance blue-phase liquid crystal displays,” SID Int. Symp. Digest Tech. Papers, **45**, 168 (2014, San Diego, CA)
32. **(Distinguished student paper award)** Z. Luo, Y. Chen, and S.-T. Wu, “Quantum Dots-

- enhanced LCD color and optical efficiency,” SID Int. Symp. Digest Tech. Papers, **45**, 245 (2014, San Diego, CA)
33. F. Peng, Y. Chen, J. Yuan, H. Chen and S.-T. Wu, “Low Temperature and High Frequency Effects on Blue Phase Liquid Crystals,” SID Symp. Digest Papers **45**, 164-167 (2014, San Diego, CA)
34. **(Invited paper)** Y. Chen and S.-T. Wu, “The outlook for blue-phase LCDs”, Proc. SPIE **9005**, 900508 1-7 (2014, San Francisco, CA)
35. **(Invited paper)** Z. Luo, S. Xu, Y. Chen, Y. Liu and S.-T. Wu, “Prospects of quantum dots-based liquid crystal displays,” Proc. SPIE **9005**, 90050G 1-7 (2014, San Francisco, CA)
36. Y. Chen, F. Peng, T. Yamaguchi, X. Song and S.-T. Wu, “High Birefringence Negative Dielectric Anisotropy Liquid Crystals for Display Applications”, IMID 2013, Daegu, Korea
37. **(Distinguished student paper award)** Y. Chen, Z. Luo, F. Peng, and S.-T. Wu, “High performance fringe-field switching with a negative dielectric anisotropy liquid crystal”, SID Int. Symp. Digest Tech. Papers, **44** (1), 334 (2013, Vancouver, Canada).
38. Y. Chen, F. Peng, and S.-T. Wu, “A vertically-aligned LCOS with submillisecond response time”, SID Int. Symp. Digest Tech. Papers, **44** (1), 898 (2013, Vancouver, Canada).
39. C. L. Lin, M. H. Cheng, C. D. Tu, C. C. Hung, P. C. Lai, J. Yan, Y. Chen and S.-T. Wu, “Pixel circuit with bootstrapping structure for blue phase liquid crystal display”, SID Int.

- Symp. Digest Tech. Papers, **44** (1), 306 (2013, Vancouver, Canada).
40. **(Invited talk)** Y. Chen, Z. Luo, F. Peng, and S.-T. Wu, “Next generation mobile LCDs”, 2nd Symposium on Liquid Crystal Photonics (2013, Chengdu, China).
41. Y. Chen, J. Yan, J. Sun, S.-T. Wu, X. Liang, S. H. Liu, P. J. Hsieh K. L. Cheng, and J. W. Shiu, “A microsecond-response blue phase liquid crystal device”, SID Int. Symp. Digest Tech. Papers **43**, 98 (2012, Boston, MA).
42. Y. Li, Y. Chen, J. Sun, S. -T Wu, S. H. Liu, P. J. Hsieh, K. L. Cheng, J. W. Shiu, S. I. Yamamoto, and Y. Haseba, “Frequency effects on polymer-stabilized blue-phase liquid crystals”, SID Int. Symp. Digest Tech. Papers **43**, 22 (2012, Boston, MA).
43. J. Yan, Y. Chen, S.-T. Wu, S. H. Liu, K. L. Cheng, and J. W. Shiu, “Dynamic decay processes of a polymer-stabilized blue-phase liquid crystal”, SID Int. Symp. Digest Tech. Papers **43**, 102 (2012, Boston, MA).
44. J. Sun, Y. Chen, S.-T. Wu and R. A. Ramsey, “Submillisecond response sheared polymer network liquid crystals for 3D displays”, SID Int. Symp. Digest Tech. Papers **42**, 82 (2011, Los Angeles, CA).
45. Y. Chen, H. Xianyu, J. Sun, and S.-T. Wu, “High-birefringence fluoro-terphenyls for thin-cell-gap LCDs,” SID Int. Symp. Digest Tech. Papers **42**, 1681 (2011, Los Angeles, CA).

MAGAZINE ARTICLES

46. Z. Luo, Y. Chen and S.-T. Wu, “Quantum dots: a new era for liquid crystal display backlight,” SPIE Newsroom (March 2014).

LIST OF REFERENCES

- [1] Z. Luo, Y. Chen, and S. T. Wu, *Opt. Express* **21** (22), 26269 (2013).
- [2] J. Beeckman, K. Neyts, and P. J. M. Vanbrabant, *Opt. Eng.* **50** (8), 081202 (2011).
- [3] S. H. Hong, I. C. Park, H. Y. Kim, and S. H. Lee, *Jpn. J. Appl. Phys.* **39** (6A), L527 (2000).
- [4] S. H. Lee, S. L. Lee, and H. Y. Kim, *Appl. Phys. Lett.* **73** (20), 2881 (1998).
- [5] Y. Chen, Z. Luo, F. Peng, and S. T. Wu, *J. Display Technol.* **9** (2), 74 (2013).
- [6] M. Oh-e and K. Kondo, *Appl. Phys. Lett.* **67** (26), 3895 (1995).
- [7] Z. Ge, X. Zhu, T. X. Wu, and S. T. Wu, *J. Display Technol.* **2** (2), 114 (2006).
- [8] M. F. Schiekel and K. Fahrenschon, *Appl. Phys. Lett.* **19** (10), 391 (1971).
- [9] F. J. Kahn, *Appl. Phys. Lett.* **20** (5), 199 (1972).
- [10] K. Ohmuro, S. Kataoka, T. Sasaki, and Y. Koike, *SID Symp. Dig. Tech.* **28**, 845 (1997).
- [11] A. Takeda, S. Kataoka, T. Sasaki, H. Chida, H. Tsuda, K. Ohmuro, T. Sasabayashi, Y. Koike, and K. Okamoto, *SID Symp. Dig. Tech.* **29**, 1077 (1998).
- [12] P. Bos, T. Buzak, and R. Vatne, *Proc. SID* **26** (2), 157 (1985).
- [13] M. Kobayashi, A. Yoshida, and Y. Yoshida, *SID Int. Symp. Digest Tech.* **41**, 1434 (2010).
- [14] S. Gauza, X. Zhu, W. Piecek, R. Dabrowski, and S. T. Wu, *J. Display Technol.* **3** (3), 250 (2007).
- [15] F. Yamada, H. Nakamura, Y. Sakaguchi, and Y. Taira, *SID Int. Symp. Digest Tech.* **31**, 1180 (2000).

- [16] H. Kikuchi, M. Yokota, Y. Hisakado, H. Yang, and T. Kajiyama, *Nat. Mater.* **1** (1), 64 (2002).
- [17] Y. Hisakado, H. Kikuchi, T. Nagamura, and T. Kajiyama, *Adv. Mater.* **17** (1), 96 (2005).
- [18] S. W. Choi, S. Yamamoto, Y. Haseba, H. Higuchi, and H. Kikuchi, *Appl. Phys. Lett.* **92** (4), 043119 (2008).
- [19] Z. Ge, S. Gauza, M. Jiao, H. Xianyu, and S. T. Wu, *Appl. Phys. Lett.* **94** (10), 101104 (2009).
- [20] J. Yan, L. Rao, M. Jiao, Y. Li, H. C. Cheng, and S. T. Wu, *J. Mater. Chem.* **21** (22), 7870 (2011).
- [21] Y. Chen and S. T. Wu, *J. Appl. Poly. Sci.* **131** (13), 40556 (2014).
- [22] K. M. Chen, S. Gauza, H. Q. Xianyu, and S. T. Wu, *J. Display Technol.* **6** (2), 49 (2010).
- [23] Y. Chen, J. Yan, J. Sun, S. T. Wu, X. Liang, S. H. Liu, P. J. Hsieh, K. L. Cheng, and J. W. Shiu, *Appl. Phys. Lett.* **99** (20), 201105 (2011).
- [24] J. Yan, Y. Li, and S. T. Wu, *Opt. Lett.* **36** (8), 1404 (2011).
- [25] Y. Li and S. T. Wu, *Opt. Express* **19** (9), 8045 (2011).
- [26] Y. H. Lin, H. S. Chen, H. C. Lin, Y. S. Tsou, H. K. Hsu, and W. Y. Li, *Appl. Phys. Lett.* **96** (11), 113505 (2010).
- [27] H. J. Coles and S. Morris, *Nat. Photonics* **4** (10), 676 (2010).
- [28] S. T. Wu, U. Efron, and L. D. Hess, *Appl. Phys. Lett.* **44** (11), 1033 (1984).
- [29] S. T. Wu, *Phys. Rev. A.* **33** (2), 1270 (1986).
- [30] U. Efron, S. T. Wu, J. Grinberg, and L. D. Hess, *Opt. Eng.* **24** (1), 111 (1985).

- [31] P. F. McManamon, T. A. Dorschner, D. L. Corkum, L. J. Friedman, D. S. Hobbs, M. Holz, S. Liberman, H. Q. Nguyen, D. P. Resler, R. C. Sharp, and E. A. Watson, Proc. of the IEEE **84** (2), 268 (1996).
- [32] J. W. McCargar, R. Ondris-Crawford, and J. L. West, J. Electronic. Img. **1** (1), 22 (1992).
- [33] L. Scolari, L. Wei, S. Gauza, S. T. Wu, and A. Bjarklev, Opt. Rev. **18** (1), 114 (2011).
- [34] S. T. Wu, J. Appl. Phys. **84** (8), 4462 (1998).
- [35] I. C. Khoo and S. T. Wu, *Optics and Nonlinear Optics of Liquid Crystals*. (World Scientific, Singapore, 1993).
- [36] D. K. Yang and S. T. Wu, *Fundamentals of Liquid Crystal Devices*. (Wiley, New York, 2006).
- [37] S. T. Wu, Appl. Opt. **28** (1), 48 (1989).
- [38] S. T. Wu and C. S. Wu, Appl. Phys. Lett. **53** (19), 1794 (1988).
- [39] S. T. Wu, Appl. Phys. Lett. **57** (10), 986 (1990).
- [40] D. Xu, L. Rao, C. D. Tu, and S. T. Wu, J. Display Technol. **9** (2), 67 (2013).
- [41] S. T. Wu, J. D. Margerum, H. B. Meng, L. R. Dalton, C. S. Hsu, and S. H. Lung, Appl. Phys. Lett. **61** (6), 630 (1992).
- [42] S. T. Wu, C. S. Hsu, and K. F. Shyu, Appl. Phys. Lett. **74** (3), 344 (1999).
- [43] C. Sekine, K. Fujisawa, K. Iwakura, and M. Minai, Mol. Cryst. Liq. Cryst. **364**, 711 (2001).

- [44] Y. Chen, J. Sun, H. Xianyu, S. T. Wu, X. Liang, and H. Tang, *J. Display Technol.* **7** (9), 478 (2011).
- [45] Y. Chen, J. Sun, and S. T. Wu, in *Progress in Liquid Crystal (LC) Science and Technology*, edited by H. S. Kwok, S. Naemura, and H. L. Ong (World Scientific, 2013).
- [46] I. K. Huh and Y. B. Kim, *Jpn. J. Appl. Phys.* **41** (11A), 6466 (2002).
- [47] I. K. Huh and Y. B. Kim, *Jpn. J. Appl. Phys.* **41** (11A), 6484 (2002).
- [48] J. Li and S. T. Wu, *J. Appl. Phys.* **95** (3), 896 (2004).
- [49] S. T. Wu, U. Efron, and L. D. Hess, *Appl. Opt.* **23** (21), 3911 (1984).
- [50] I. Haller, *Prog. Solid State Chem.* **10**, 103 (1975).
- [51] M. Schadt and W. Helfrich, *Appl. Phys. Lett.* **18** (4), 127 (1971).
- [52] C. H. Gooch and H. A. Tarry, *J. Phys. D: Appl. Phys.* **8**, 1575 (1975).
- [53] Z. Ge and S. T. Wu, *Transflective Liquid Crystal Displays*. (Wiley, United Kingdom, 2010).
- [54] S. T. Wu and C. S. Wu, *Phys. Rev. A.* **42** (4), 2219 (1990).
- [55] P. G. DeGennes, *The Physics of Liquid Crystals*. (Clarendon, Oxford, 1974).
- [56] V. V. Belyayev, S. A. Ivanov, and M. F. Grebenkin, *Kristallografiya* **30** (6), 1160 (1985).
- [57] A. Saupe, *Z. Naturforsch. Teil A* **15**, 810 (1960).
- [58] M. J. Bradshaw, D. G. McDonnell, and E. P. Raynes, *Mol. Cryst. Liq. Cryst.* **70** (1-4), 1567 (1981).
- [59] S. T. Wu, A. M. Lackner, and U. Efron, *Appl. Opt.* **26** (16), 3441 (1987).

- [60] S. T. Wu and D. K. Yang, *Reflective Liquid Crystal Displays*. (Wiley, New York, 2001).
- [61] P. Kirsch, V. Reiffenrath, and M. Bremer, *Synlett* (4), 389 (1999).
- [62] P. Kirsch, M. Heckmeier, and K. Tarumi, *Liq. Cryst.* **26** (3), 449 (1999).
- [63] M. Klasen, M. Bremer, and K. Tarumi, *Jpn. J. Appl. Phys.* **39** (11B), L1180 (2000).
- [64] P. Kirsch and K. Tarumi, *Angew. Chem. Int. Ed.* **37** (4), 484 (1998).
- [65] M. Hird, J. W. Goodby, and K. J. Toyne, presented at the Proc. SPIE, 2000.
- [66] M. Ogata, K. Ukai, and T. Kawai, *J. Display Technol.* **1** (2), 314 (2005).
- [67] M. Hird, *Chem. Soc. Rev.* **36** (12), 2070 (2007).
- [68] G. W. Gray, M. Hird, and K. J. Toyne, *Mol. Cryst. Liq. Cryst.* **204**, 43 (1991).
- [69] S. T. Wu, C. S. Hsu, and J. M. Chen, *Mol. Cryst. Liq. Cryst.* **304**, 441 (1997).
- [70] D. Cuypers, H. De Smet, and A. Van Calster, *J. Display Technol.* **7** (3), 127 (2011).
- [71] S. Gauza, M. Jiao, S. T. Wu, P. Kula, R. Dąbrowski, and X. Liang, *Liq. Cryst.* **35** (12), 1401 (2008).
- [72] S. H. Lee, S. M. Lee, H. Y. Kim, J. M. Kim, S. H. Hong, Y. H. Jeong, C. H. Park, Y. J. Choi, J. Y. Lee, and J. W. Koh, *SID Int. Symp. Digest Tech.* **32**, 484 (2001).
- [73] S. H. Lee, S. L. Lee, H. Y. Kim, and T. Y. Eom, *SID Int. Symp. Digest Tech.* **30**, 202 (1999).
- [74] L. M. Blinov and V. G. Chigrinov, *Electrooptic effects in liquid crystal materials*. (Springer-Verlag, 1994).
- [75] H. J. Yun, M. H. Jo, I. W. Jang, S. H. Lee, S. H. Ahn, and H. J. Hur, *Liq. Cryst.* **39** (9), 1141 (2012).

- [76] Y. Chen, F. Peng, T. Yamaguchi, X. Song, and S. T. Wu, *Crystals* **3** (3), 483 (2013).
- [77] C. H. Wen, S. Gauza, and S. T. Wu, *Appl. Phys. Lett.* **87** (19), 191909 (2005).
- [78] M. G. Clark, E. P. Raynes, R. A. Smith, and R. J. A. Tough, *J. Phys. D* **13** (11), 2151 (1980).
- [79] A. Lien, *Appl. Phys. Lett.* **57** (26), 2767 (1990).
- [80] Z. Ge, S. T. Wu, S. S. Kim, J. W. Park, and S. H. Lee, *Appl. Phys. Lett.* **92** (18), 181109 (2008).
- [81] Y. Sun, Z. Zhang, H. Ma, X. Zhu, and S. T. Wu, *Appl. Phys. Lett.* **81** (26), 4907 (2002).
- [82] M. Jiao, Z. Ge, Q. Song, and S. T. Wu, *Appl. Phys. Lett.* **92** (6), 061102 (2008).
- [83] R. Lu, X. Zhu, S. T. Wu, Q. Hong, and T. X. Wu, *J. Display Technol.* **1** (1), 3 (2005).
- [84] X. Zhu, Z. Ge, and S. T. Wu, *J. Display Technol.* **2** (1), 2 (2006).
- [85] D. Armitage, I. Underwood, and S. T. Wu, *Introduction to Microdisplay*. (Wiley, Hoboken, NJ, 2006).
- [86] M. S. Brennesholtz and E. H. Stupp, *Projection Displays*, 2nd ed. (Wiley, 2008).
- [87] S. T. Wu and C. S. Wu, *Appl. Phys. Lett.* **68** (11), 1455 (1996).
- [88] S. Lee, C. C. Mao, and K. M. Johnson, *Opt. Eng.* **45** (12), 127402 (2006).
- [89] K. H. Fan-Chiang, S. T. Wu, and S. H. Chen, *J. Display Technol* **1** (2), 304 (2005).
- [90] H. Wang, T. X. Wu, X. Zhu, and S. T. Wu, *J. Appl. Phys.* **95** (10), 5502 (2004).
- [91] Y. Chen, F. Peng, and S. T. Wu, *J. Display Technol.* **9** (2), 78 (2013).
- [92] C. H. Wen, S. Gauza, and S. T. Wu, *J. SID* **13** (9), 805 (2005).
- [93] S. H. Lee, S. M. Kim, and S. T. Wu, *J. SID* **17** (7), 551 (2009).

- [94] S. S. Kim, *SID Symp. Dig. Tech.* **36**, 1842 (2005).
- [95] K. Miyachi, K. Kobayashi, Y. Yamada, and S. Mizushima, *SID Symp. Dig. Tech.* **41**, 579 (2010).
- [96] H. Hong, H. Shin, and I. Chung, *J. Display Technol.* **3** (4), 361 (2007).
- [97] A. Yoshizawa, *RSC Advances* **3** (48), 25475 (2013).
- [98] F. Reinitzer, *Monatsh. Chem.* **9** (1), 421 (1888).
- [99] P. Etchegoin, *Phys. Rev. E* **62** (1), 1435 (2000).
- [100] W. Y. Cao, A. Munoz, P. Palffy-Muhoray, and B. Taheri, *Nat. Mater.* **1** (2), 111 (2002).
- [101] H. S. Kitzerow, H. Schmid, A. Ranft, G. Heppke, R. A. M. Hikmet, and J. Lub, *Liq. Cryst.* **14** (3), 911 (1993).
- [102] F. Castles, F. V. Day, S. M. Morris, D. H. Ko, D. J. Gardiner, M. M. Qasim, S. Nosheen, P. J. W. Hands, S. S. Choi, R. H. Friend, and H. J. Coles, *Nat. Mater.* **11** (7), 599 (2012).
- [103] D. Xu, Y. Chen, Y. Liu, and S. T. Wu, *Opt. Express* **21** (21), 24721 (2013).
- [104] J. Yan, S. T. Wu, K. L. Cheng, and J. W. Shiu, *Appl. Phys. Lett.* **102**, 081102 (2013).
- [105] C. D. Tu, C. L. Lin, J. Yan, Y. Chen, P. C. Lai, and S. T. Wu, *J. Display Technol.* **9** (1), 3 (2013).
- [106] L. Rao, Z. Ge, S. T. Wu, and S. H. Lee, *Appl. Phys. Lett.* **95** (23), 231101 (2009).
- [107] M. Kim, M. S. Kim, B. G. Kang, M. K. Kim, S. Yoon, S. H. Lee, Z. Ge, L. Rao, S. Gauza, and S. T. Wu, *J. Phys. D: Appl. Phys.* **42** (23), 235502 (2009).
- [108] M. Jiao, Y. Li, and S. T. Wu, *Appl. Phys. Lett.* **96** (1), 011102 (2010).

- [109] H. C. Cheng, J. Yan, T. Ishinabe, and S. T. Wu, *Appl. Phys. Lett.* **98** (26), 261102 (2011).
- [110] L. Rao, J. Yan, S. T. Wu, S. I. Yamamoto, and Y. Haseba, *Appl. Phys. Lett.* **98** (8), 081109 (2011).
- [111] M. Wittek, N. Tanaka, D. Wilkes, M. Bremer, D. Pauluth, J. Canisius, A. Yeh, R. Yan, K. Skjonnemand, and M. Klasen-Memmer, *SID Int. Symp. Digest Tech.* **43**, 25 (2012).
- [112] Y. Chen, D. Xu, S. T. Wu, S. Yamamoto, and Y. Haseba, *Appl. Phys. Lett.* **102**, 141116 (2013).
- [113] P. R. Gerber, *Mol. Cryst. Liq. Cryst.* **116** (3-4), 197 (1985).
- [114] Y. Haseba and T. Kuninobu, US Patent No. 7,879,413 B2 (Feb. 1 2011).
- [115] A. Taugerbeck, P. Kirsch, D. Pauluth, J. Krause, and M. Heckmeier, US Patent No. 7,223,150 B2 (May 29 2007).
- [116] M. Jiao, J. Yan, and S. T. Wu, *Phys. Rev. E* **83** (4), 041706 (2011).
- [117] Y. Chen, J. Yan, M. Schadt, S. H. Liu, K. L. Cheng, J. W. Shiu, and S. T. Wu, *J. Display Technol.* **9** (2013).
- [118] L. M. Blinov, *Electro-optical and magneto-optical properties of liquid crystals*. (Wiley, 1983).
- [119] Y. Li, Y. Chen, J. Sun, S. T. Wu, S. H. Liu, P. J. Hsieh, K. L. Cheng, and J. W. Shiu, *Appl. Phys. Lett.* **99** (18), 181126 (2011).
- [120] A. C. Metaxas and R. J. Meredith, *Industrial Microwave Heating*. (IET, London, 1983).
- [121] M. Schadt, *Mol. Cryst. Liq. Cryst.* **66** (1-4), 639 (1981).

- [122] C. H. Wen and S. T. Wu, *Appl. Phys. Lett.* **86** (23), 231104 (2005).
- [123] Y. Liu, Y. F. Lan, H. Zhang, R. Zhu, D. Xu, C. Y. Tsai, J. K. Lu, N. Sugiura, Y. C. Lin, and S. T. Wu, *Appl. Phys. Lett.* **102**, 131102 (2013).
- [124] Y. Liu, Y. F. Lan, Q. Hong, and S. T. Wu, *J. Display Technol.* **10** (1), 3 (2014).
- [125] H. Choi, H. Higuchi, and H. Kikuchi, *Appl. Phys. Lett.* **98** (13), 131905 (2011).
- [126] H. Choi, H. Higuchi, and H. Kikuchi, *Soft Matter* **7** (9), 4252 (2011).
- [127] Y. Chen and S. T. Wu, *Appl. Phys. Lett.* **102** (17), 171110 (2013).
- [128] S. Yokoyama, S. Mashiko, H. Kikuchi, K. Uchida, and T. Nagamura, *Adv. Mater.* **18** (1), 48 (2006).
- [129] H. Kikuchi, *Liquid Crystalline Blue Phases*. (Springer Berlin, Heidelberg, 2008).
- [130] J. Yan and S. T. Wu, *J. Display Technol.* **7** (9), 490 (2011).
- [131] T. Mizunuma, T. N. Oo, Y. Nagano, H. Ma, Y. Haseba, H. Higuchi, Y. Okumura, and H. Kikuchi, *Opt. Mater. Express* **1** (8), 1561 (2011).
- [132] J. Zhu, S. Ni, Y. Song, E. Zhong, Y. Wang, C. Chen, Z. Ye, G. He, D. Wu, and X. Song, *Appl. Phys. Lett.* **102** (7), 071104 (2013).
- [133] C. Y. Fan, H. C. Jau, T. H. Lin, F. C. Yu, T. s. Huang, C. Liu, and N. Sugiura, *J. Display Technol.* **7** (11), 615 (2011).
- [134] T. N. Oo, T. Mizunuma, Y. Nagano, H. Ma, Y. Ogawa, Y. Haseba, H. Higuchi, Y. Okumura, and H. Kikuchi, *Opt. Mater. Express* **1** (8), 1502 (2011).
- [135] H. S. Kitzerow and C. Bahr, *Chirality in Liquid Crystals*. (Springer, New York, 2001).
- [136] P. Pieranski, P. E. Cladis, T. Garel, and R. Barbetmassin, *J. Physique* **47** (1), 139 (1986).

- [137] H. S. Kitzerow, *Mol. Cryst. Liq. Cryst.* **202**, 51 (1991).
- [138] S. Yamamoto, Y. Haseba, H. Higuchi, Y. Okumura, and H. Kikuchi, *Liq. Cryst.* **40** (5), 639 (2013).
- [139] Y. Li, Y. Chen, J. Yan, Y. Liu, J. Cui, Q. Wang, and S. T. Wu, *Opt. Mater. Express* **2** (8), 1135 (2012).
- [140] J. Yan, H. C. Cheng, S. Gauza, Y. Li, M. Jiao, L. Rao, and S. T. Wu, *Appl. Phys. Lett.* **96** (7), 071105 (2010).
- [141] H. Stegemeyer and F. Porsch, *Phys. Rev. A.* **30** (6), 3369 (1984).
- [142] M. Heckmeier and D. Pauluth, US Patent No. 7,033,651 B2 (Apr. 25 2006).
- [143] M. Yanai, Y. Kubo, and E. Nakagawa, US Patent No. 6,572,938 B2 (Jun. 3 2003).
- [144] N. Hattori, H. Yamamoto, and H. Fujita, US Patent No. 7,608,310 B2 (Oct. 27 2009).
- [145] M. Schadt, R. Buchecker, F. Leenhouts, A. Boller, A. Villiger, and M. Petrzilka, *Mol. Cryst. Liq. Cryst.* **139**, 1 (1986).
- [146] M. Schadt, R. Buchecker, and K. Müller, *Liq. Cryst.* **5** (1), 293 (1989).
- [147] Q. Song, S. Gauza, J. Sun, S. T. Wu, and X. Liang, *Liq. Cryst.* **36** (8), 865 (2009).
- [148] J. Sun, H. Xianyu, S. Gauza, and S. T. Wu, *Liq. Cryst.* **36** (12), 1401 (2009).
- [149] J. Yan, Y. Chen, S. T. Wu, and X. Song, *J. Display Technol.* **9**, 24 (2013).
- [150] E. M. Averyanov and V. F. Shabanov, *Sov. Phys. Crystallogr.* **23**, 177 (1978).
- [151] T. K. Bose, B. Campbell, S. Yagihara, and J. Thoen, *Phys. Rev. A.* **36** (12), 5767 (1987).
- [152] F. C. Frank, *Discuss. Faraday Soc.* **25**, 19 (1958).
- [153] H. Xianyu, S. T. Wu, and C. L. Lin, *Liq. Cryst.* **36** (6-7), 717 (2009).

- [154] F. Peng, Y. Chen, J. Yuan, H. Chen, S. T. Wu, and Y. Haseba, *J. Mater. Chem. C* **2** (18), 3597 (2014).
- [155] J. Sun, H. Xianyu, Y. Chen, and S. T. Wu, *Appl. Phys. Lett.* **99** (2), 021106 (2011).
- [156] L. Rao, J. Yan, and S. T. Wu, *J. Soc. Inf. Disp.* **18** (11), 954 (2010).
- [157] L. Rao, J. Yan, S. T. Wu, Y. C. Lai, Y. H. Chiu, H. Y. Chen, C. C. Liang, C. M. Wu, P. J. Hsieh, S. H. Liu, and K. L. Cheng, *J. Display Technol.* **7** (12), 627 (2011).
- [158] J. Yan and S. T. Wu, *Opt. Mater. Express* **1** (8), 1527 (2011).
- [159] T. W. Dakin, in *Engineering Dielectrics*, edited by R. Bartnikas, R. M. Eichhorn, and B. Brook (1983), pp. 663.
- [160] K. M. Chen, S. Gauza, H. Xianyu, and S. T. Wu, *J. Display Technol.* **6** (8), 318 (2010).
- [161] J. Yan, Y. Chen, S. T. Wu, S. H. Liu, K. L. Cheng, and J. W. Shiu, *J. Appl. Phys.* **111** (6), 063103 (2012).
- [162] H. C. Cheng, J. Yan, T. Ishinabe, C. H. Lin, K. H. Liu, and S. T. Wu, *J. Display Technol.* **8** (11), 627 (2012).
- [163] C. T. Wang, H. Y. Liu, H. H. Cheng, and T. H. Lin, *Appl. Phys. Lett.* **96** (4), 041106 (2010).
- [164] G. Heppke, M. Krumrey, and F. Oestreicher, *Mol. Cryst. Liq. Cryst.* **99** (1-4), 99 (1983).
- [165] S. Y. Lu and L. C. Chien, *Opt. Lett.* **35** (4), 562 (2010).
- [166] J. Yan, Y. Chen, D. Xu, and S. T. Wu, *J. Appl. Phys.* **114** (11), 113106 (2013).
- [167] K. Uchida, Y. Hisakado, H. Kikuchi, and T. Kajiyama, *Trans. Mater. Res. Soc. Jpn.* **29** (3), 819 (2004).

- [168] J. H. Flack and P. P. Crooker, *Mol. Cryst. Liq. Cryst.* **69** (3-4), 281 (1981).
- [169] R. M. Hornreich and S. Shtrikman, *Phys. Rev. A.* **28** (3), 1791 (1983).
- [170] C. Bohley and T. Scharf, *J. Opt. A: Pure Appl. Opt.* **6** (3), S77 (2004).
- [171] G. W. Gray and A. Mosley, *Mol. Cryst. Liq. Cryst.* **48** (3-4), 233 (1978).
- [172] G. L. Hoatson, A. L. Bailey, A. J. van der Est, G. S. Bates, and E. E. Burnell, *Liq. Cryst.* **3** (6-7), 683 (1988).
- [173] S. T. Wu, Q. H. Wang, M. D. Kempe, and J. A. Kornfield, *J. Appl. Phys.* **92** (12), 7146 (2002).
- [174] M. Schadt, *Annual Rev. Mater. Science* **27** (1), 305 (1997).
- [175] Y. Chen, H. Xianyu, J. Sun, P. Kula, R. Dabrowski, S. Tripathi, R. J. Twieg, and S.-T. Wu, *Opt. Express* **19** (11), 10843 (2011).
- [176] B. D. Mistry, *A Handbook of Spectroscopic Data: Chemistry-UV, IR, PMR, CNMR and Mass Spectroscopy*. (Oxford book company, Jaipur, India, 2009).
- [177] S. T. Wu, *Opt. Eng.* **26** (2), 120 (1987).
- [178] R. C. Sharp, D. P. Resler, D. S. Hobbs, and T. A. Dorschner, *Opt. Lett.* **15** (1), 87 (1990).
- [179] G. W. Gray and S. M. Kelly, *J. Mater. Chem.* **9** (9), 2037 (1999).
- [180] E. Bartmann, *Adv. Mater* **8** (7), 570 (1996).
- [181] P. Kirsch and M. Bremer, *Angew. Chem. Int. Ed.* **39** (23), 4217 (2000).